UNIVERSITY OF THE WITWATERSRAND, JOHANNESBURG
SCHOOL OF MECHANICAL ENGINEERING

AN INVESTIGATION INTO THE USE OF FLOATING-TIP AILERONS ON SKEW-WING AIRCRAFT

BY

R J DAVIS

A Dissertation presented in fulfilment of the requirements for the Degree of Master of Science in Engineering.

DECEMBER 1975

to Cecile

DECLARATION

I, ROBERT JOCELYN DAVIS, hereby declare that this dissertation is my own work and has not been submitted as a dissertation for the Degree of Master of Science in Engineering to any other University.

Robert J Davis

ABSTRACT

Wind-tunnel tests were conducted on a rectangular planform skew wing, fitted with floating-tip ailerons. Rolling criteria calculated from static rolling moment and lift results showed good aileron performance in the low incidence cruise régime. Trends were for favourable yawing moments to be generated; the usual asymmetric pitch/roll cross-coupling was observed. Rolling performance in the unskewed position was reasonably well predicted by lifting-line theory - the resulting lift distribution appeared very non-elliptic towards the wing-tips, resulting in higher induced drag than the optimum elliptic distribution. Tests on a second wind-tunnel model indicated that the effect of the incidence discontinuity at the wing/aileron interface spread further spanwise than was expected. Conclusions were that the improved roll performance of floating-tip ailerons might be outweighed by the increase in induced drag. Further research was required in the transonic régime to determine effects on wave drag. Research into the dynamic performance was also required. It is suggested that lifting-surface theory be used for performance prediction of the skewed case.

ACKNOWLEDGEMENTS

The author would like to thank the following people, without whose continuing support this project could never have been undertaken.

Professor B W Skews - my supervisor, for all his inspiration, encouragement and advice, throughout the duration of this research programme; not only at the University, but also in the general aeronautical field.

Mr and Mrs L Davis - my parents, for their encouragement and support throughout the formative stages of my career.

Mr F A S Bezuidenhout - and his team of technicians who so competently manufactured the two wind-tunnel models.

The South African Council for Scientific and Industrial Research - for their financial assistance in the form of a bursary.

TABLE OF CONTENTS

LIST OF FIGURES

NOTATION

ROMAN

A_k polynomial coefficients

A_n Fourier series coefficients

A_R aspect ratio

a semi-major axis of ellipse m

a_o two-dimensional lift curve slope per rad

b semi-minor axis of ellipse m

C wind-tunnel cross-sectional area m^2

C_L' local lift coefficient $= L'/\frac{1}{2}\rho V^2 c$

C_L lift coefficient $= L/\frac{1}{2}\rho V^2 S$

C_D drag coefficient $= D/\frac{1}{2}\rho V^2 S$

C_Y side-force coefficient $= Y/\frac{1}{2}\rho V^2 S$

C_M pitching-moment coefficient $= M/\frac{1}{2}\rho V^2 Sc$

C_{M_o} zero-lift pitching-moment coefficient

C_ℓ rolling moment coefficient $= \ell/\frac{1}{2}\rho V^2 Ss$

C_n yawing moment coefficient $= n/\frac{1}{2}\rho V^2 Ss$

c focus of ellipse, local chord size m

D drag force N

g acceleration due to gravity ms^{-2}

h manometric height m

height of model above tunnel centre-line m

height of rectangular wind-tunnel m

k ratio of s' to a

L lift force N

ℓ	rolling moment Nm
M	pitching moment Nm
n	yawing moment Nm
p	static pressure P_a
R	gas constant
RC	roll criterion = C_ℓ/C_L
r	radius of milling cutter mm
S	wing area m^2
s	semi-span of wing m
s'	semi-span of trailing vortices m
T	absolute temperature ^oK
V	free-stream velocity ms^{-1}
w	width of rectangular wind-tunnel m
x	Cartesian co-ordinate
Y	side-force N
y	Cartesian co-ordinate
z	Cartesian co-ordinate

GREEK

α	local incidence from zero lift degrees
Γ	circulation $m^2\ s^{-1}$
δ	wind-tunnel interference factor
	induced drag factor
η	elliptical co-ordinate
θ	spanwise variable
κ	wind-tunnel interference factor
Λ	skew angle degrees

μ	parameter in lifting-line theory
ξ	elliptical co-ordinate
	aileron differential, deg, positive if in a direction to cause positive C_ℓ
ρ	air density kg m^{-3}
ρ_ω	density of water kg m^{-3}
ψ	stream function

COMPUTER OUTPUT NOTATION

CD	drag coefficient
CL	lift coefficient
CPM	pitching moment coefficient
CRM	rolling moment coefficient
CSF	side-force coefficient
CYM	yawing moment coefficient

CHAPTER 1

INTRODUCTION

Ecological considerations have recently shifted the emphasis in research and development from very high speed overland supersonic flight, to the transonic and low supersonic regime. By suitable monitoring of meteorological conditions, an aircraft may fly at speeds up to fifty per cent faster than present subsonic transports, without creating a sonic boom on the ground.

In order to decide on a transonic configuration, the NASA recently contracted the Boeing Commercial Airplane Company to undertake a comparative study of five different configurations (Ku 73). The configurations examined were an arrow-wing, a variable geometry arrow-wing, a delta wing, a twin-fuselage skew wing, and a single-fuselage skew wing. Figure 1.1 overleaf shows a comparison of the drag coefficients for the cruise condition, and figure 1.2 compares the take off gross masses for the configurations, all designed for the same payload, range, cruise speed and altitude.

Clearly, the single-fuselage skew wing had the lowest gross mass, and since it had the lowest drag, had the lowest fuel consumption of the five configurations examined. The study also showed the single-fuselage skew wing to be the most quiet configuration, bettering FAR part 36 by 15 EPNdB.

First conceived in the early post-war years, when the advantages of sweepback became evident, the skew wing aircraft does not have the bilateral symmetry found in conventional aircraft and birds. However, the comparative study for the NASA showed the aerodynamic advantages to outweigh the

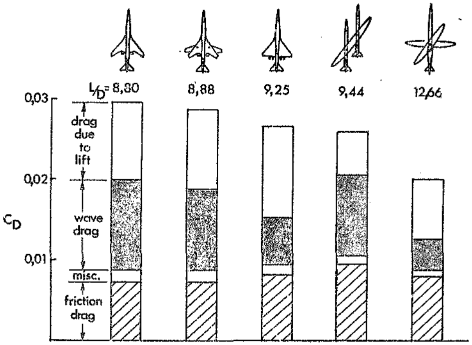

FIGURE 1.1: Cruise Drag Comparison

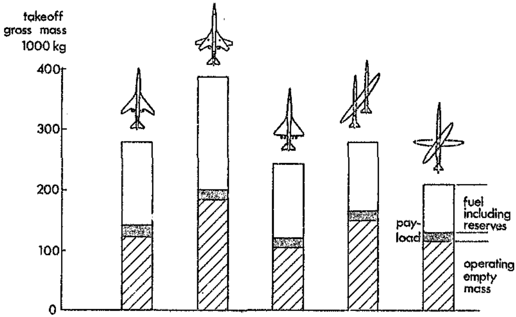

FIGURE 1.2: Takeoff Gross Mass Comparison

intuitive objections to this lack of symmetry.

In early research on the skew wing configuration, some control difficulties were encountered, particularly in the ineffectiveness of the ailerons at high skew angles. The purpose of this investigation, was to examine the effectiveness of floating-tip ailerons on a skew wing configuration, and thus to determine whether an overall improvement in performance was possible.

It must be noted that for the purposes of this dissertation, the term "skew wing" refers to "slewed wing","oblique wing", "yawed wing", and "skewed wing". The term "floating-tip aileron" refers to "floating wing-tip aileron".

CHAPTER 2

REVIEW OF PREVIOUS WORK

Since, to the author's knowledge, floating-tip ailerons have not been used on either a skewed, or sweptback configuration before, this Chapter is divided into two sections. One deals with previous work on the skew-wing configuration, the other with floating-tip ailerons.

Well established theoretical and experimental techniques used in this work will not be reviewed here, but will be referenced in appropriate sections of the text.

2.1 THE SKEW-WING CONFIGURATION

The work carried out for this dissertation was not chiefly concerned with drag minimisation using a skew-wing configuration. The theory of drag minimisation using a skew-wing is therefore not quoted in this section; a resumé of the developments is given. The reader is referred to the references for a fuller theoretical background.

Although various sources claim to have proposed a skew-wing configuration, (Sc 75), the first published work on this concept appears to be that of Campbell and Drake in 1946 (CD 46). They tested a model in the Langley free-flight wind-tunnel, and found that for skew angles of up to 40^{o}, no serious control difficulties were encountered. Some pitch/roll coupling was observed in their static force tests, but this was not encountered in free flight. Evidently, the change of longitudinal lift distribution produced by deflecting the ailerons was almost immediately cancelled by the rolling motion of the model. The wing in effect simply followed the helix angle defined by an effective twist associated with aileron deflection, with no significant change in lift distribution. At a skew angle of 60°, however, aileron effectiveness was unsatisfactorily weak.

The first authoritive theoretical work on drag minimisation appears to be that of Jones (Jo 51, Jo 52). Basically, he showed that an elliptic planform, with elliptic spanwise variation of thickness/chord ratio, satisfied the conditions for minimum drag. Furthermore, he showed that yawing the wing at an angle to the flow further reduced this minimum drag.

Smith (Sm 61) further extended the theory for a skew-wing of given volume, and showed that at a Mach number of two, lift/drag ratios were:

> 'very much the same for skewed elliptic wings and for slender delta-like wings'.

In a paper in 1972, Jones (Jo 72b) summarised these results:

> 'for any area bounded by two streamlines and two characteristic lines, the distribution of lift and volume yeilding the minimum pressure drag (i.e. wave drag and vortex drag) places all the elements of lift and volume near a diagonal lifting line. Such a diagonal line may be thought of as the limiting configuration of a narrow elliptic wing [as illustrated in Fig. 2.1]. Minimum drag occurs when the surface loading of the ellipse is constant and when the projected cross-sectional area is that of a Sears-Haack body'.

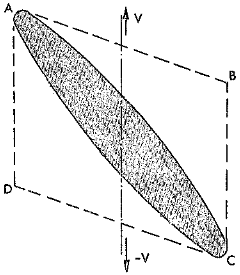

FIGURE 2.1: Optimum Distribution of Lift and Volume within Area ABCD

Graham, Jones and Boltz (GJ 73) performed wind-tunnel experiments on a skew-wing-body configuration, and found that reasonably high lift/drag ratios were possible in the transonic and low supersonic regions. Figure 2.2 shows the values obtained. The envelope over these curves shows the lift/drag ratios which may be obtained by continually varying skew angle as Mach number increases.

At high skew angle and large angles of attack, they found that premature tip-stall occurred on the downstream wing-tip. This behaviour may be compared with the premature tip-stall encountered with sweptback wings; causing the aircraft to pitch nose-up and stall completely. Tip-stall of the skew-wing causes lift to be lost on the downstream wing, and will result in a rolling motion.

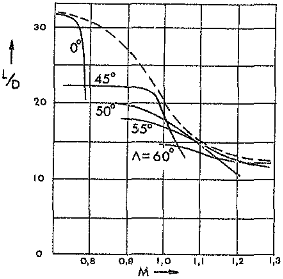

FIGURE 2.2: Lift/drag ratios for a skew-wing-body combination at various skew angles

Interest in a transonic transport aircraft increased in the early 1970's, in the search for a faster, but boomless aircraft. For the case of an aircraft at an altitude of the order of 10 000 metres, it is possible to fly in the transonic region (at about Mach 1,2, depending on local wind conditions) without a shock wave being transmitted to ground level. This is due to the increasing temperature causing a decrease in Mach number with decreasing altitude, so that the shock wave degenerates to a sound wave before reaching ground level (Jo 72a).

Kulfan *et al* (Ku 73, Ku 74) conducted a comparative study of five transonic configurations, the results of which are summarised in ref SD 75. They found that overall, the single-fuselage skew-wing was the most promising configuration.

However, two problem areas were suspected at first. With the wing in the skewed position, downwash from the forward wing-tip decreased the forward wing's effective angle of attack. This resulted in a spanwise shift of centre of lift towards the aft-swept wing; and a rolling moment resulted. Secondly, with the use of a moderately high aspect ratio, it was feared that aeroelastic effects might cause some difficulties.

However, it was found that upward bending of the wing-tips created a dihedral, which in fact tended to move the spanwise centre of lift back towards the centre-line of the aircraft. Furthermore, wing flexibility was introduced to a six-degree freedom stability analysis, and it was found that rigid-wing divergent responses to an elevator pulse became convergent.

With careful aeroelastic design, therefore, it may be possible to overcome some of the inherent aerodynamic difficulties of the skew-wing configuration.

2.2 FLOATING-TIP AILERONS

In the early 1930's, the NACA performed a set of systematic tests, comparing various lateral control devices, particularly at high angles of attack. Floating-tip ailerons were first tested in 1932 (WH 32) by Weick and Harris, on rectangular planform wings. Generally, it was found that they resulted in reasonable roll control, especially in post-stall conditions, where conventional ailerons failed almost completely. No appreciable adverse yawing moments were found, but large favourable yawing moments were generated. However, floating-tip ailerons were found to have an adverse effect on aircraft performance; presumably due to an increase in trailing vortex drag.

Weick and Harris (WH 33) extended their tests to tapered wings, and found that floating-tip ailerons on tapered wings gave better roll performance than on rectangular wings. It is suggested that this was due to higher local loading on the smaller chord on the tapered wing. They again noticed adverse effects on performance - a decrease in lift/drag ratio. Their tests included multiple floating-tip ailerons, but it was concluded that their performance was not as good as single, full-chord floating-tip ailerons.

Bamber (Ba 34) investigated the performance of floating-tip ailerons as an aircraft control during spinning, in 1934. He found that very large rolling and yawing moments were generated in a direction opposing the spin, if no aileron differential was applied. Yawing and rolling moments were also computed, assuming that each aileron was an isolated aerofoil, and that no aileron-wing interference was present. There was considerable discrepancy between experimental and theoretical values; computed values being far larger than measured values. Bamber attributed this discrepancy to wing-aileron interference.

Soulé and Gracey (SG 37) performed a series of flight tests, using a Fairchild 22 monoplane aircraft, fitted with conventional, and then floating-tip, ailerons on a tapered wing, in 1937. They considered the floating-tip ailerons to be unsatisfactory, since their rolling action was approximately half that for conventional ailerons. They commented that since the stick forces on floating-tip ailerons were relatively small, their area could have been considerably increased, giving an increased effectiveness, before the stick forces approached those of conventional ailerons. However, this increase in area would necessitate an increase in wing-span, and therefore weight.

Overall results from previous work thus show that floating-tip ailerons are very effective in post-stall and spin conditions. Their effectiveness in the more normal flight regime is, however, not as good as that of conventional ailerons.

They also have a detrimental effect on general aircraft performance (a decrease in lift/drag ratio).

CHAPTER 3

USE OF LIFTING-LINE THEORY FOR FLOATING-TIP AILERONS

Bamber (Ba 34) attempted prediction of floating-tip aileron performance by assuming each aileron to be an isolated aerofoil, and no wing/aileron interference to be present. He found considerable discrepancy between predicted and experimental aileron performance.

It was decided to investigate the use of the "Monoplane Equation", based on a lifting-line model, to predict the performance of floating-tip ailerons. It was hoped that this method, taking into account local changes in wing incidence and aerofoil section, would prove more accurate than that used by Bamber.

Due to the symmetry of the lifting-line model, the investigation was limited to prediction of aileron performance for the unskewed case.

3.1 THE LIFTING-LINE IDEALISATION AND THE MONOPLANE EQUATION

The simplest three-dimensional wing theory is that based on the concept of the lifting-line (proposed by Prandtl in 1921), where the wing is replaced by a straight line at the chordwise position of aerodynamic centre. The lift developed is due to a spanwise "bound vortex" about this straight line.

The bound vortex sheds a continuous trailing vortex sheet; the local strength of which depends on the local strength of lift on the wing (see figure 3.1 overleaf).

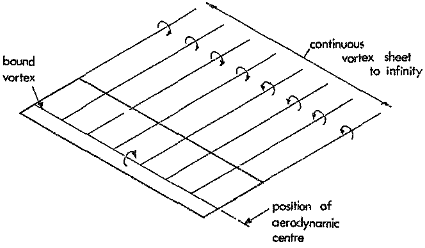

FIGURE 3.1: The Lifting-Line Idealisation

The trailing vortices are assumed not to roll up behind the wing, but remain parallel and continue to infinity downstream.

The derivation of the Monoplane Equation based on this lifting-line model may be found in most aerodynamics texts (HB 70), and will not be repeated here.

The Monoplane Equation as used in this dissertation is as follows:

$$\Sigma A_n \sin n\theta \, (n\mu + \sin\theta) = \mu \, \alpha \sin \theta \quad \ldots\ldots (3.1)$$

$$\text{where } \mu = \frac{a_o c}{8s} \quad \ldots\ldots\ldots\ldots (3.2)$$

and the lift distribution is given in terms of the circulation by the Fourier Series:

$$\Gamma = 4s\ V \sum_{1}^{\infty} A_n \sin n\theta \quad . . . . (3.3)$$

where the spanwise variable θ is defined by

$$y = -s \cos \theta \quad . . . . (3.4)$$

The method of solution is to evaluate (3.1) for as many values of θ between 0 and π (but not *at* $\theta = 0$ or π, as this leads to $0 = 0$ for zero loading at the tips) as coefficients A_n are required.

Having determined the A_n coefficients, the lift, trailing vortex drag, and rolling and yawing moments are given by (HB 70):

lift: $C_L = \pi . A_1 . A_R \quad . . . . (3.5)$

trailing vortex drag:

$$C_{D_V} = \frac{(1 + \delta)}{\pi\ A_R}\, C_L{}^2 \quad . . . . (3.6)$$

where $\delta = \frac{1}{A_1{}^2} \sum_{n=2}^{\infty} (2n - 1)\ A^2_{2n-1}$

rolling moment:

$$C_\ell = \frac{\pi}{2} . A_2 . A_R \quad . . . . (3.7)$$

yawing moment:

$$C_n = \frac{\pi}{2}\, A_R \sum_{n=1}^{\infty} (2n + 1)\ A_n \quad A_{n+1} \quad . . . . (3.8)$$

3.2 SOLUTION OF THE MONOPLANE EQUATION FOR FLOATING-TIP AILERONS WITH NO INCIDENCE DIFFERENTIAL

The usual method of solution of the Monoplane Equation is to set-up equation (3.1) for as many *equally-spaced* definition points along the wing as coefficients are required.

The following matrix equation ensues:

$$\begin{bmatrix} A_1 \\ A_2 \\ \vdots \\ \vdots \\ \vdots \\ \vdots \\ \vdots \\ \vdots \\ A_n \end{bmatrix} \cdot \begin{bmatrix} \sin\theta_1(\mu_1+\sin\theta_1)+\sin 2\theta_1(2\mu_1+\sin\theta_1)+\ldots+\sin n\theta_1(n\mu_1+\sin\theta_1) \\ \sin\theta_2(\mu_2+\sin\theta_2)+\sin 2\theta_2(2\mu_2+\sin\theta_2)+\ldots+\sin n\theta_2(n\mu_2+\sin\theta_2) \\ \vdots \\ \vdots \\ \vdots \\ \vdots \\ \vdots \\ \vdots \\ \sin\theta_n(\mu_n+\sin\theta_n)+\sin 2\theta_n(2\mu_n+\sin\theta_n)+\ldots+\sin n\theta_n(n\mu_n+\sin\theta_n) \end{bmatrix}$$

$$= \begin{bmatrix} \mu_1\ \alpha_1\ \sin\ \theta_1 \\ \mu_2\ \alpha_2\ \sin\ \theta_2 \\ \vdots \\ \vdots \\ \vdots \\ \vdots \\ \vdots \\ \vdots \\ \mu_n\ \alpha_n\ \sin\ \theta_n \end{bmatrix} \qquad \ldots\ldots\ldots\ldots\ (3.9)$$

where subscript n denotes value at the nth definition point.

the matrix equation is then solved for the coefficients A_n by the normal matrix methods.

For the case of floating-tip ailerons, all of the geometric and aerodynamic parameters are known, except for the aileron geometric incidence. As the name "floating-tip" implies, the ailerons are free to float at some stable angle of incidence, referred to as the "floating angle". Since the ailerons are situated in the upwash field generated by the wing, their floating-angle will depend on the wing lift distribution, and hence wing incidence.

A second factor contributing to floating-angle, is the zero-lift pitching-moment coefficient of the aileron aerofoil section. As may be seen from figure 3.2 below, a pitching moment condition has to be satisfied. For equilibrium, there must be no nett pitching-moment about the pitching axis.

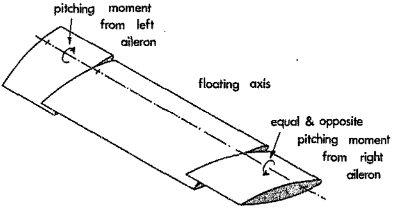

FIGURE 3.2: Aileron Pitching-Moment Equilibrium

The pitching-moment equilibrium may be separated into three cases:

(i) ailerons having a cambered aerofoil section without incidence differential. Since there is no incidence differential, these ailerons will float at an incidence giving zero pitching-moment. This will occur at aileron incidences giving *negative* nett aileron lift, since the stable C_M - C_L curve has negative slope, and, for a cambered aerofoil intersects the C_L axis at a negative value. (Further discussion on aileron stability may be found in Chapter 6).

(ii) ailerons having a symmetrical aerofoil section without incidence differential. Since there is no incidence differential, these ailerons will also float at an incidence giving zero pitching-moment. However, this will occur at an aileron incidence giving *zero* nett lift across the aileron; since the C_M - C_L curve for a symmetric section passes through the origin.

(iii) ailerons of both types (i) and (ii) above, but with incidence differential. This case is dealt with in section 3.3 of this chapter.

As mentioned before, the usual method of solution of the Monoplane Equation is to set-up equation (3.1) for n equally-spaced definition points. Since the step change at the wing/aileron interface is a severe change of parameters in so short a spanwise distance, it was decided not to use equally-spaced definition points all along the wing and aileron, but rather equally-spaced definition points all along the wing, and equally-spaced points on the aileron. Figure 3.3 overleaf shows the definition point system used.

A computer programme was written using this definition point system to set-up and solve the Monoplane Equation. From figure 3.3 it may be seer that there are three variables affecting the definition point system:

(i) ratio of n_a to n_w

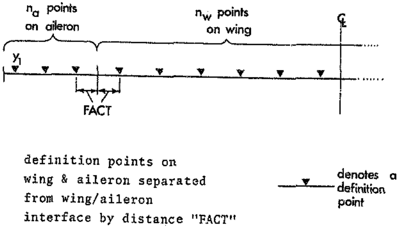

FIGURE 3.3: The Definition Point System

(ii) distance from first definition point y_1 to the aileron tip.

(iii) distance "FACT".

(i) The ratio of n_a to n_w was varied for an aileron differential of 30^o; figure 3.4 overleaf shows how the resulting rolling moment coefficient was affected. The lift distribution was plotted out for each case, and a value of n_a to n_w ratio was obtained which gave a reasonably smooth lift distribution while reasonable rolling moments were obtained. At first it appeared that keeping a constant ratio of n_a to n_w resulted in a constant rolling moment, but some change (0,6%) occurred for large values of n_w; this presumably being due to round-off error accumulating from solving large matrix equations (111 by 111).

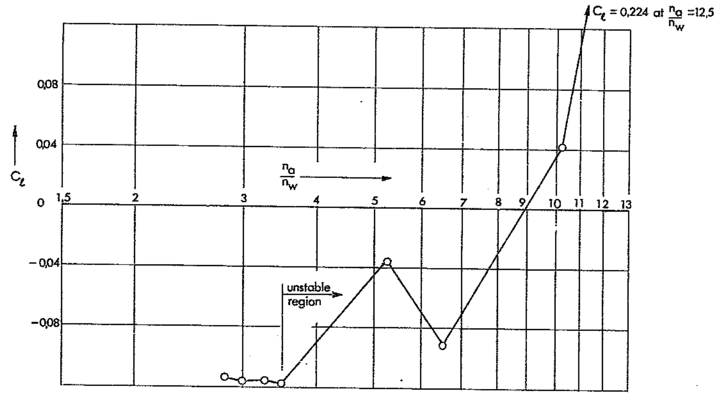

FIGURE 3.4: Effect of Changing Ratio of n_a to n_w on Rolling Moment : For Aileron Differential of 30^o in a Sense to Give Negative Rolling Moment

(ii) The distance from the first definition point to the aileron tip was varied, for a wing at positive incidence, fitted with ailerons at negative incidence. From examination of the resulting lift distributions, a distance was chosen which gave the smoothest reasonable distribution, especially at the aileron tip. Figure 3.5 shows that as the distance from the first definition point to the aileron tip increases, so the "spike" at the aileron tip becomes less severe. This "spike" is discussed further in Chapter 6.

(iii) The distance "FACT" from the wing/aileron interface to the first wing definition point was varied, and the resulting induced drag factor δ and lift distributions were examined. It was found that there was a reasonably large variation in δ for varying FACT: figure 3.6 overleaf shows this. FACT was varied until the resulting δ matched experimentally obtained values (these are discussed in Chapter 6). Figure 3.6 also shows the sensitivity of the lift-curve slope to variations in FACT.

Once the distribution of definition points had been optimised in (i), (ii) and (iii) above, the computer programme was modified to determine the aileron floating-angle, the criterion for floating being zero nett lift integrated across the symmetrical aerofoil section ailerons.

The method used was that of false position (Ge 70). The method and computer programme are described in detail in Appendix D.3, and a listing of the programme is given. Experimental and theoretical values of floating angles are compared and discussed in Chapter 6.

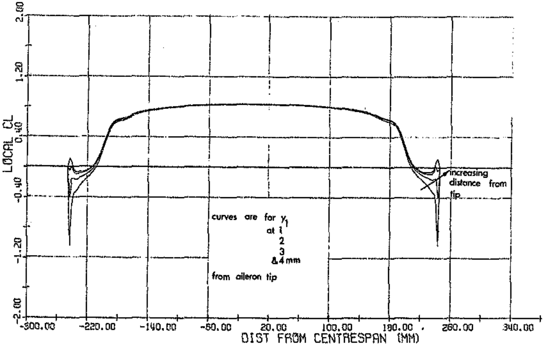

FIGURE 3.5: Effect of Position of y_1 on Lift Distribution

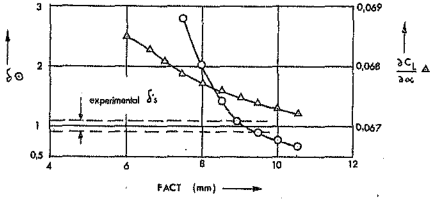

FIGURE 3.6: Effect of FACT on Drag and Lift-Curve Slope for y_1 at 3 mm from Aileron Tip

3.3 SOLUTION OF THE MONOPLANE EQUATION FOR FLOATING-TIP AILERONS WITH INCIDENCE DIFFERENTIAL

The solution of the Monoplane Equation for the case of floating-tip ailerons with incidence differential, differs only from the case of section 3.2 by the definition of aileron floating angle.

Assuming that the pitching-moment/incidence curve for an aileron is antisymmetric about the $C_M = 0$ point, the incidence differential will be divided exactly between the two ailerons. One aileron will have a floating-angle equal to that for the no-differential case *plus* half of the differential; the other *minus* half of the differential. (Note that these incidences are measured from the zero-lift line of the aerofoil section). Each aileron thus produces a pitching-moment which is equal in size and opposite in direction, to that produced by the opposing ailerons.

The computer programme was run for aileron differentials, and results of rolling and yawing moment and lift obtained. These results are compared with experimental results and discussed in Chapter 6.

CHAPTER 4

WIND-TUNNEL BOUNDARY-INDUCED INTERFERENCE

The presence of boundaries in a wind-tunnel produces an alteration in the downwash across a model, which causes optimistic values for lift and drag to be obtained. This upwash velocity effect is dependent on the position of the model in the tunnel, and allowance must be made for it when analysing wind-tunnel test results.

The change in incidence due to upwash is usually expressed in the form (Po 54 ii)

$$\Delta\alpha = \delta.\frac{S}{C}\,C_L \qquad (4.1)$$

where δ = interference parameter
S = model wing area
C = tunnel cross-section area
C_L = lift coefficient

the change in induced drag is then

$$\Delta C_{D_0} = \Delta\alpha.C_L = \delta.\frac{S}{C}(C_L)^2 \qquad (4.2)$$

The force and moment coefficients obtained from wind-tunnel tests are plotted against corrected incidence. Drag coefficients, however, are corrected and then plotted against corrected incidence, since the effect of upwash on induced drag is non-linear (as may be seen from equation 4.2).

4.1 INTERFERENCE FOR THE UNSKEWED (SYMMETRICAL) CASE

In this section, the two-dimensional method of Sanuki and Tani (ST 32), for the determination of upwash velocities for an elliptic cross-section wind-tunnel is reviewed.

The wing system is replaced in the tunnel by an equivalent horseshoe vortex system, the trailing vortices having a span of 2 s'. Figure 4.1 below shows the tunnel/wing system.

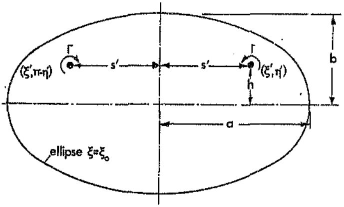

FIGURE 4.1: The Tunnel/Wing System

The fluid motion in the region is considered to consist of two parts; one due to the vortices, the other due to the existence of the tunnel wall. The stream function is written as the sum of two parts

$$\psi = \psi_1 + \psi_2 \qquad \text{. . . . . (4.3)}$$

where ψ_1 is due to the vortices
and ψ_2 is due to the wall.

Introducing elliptical co-ordinates in the form

$$z = x + iy = C \cosh (\xi + i\eta) \quad \ldots\ldots\ldots \quad (4.4)$$

where C is a real constant, Sanuki and Tani show that the resulting interference factor is

$$\delta = \frac{1}{4}\cdot\frac{b}{a}\cdot\frac{\kappa}{k^2} \quad (k = \frac{S'}{a}) \quad \ldots\ldots\ldots \quad (4.5)$$

$$\text{where } \kappa = \sum_{n=1,odd}^{\infty} \frac{e^{-n\xi_o}}{n \cosh (n\xi_o)} \cosh^2 (n\xi') \cos^2 (n\eta')$$

$$+ \sum_{n=2,even}^{\infty} \frac{e^{-n\xi_o}}{n \sinh (n\xi_o)} \sinh^2 (n\xi') \sin^2 (n\eta') \quad \ldots\ldots\ldots \quad (4.6)$$

(ξ', η') are the co-ordinates of the vortex

and the ellipse $\xi = \xi_o$ is the tunnel boundary.

The first problem was to determine the value of ξ_o for the University of the Witwatersrand wind-tunnel. Milne-Thompson (MT 68) shows that for an ellipse of semi-major and semi-minor axes of a and b respectively,

$$\xi_o = \frac{1}{2} \ln (\frac{a + b}{a - b}) \quad \ldots\ldots\ldots \quad (4.7)$$

and that lines of constant ξ form confocal ellipses of focii $(\pm C, o)$, where C is the real constant in equation (4.4), and

$$C^2 = a^2 - b^2 \quad \ldots\ldots\ldots \quad (4.8)$$

Secondly, the determination of ξ' and η' was by consideration of the ellipse passing through (S', h), having semi-major and semi-minor axes of a' and b' respectively, confoc with the ellipse $\xi = \xi_o$.

Hence $C^2 = a^2 - b^2 = (a')^2 - (b')^2$ . . . . (4.9)

Now, for the ellipse of semi-major and minor axes a' and b'

$$\frac{(S')^2}{(a')^2} + \frac{h^2}{(a')^2 - C^2} = 1 \qquad (4.10)$$

solving:

$$(a')^2 = \frac{(S')^2 + h^2 + C^2 \pm \sqrt{((S')^2 + h^2 + C^2)^2 - 4\, C^2 (S')^2}}{2}$$

and

$$(b')^2 = (a')^2 - C^2 \qquad (4.11)$$

the value of ξ' follows from equation (4.7)

namely, $\xi' = \frac{1}{2}\, \ell n \left(\frac{a' + b'}{a' - b'}\right)$

and $\eta' = arcos \left(\frac{S'}{C \cosh \xi'}\right)$ . . . . (4.12)

from (4.11) it may be seen that there are four possible roots. Calculation for the values used revealed two imaginary roots, and one giving a' less than C; thus leaving one acceptable value.

The mathematics described here was incorporated into a computer programme, DAVELIP, which is listed and further described in Appendix D.1. Values of interference parameter for various sized wings at varying height in the wind-tunnel are presented in figure 4.2 overleaf.

Reference to published data for elliptic cross-section wind-tunnels of axis ratio 1 : $\sqrt{2}$, show the values obtained for

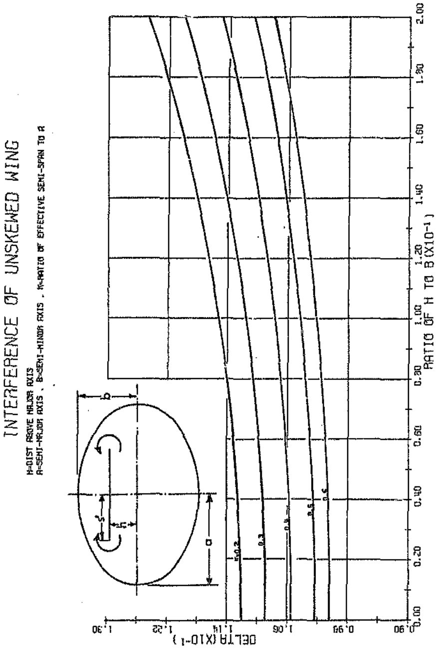
INTERFERENCE OF UNSKEWED WING
H=DIST ABOVE MAJOR AXIS
A=SEMI-MAJOR AXIS , B=SEMI-MINOR AXIS , R=RATIO OF EFFECTIVE SEMI-SPAN TO A
DELTA (X10-1)
RATIO OF H TO B (X10-1)
0.00
0.20
0.40
0.60
0.80
1.00
1.20
1.40
1.60
1.80
2.00
0.90
0.98
1.06
1.14
1.22
1.30
R=0.2
0.3
0.4
0.5
0.6
a
b
h
s'

FIGURE 4.2

the University wind-tunnel, (axis ratio 2:3) to be reasonable.

4.2 INTERFERENCE FOR THE SKEWED CASE

Since no literature was available for wind-tunnel interference for a swept or yawed wing in an elliptic section wind-tunnel, it was decided to interpolate values for a rectangular section wind-tunnel.

A ratio of interference factors for elliptic and rectangular wind-tunnels was calculated for the unskewed wing, and it was assumed that the same ratio held for the skewed case. The interference factors for the rectangular section wind-tunnel were calculated using the method of Katzoff and Hannah (KH 48). This method is reviewed briefly here.

The loading on the wing is approximated by a distribution of point concentrations of lift on the quarter-chord line of the wing, as indicated in figure 4.3 below.

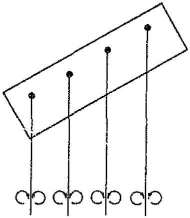

FIGURE 4.3: Replacement of Wing by Point Concentrations of Lift

Associated with each lift concentration is a horseshoe vortex of zero span, extending to infinity downstream of the wing, (Katzoff and Hannah refer to these horseshoe vortices as doublet lines, since the field of a zero-span horseshoe vortex is equivalent to that of a line of source-sink doublets).

Figure 4.4 below shows the image system for one doublet line located in the horizontal plane of symmetry of a rectangular wind-tunnel.

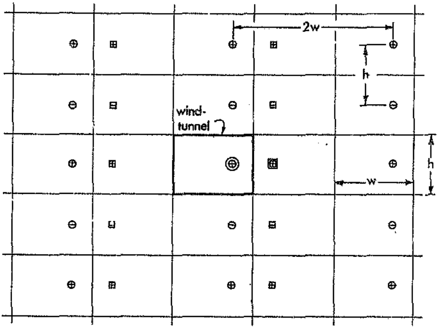

FIGURE 4.4: Images of a Doublet in a Rectangular Wind-Tunnel

The doublet in the tunnel is indicated by a double circle, its nearest lateral image by a double square. The doublets are represented by plus or minus signs according to whether they are the same as or the reverse of the doublet in the tunnel. The system of doublets is composed of two superimposed 2^{ω} by h rectangular arrays of doublets. One array, indicated by circles is considered to be centred at the original doublet (double circle) in the tunnel; the other array is considered to be centred at the nearest horizontal image (double square).

The interference field is thus made up of two parts:

(a) the field of a complete rectangular array having its centre at the double square, and

(b) the field of a complete rectangular array having its centre at the double circle, with the field of the centre doublet omitted (since it represents the lifting element itself and is thus not part of the interference field).

Katzoff and Hannah showed that it was therefore possible to determine the interference field using two "contour" charts of upwash velocity; viz one representing the field due to (b) above, and one representing the flow due to a single doublet (since (a) above is equivalent to (b) above plus the flow due to a single doublet). This procedure must of course be repeated for each point concentration of lift.

The procedure used is as follows:

(i) the lift was assumed to be concentrated at four points, equally spaced along the wing at the quarter-chord. The lift was assumed to be distributed elliptically for the purpose of calculation of point lift concentration strength.

(ii) using the contour charts in Ref *KH 48*, the upwash angle was determined at three equi-distant points on the three-quarter chord line of the wing, as suggested in this reference.

(iii) an arithmetic mean of the upwash angle was taken, and an interference parameter calculated.

Assuming that the change in interference due to skew for the elliptic tunnel is the same as that for the rectangular tunnel, an equivalent interference parameter was calculated for the elliptic tunnel. Figure 4.5 overleaf shows the effect of skew on interference parameter. A secondary assumption may also be seen from figure 4.5; i.e. that the change in interference due to vertical displacement from the tunnel centreline is the same for the skewed as the non-skewed condition. Clearly, the validity of this assumption depends on the skew angle; and it is certainly questionable at large skew angles. However, no other method of determination of interference for an elliptic section wind-tunnel could be found.

Figure 4.5 shows that as the skew angle increases, so does the tunnel-induced interference. At first sight it appears that the reverse should hold, since the wing moves further from the boundary of the wind-tunnel as the skew angle increases. Examination of the contour charts provided in Ref KH 48, shows that the upwash contours are extremely three-dimensional, and depend greatly on stream-wise position.

BOUNDARY-INDUCED INTERFERENCE

H=DIST ABOVE MAJOR AXIS OF WIND-TUNNEL
B=SEMI-MINOR AXIS OF TUNNEL

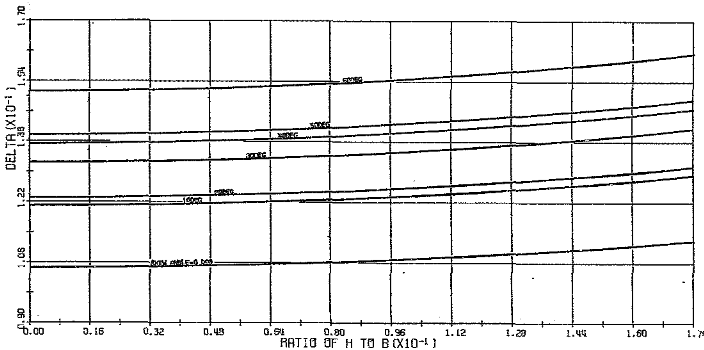

FIGURE 4.5

CHAPTER 5

THE WIND-TUNNEL MODELS

The experimental work carried out for this dissertation consisted of testing a skew-wing/body combination, fitted with floating-tip ailerons (Model No. 1), and a two-dimensional model of the wing/aileron interface (Model No. 2). Model No. 1 was to determine the effectiveness of floating-tip ailerons on a skew-wing configuration, while Model No. 2 resulted from the theoretical investigations in Chapter 3, and was to determine the spanwise lift distribution across the wing/aileron interface.

All experimental work was carried out in the 600 x 900 mm elliptic cross-section, low-speed wind-tunnel facility, of the School of Mechanical Engineering. This is fully described in references Cl 72, Do 66, Si 58, Sm 73 and Appendix A. The reader is referred to Appendix G for detailed manufacturing drawings of both models.

5.1 DESIGN OF WIND-TUNNEL MODEL NO. 1

The requirements for this model may be summarised as follows:

(i) a skew-wing of reasonably high Aspect Ratio

(ii) floating-tip ailerons joined through the wing by an aileron tie-rod.

(iii) accuracy and ease of manufacture

(iv) as high a Reynolds Number as possible.

The size of the model was constrained by the size of the *wind-tunnel working section*; blockage and interference effects to be kept as small as possible.

5.1.1 Main Wing and Ailerons

For ease of manufacture, it was decided to use a wing of rectangular planform. This meant that since the wing was not twisted, and had the same aerofoil section at all spanwise positions, straight cuts could be made in a spanwise direction. The wing could therefore be machined in a milling machine, without necessitating the use of a complex numerically-controlled machine, or tedious point-to-point machining. The drag optimisation provided by an elliptic planform has been well proven (GJ 73), so that the use of an elliptic planform was not justified in terms of added manufacturing complications. Performance of the ailerons would be measured by non-dimensional coefficients, so that comparisons with other planforms would be possible.

The aerofoil section chosen for the wing was a Clark Y; 11,7 per cent thick. This section has several advantages, namely, good performance at Reynolds Numbers down to 150 000, (Po 54i) and a flat bottom for approximately eighty per cent of the chord (from approximately twenty per cent chord to the trailing edge). Also, much of the previous work carried out on floating-tip ailerons used a Clark Y section on the main wing (WH 32, WH 33), enabling comparisons to be made with their work.

It was found in previous work (CD 46) that skewing the wing caused a rolling moment to be developed, lifting the aft-swept wing. In order to counteract this, Campell and Drake (CD 46) placed their skew axis at forty per cent of the chord, at mid-span, so that the forward-swept wing had a greater area than the aft-swept wing. It was for this reason that it was decided to also place the skew axis of the present model at forty per cent of the mid-span chord.

Symmetrical aerofoil section ailerons were to be used first, and Clark Y section ailerons at a later stage. The use of floating-tip ailerons dictates that when an incidence differential is applied to the ailerons, one aileron develops "negative lift" or downward thrust. The use of a symmetric aerofoil section on the ailerons ensured that the downward thrust provided by one aileron was always equal in size and opposite in direction to that provided by the other aileron, at zero skew. *Considering the premature stall of* a cambered aerofoil section at negative incidence, this is not always true of cambered sections; since the aileron providing downward thrust may stall at negative incidence before the other aileron stalls at positive incidence.

Previous work (WH 32, WH 33) showed that aileron flutter could be avoided by placing the rotation axis of the ailerons at seventeen per cent of the chord. This criterion was adopted for Model No. 1.

In order to balance the ailerons statically about their rotation axis, they were of composite construction; an aluminium front and balsa rear section. They were attached to an aileron tie-rod through the wing, by means of grubscrews in the aluminium front section.

Wind-tunnel working-section dimensions necessitated the use of as small a model as possible, although in the interests of accuracy and Reynolds Number, the model had to be as large as possible. A compromise was reached and the following dimensions were chosen for the complete wing:

span	: 492 mm
chord	: 56 mm
aspect ratio	: 8,79
aileron span	: 45 mm (18,27% of wing semi-span).

5.1.2 Wing Support (or Body)

Graham, Jones and Boltz (GJ 73) mounted their wing on an area-ruled Sears-Haack body, which in turn was sting-mounted in their wind-tunnel. This facilitated skewing the wing without necessitating its removal from the tunnel. For convenience, it was decided to use a scaled-down version of this Sears-Haack body in the present investigations. Aspect ratios being approximately the same, the body was scaled-down by the ratio of the wing-spans, thus keeping the area ruling approximately valid.

The wing was mounted on a "saddle" on the body; its flat bottom surface resting on the flat top surface of the saddle. A pin pressed into the wing fitted into a hole in the saddle, perpendicular to its surface. A grubscrew in the body locked the pin in position.

Location of the wing at various skew angles was by means of a small pin in the top surface of the saddle, locating in holes drilled into the undersurface of the wing, at ten degree intervals. This allowed positive, accurate location of the wing at skew angles from zero degrees to sixty degrees, in steps of ten degrees.

Figure 5.1 overleaf shows the method of attachment of the wing to the body.

5.1.3 Sting-Mount and Fairing

It was decided to mount the wind-tunnel model in the wind-tunnel in the same way as Graham, Jones and Boltz (GJ 73), viz, a sting-mount. An extension to the Sears-Haack body was mounted on two struts, shielded from the tunnel flow by a fairing.

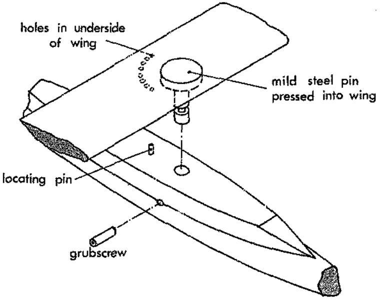

FIGURE 5.1: "Exploded" View of Wing-Body Attachment

For rigidity, the front strut was of reasonably large diameter. The rear strut providing the incidence change, was of lighter construction. Pivoting in the pitching plane was about the attachment point in the front mounting strut.

Due to tunnel blockage effects, it was necessary to keep the fairing size as small as possible. The final cross-section selected consisted of two flat sides, joined at the front by an elliptical curve. At the rear, a smooth curve joined each of the flat sides to the opposite sides of a triangle, closing at the trailing edge. Figure 5.2 overleaf shows the assembled sting-mount and fairing.

The fairing was not used at incidence to the flow, so the bad stall characteristics of an aerofoil section of this shape did not present any problem. A true symmetrical

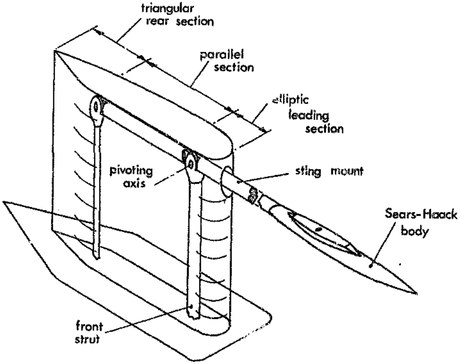

FIGURE 5.2: Assembled Sting-Mount and Fairing

aerofoil section was considered, but disregarded due to the excessive thickness required to enshroud the struts.

The sting-mount protruded from a hole in the front of the fairing, permitting angles of incidence from ten degrees negative to twenty degrees positive. Two stay wires attached to the sides of the fairing prevented any sideways movement which would cause it to touch the sting support.

5.1.4 Generation of Co-ordinates for the Wing Surface

In order to cut the wing profile, it was decided to use a radius cutter in a milling machine. To minimise the "crests" between cuts, it was necessary that as large a radius as possible be used (see Figure 5.3 below).

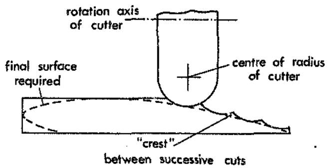

FIGURE 5.3: Use of Radius Cutter in Milling Aerofoil Profile

It was necessary to provide the x-y co-ordinates of the centre of the radius of the cutter to the machinist, thereby generating the x-y co-ordinates of the aerofoil.

Several attempts were made to fit a polynomial through the x-y co-ordinates of the Clark Y aerofoil found in ref Re 61. It was found that the best fit was provided by three polynomials of order ten; one to the curved portion of the bottom surface, one to the front section of the top surface (zero to five per cent chord), and one to the remainder of the top surface. These curves were fitted using a standard computer package programme called "FITT". The slopes of the three curves at their points of intersection were checked for matching, and found to be within one degree. The worst error in fitting the curves to the x-y co-ordinates was less than a tenth of one per cent.

Figure 5.4 below shows the co-ordinate system used.

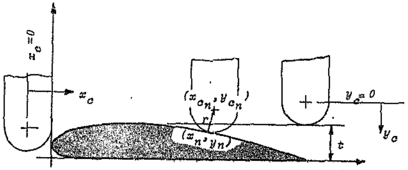

FIGURE 5.4: Co-ordinate System used in Generating x-y Co-ordinates of Cutter Centre

(x_n, y_n)	= co-ordinates of nth point on aerofoil surface
(x_{c_n}, y_{c_n})	= co-ordinates of nth point of cutter corresponding to (x_n, y_n) on the aerofoil surface
$\left.\frac{dy}{dx}\right\|_n$	= slope of aerofoil surface at (x_n, y_n)
t	= maximum thickness of aerofoil
r	= radius of cutter
θ	= $\arctan^{-1} \{ \left.\frac{dy}{dx}\right\|_n \}$

$$y_{c_n} = t - y_n$$

$$x_{c_n} = x_n \pm r \cos\theta \therefore r : + \text{ if } \left.\frac{dy}{dx}\right|_n^{-1} \text{ is positive}$$

$$- \text{ if } \left.\frac{dy}{dx}\right|_n^{-1} \text{ is negative}$$

y_n defined by 10th order polynomial

$$y_n = \sum_{k=1}^{11} A_k\, x_n^{k-1} \quad : \text{where } A_k \text{ are coefficients of polynomial}$$

$$\text{hence } \left.\frac{dy}{dx}\right|_n = \sum_{k=1}^{11} (k-1)\, A_k\, x_n^{k-2} = \sum_{k=2}^{11} (k-1)\, A_k\, x_n^{k-2}$$

The mathematics described here was incorporated into a computer programme to generate (x_{c_n}, y_{c_n}) given (x_n, y_n).

5.2 CONSTRUCTION OF WIND-TUNNEL MODEL NO.1

5.2.1 Construction of the Wing

One of the problems faced in constructing the wing was the method of obtaining a spanwise hole down the wing, to take the aileron tie rod. This was solved by constructing the wing in two sections; an upper and lower section, each having a semi-circular section groove down its length. The aileron tie rod was placed in its "teflon" bearings in this groove, and the two sections epoxied and rivetted together. Figure 5.5 overleaf shows an exploded view of the wing assembly.

The material chosen for the wing was an aluminium alloy B51S, chosen for its strength/weight ratio, and ease of machining with a good surface finish.

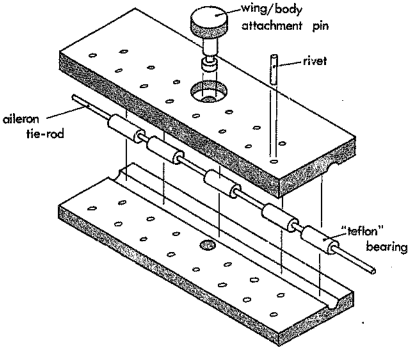

FIGURE 5.5: "Exploded" View of Wing before Final Surface Machining

The wing/bo·ly attachment pin was turned from silver steel and pressed o a reamed hole in the wing.

The wing assembly was then clamped to the bed of the milling machine and machined to final maximum thickness using a fly-cutter. The aerofoil surface was then cut using a radius cutter (o.d. = 32,55 mm; cutting radius = 11,113 mm = r in Figure 5.2). The reference zero in the y-direction was set when the cutter just touched the surface of the unprofiled wing; in the x-direction when the cutter just touched the front surface (see Figure 5.2). Movements in the x and y-directions were measured by two dial gauges, each having a least count of 0,01 mm.

The curved front portion of the bottom surface was machined first, the wing was then turned over and clamped with its flat bottom section on the machine bed: hence the advantage of a Clark Y section. In order to prevent deformation of the thin trailing edge when cutting towards it on the top surface, it was decided to begin cutting *at* the trailing edge, and cut towards the leading edge. After machining the surface had "crests" between cuts, and "troughs" which were at the required final size. It was then a relatively simple matter to rub the "crests" down to the "troughs" with emery paper. The wing was then cut to final span size, and polished to a mirror finish.

The offcuts from the wing were placed in a profile projector (Hilger and Watts TT 777), and compared with a suitably scaled-up drawing. Figure 5.6 overleaf shows a comparison between a true Clark Y and the actual wing. The discrepancy between true Clark Y and the actual wing was within 0,7 per cent.

5.2.2 Construction of Ailerons

The first stage in aileron construction was to machine the aluminium front sections, complete with hole for the tie-rod, and threaded hole for the grubscrew. The balsa rear sections were then glued on with an epoxy cement.

A template of the NACA 0012 section was cut roughly to size, then finished accurately by checking against a scaled-up drawing in the profile projector. The ailerons were then filed down by hand until they approximately fitted the template. They were then sealed with several coats of model aircraft dope to prevent shrinkage and warping, and sanded down to fit the template as accurately as possible.

FIGURE 5.6: Comparison between True Clark Y Section and Actual Wing Section

A covering surface of "Solarfilm" was applied, to ensure a good, uniform surface finish.

The accuracy of the ailerons was not as good as that of the main wing; being approximately two per cent.

5.2.3 Sears-Haack Body and Sting-Mount

Graham, Jones and Boltz (GJ 73) give values of body diameter, at distances from their wing attachment point. As stated before in section 5.1.2, these dimensions were scaled down for the present body.

The body was turned from aluminium bar, using dial gauges for radius and distance measurements. Since the sting-mount would be useful for other work in the wind-tunnel, the Sears-Haack body was not permanently fixed to it; but merely by means of a tapered pin in a reamed hole.

The sting-mount was turned from mild steel stock, as were the front and rear support struts.

5.2.4 Fairing

For ease of setting-up, the fairing was constructed from transparent "Perspex" sheet. This enabled clearance between the sting-mount, struts and fairing to be easily checked by visual observation.

A wooden former was shaped by hand, and the "Perspex" sheet heated in an oil-bath. The soft sheet was then wrapped around the former, clamped in position and left to cool. The former was then removed, and the trailing edge glued together. A bottom support flange (also "Perspex") and stay-wire clamps were then glued to the fairing. Figure 5.7 below shows the method of forming the "Perspex" fairing.

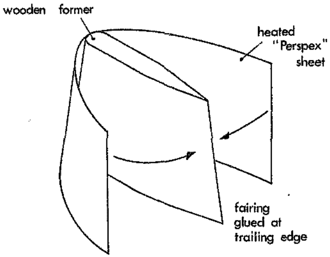

FIGURE 5.7: Forming of Fairing

A "Perspex" top section was made to fit the fairing, and was attached by eight brass screws. This top section had to be removable for assembly and disassembly of the sting-mount support and struts.

5.3 TESTING OF WIND-TUNNEL MODEL NO. 1

Before any testing was carried out, the wind-tunnel, and wind-tunnel balance were first calibrated. Details of the calibrations may be found in Appendix B.

5.3.1 Initial Set-Up and Corrections

In order to align the ailerons, so that they were at the same incidence, the completed wing was placed bottom surface down on two parallel bars on a steel flat surface table. Two smaller parallel bars were inserted under the ailerons, and they were rotated about their floating axis until their trailing edges rested on these bars. The ailerons were then locked in position on the aileron tie rod by means of the small grubscrews in the aileron aluminium front sections (see Figure 5.8 below).

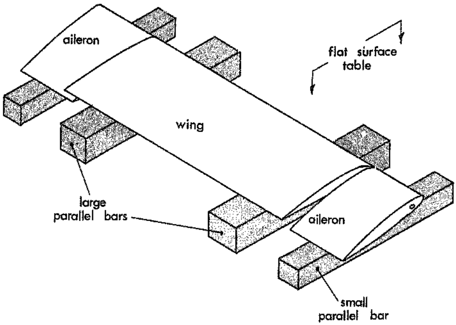

FIGURE 5.8: Aileron Alignment

The Sears-Haack body was then placed in the wind-tunnel, supported by the two struts enshrouded by the fairing. The side force, and yawing and rolling moment components of the balance were then zeroed, and the tunnel run up to operating speed. The Sears-Haack body was then rotated in the yaw direction until no side force was present. The yawing and rolling moments were checked for zero and found to be within the sensitivity of the microvoltmeter output of the balance. These zeros were checked for a range of incidences from approximately 10° below the horizontal to approximately 20° above.

The wing, complete with aligned ailerons was placed in position on the Sears-Haack body, at zero skew. All components of the balance were zeroed, as was the manometer. The atmospheric pressure was measured and recorded. The tunnel was run up to operating speed, and values of the six forces and moments recorded for incidences from zero lift to stall in steps of 0 5 degrees. Also recorded were tunnel initial temperature and starting pitot-pressure. Photographs of the ailerons were taken at the beginning of the test (zero lift), at $6{,}5^{\circ}$ incidence and just before the stall.

The test was repeated after the tunnel had been allowed to cool down, and it was found that the results were within 0,5%, except towards the non-linear stall region.

Curves were fitted through the side-force and yawing and rolling moment data, so that these forces and moments, caused by imperfections in manufacture, would be subtracted when processing data.

5.3.2 Testing in the Skewed Position, and with Aileron Differential

The model was tested for increasing skew angle up to 60° in steps of 10° using the procedure described in section 5.3.1. However, readings were taken at incidence increments of one degree; and photographs at zero lift, mid-range, and upper limit.

The wing was then removed from the Sears-Haack body, and again placed on two parallel bars on a steel flat surface table. The two smaller parallel bars were again placed under the aileron trailing edges, however, a steel block, machined to the correct dimensions was placed on the bar under one of the ailerons, thus creating an incidence differential. The ailerons were then locked in position by the grubscrews as before.

With the ailerons set at an incidence differential, testing was continued for varying skew angle.

The range of tests run is as follows:-

Incidences from zero lift incidence to stall, 19° above zero lift, or serious flutter; which ever occurred first; for aileron differentials of $\pm 5^{\circ}$, $\pm 10^{\circ}$, $\pm 15^{\circ}$; and skew angles of 0° to 60° in 10° increments.

Figure 5.9 overleaf shows wind-tunnel Model No. 1 mounted in position on the balance in the wind-tunnel. The wing has been skewed left wing forward for clarity; the model was tested with the lift wing skewed back.

The experimental results are presented in Appendix F.1.

5.4 DESIGN OF WIND-TUNNEL MODEL NO. 2

Arising from the theoretical work described in Chapter 3, various queries arose regarding the continuity of the press-

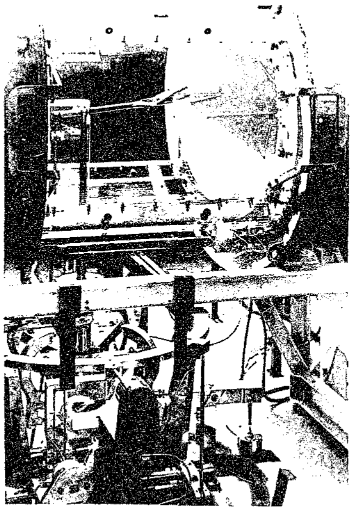

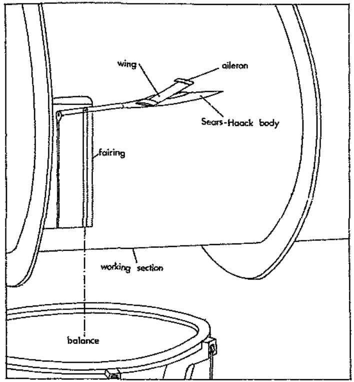

FIGURE 5.9 Model No 1 in the Wind-Tunnel

ure distribution across a step change in wing incidence. In the case of the interface between the wing-tip and the floating-tip aileron, there is not only a step change in incidence, but also a gap through which flow may occur (see Figure 5.10 below).

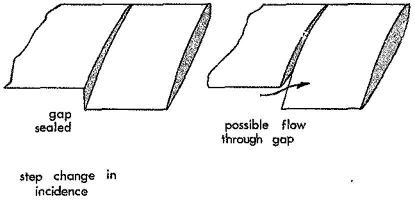

FIGURE 5.10: The Wing/Aileron Interface

It was decided to investigate the pressure distribution across such an interface, in order to determine qualitatively the validity of the theoretical prediction.

The requirements for this model may be summarised as follows:

(i) a variable step change in incidence with no gap sealing.

(ii) the model should span the complete working section of wind-tunnel; keeping the flow two-dimensional at the "tips", the only cross-flow being in the region of the interface gap.

(iii) pressure tappings provided for spanwise pressure distribution measurement.

The aerofoil section chosen was again Clark Y, also for ease of manufacture, and good behaviour at low Reynolds Numbers. The incidence pivot was at seventeen per cent of chord, as in Model No. 1.

Thirty-four spanwise pressure tappings were made in the upper surface of the wing at 30 per cent chord; this position providing the maximum sensitivity of local lift coefficient to pressure for the Clark Y profile.

Since the working section of the wind-tunnel is elliptic, the model was supported by two vertical flat plates, bolted to the top and bottom flanges. Slots were provided in these end-plates to allow changes of incidence. The wing-tip/end-plate interfaces were sealed by two sealing plates. The arrangement is shown in Figure 5.11 below.

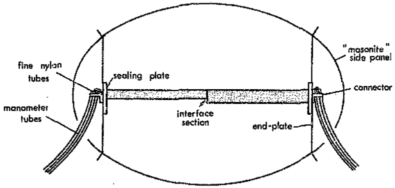

FIGUF 5.11: Arrangement of Model No. 2 in Wind-Tunnel

The original "Perspex" working-section side panels were replaced with "masonite" side panels; holes were cut in these for rubber manometer tubes to pass through. The fine nylon pressure tapping tubes were connected to the rubber manometer tubes via complete hypodermic needles set in an aluminium bracket.

5.5 CONSTRUCTION OF WIND-TUNNEL MODEL NO. 2

The method of construction used was very similar to that of Model No. 1. Again it was constructed in two halves, with a spanwise hole at the pivoting axis to take the pressure tubes and a stiffening rod. The pressure tappings were constructed by cementing short sections of 0,25 mm I.D. hypodermic needle into pre-drilled holes in the upper wing half. 0,5 mm I.D. nylon tubing was then cemented to the hypodermic needles and cemented along the spanwise pivoting axis groove.

When all the pressure tappings had been connec... nylon tubes, the upper and lower halves of each wing were cemented and rivetted together. The aerofoil section was machined in the same manner as Model No. 1. There was no danger of burrs blocking the pressure tappings, since they were at the position of maximum thickness, and were thus not machined. During machining, they were sealed with a strip of masking tape to ensure that no shavings caused any blockages. Figures 5.12 and 5.13 overleaf show the model before assembly and in the milling machine respectively.

5.6 TESTING OF WIND-TUNNEL MODEL NO. 2

The model was placed in position in the wind-tunnel and the laser incidence measuring system calibrated (see Appendix B for details of this system).

Figures 5.14 and 5.15 overleaf show the experimental apparatus, and a view of Model No.2 in the wind-tunnel, respectively.

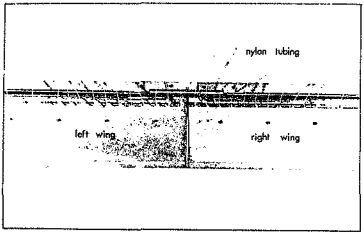

FIGURE 5.12: Model No. 2 before Assembly

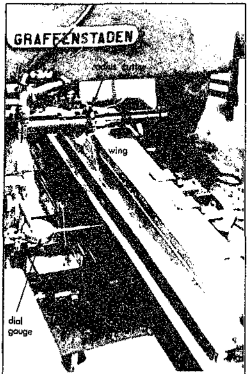

FIGURE 5.13: Model No. 2 in Milling Machine

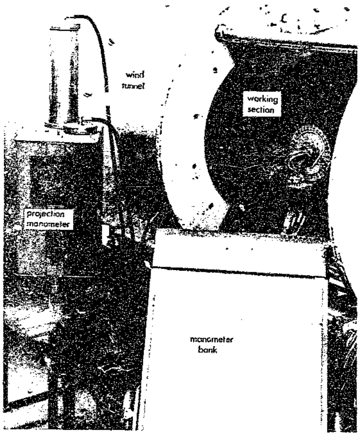

FIGURE 5.14: Experimental Apparatus Used in Testing Model No. 2

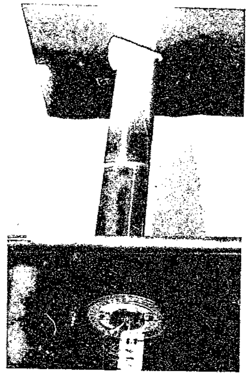

FIGURE 5.15: View of Model No. 2 in the Wind-Tunnel

It was decided to test Model No. 2 at the same Reynolds Number as Model No. 1, thus ensuring similar flow conditions.

The model was set at ten degrees incidence from the zero lift angle on both wings, and the tunnel run up to the required velocity for Reynolds Number matching. The levels of water in the multi-tube manometer were allowed to settle to steady values, and readings of height were recorded. Values of local lift coefficient were calculated, and it was found that there was a slight, approximately linear increase in local lift coefficient from the left wing to the right, spanwise across the model. This was attributed to swirl in the wind-tunnel, and results were modified accordingly (see Chapter 6 and Appendix C).

The test was repeated for incidences of 0^o; $2,5^o$; $5,0^o$ and $7,5^o$ on both wings. Tests were then run with incidence differential. The incidence on one wing was kept constant at ten degrees (this being termed the reference incidence), and pressure distributions were recorded for incidences of the other wing of $7,5^o$; $5,0^o$; $2,5^o$ and 0^o. The roles of the wings were then reversed, and further tests run. This process was repeated for baseline incidences of $7,5^o$; $5,0^o$ and $2,5^o$.

The experimental results are presented in Appendix F.2

CHAPTER 6

DISCUSSION OF RESULTS

The experimental results obtained from the wind-tunnel tests carried out on the two wind-tunnel models, and the theoretical results obtained from the lifting-line wing model, are discussed in this chapter. Experimental results for both wind-tunnel models are presented in Appendix F.

6.1 DISCUSSION OF EXPERIMENTAL RESULTS : WIND-TUNNEL MODEL NO. 1

6.1.1 Lift (Figures F.1, F.7, F.13, F.19, F.25, F.31 and F.37)

The lift coefficient/incidence curves essentially consist of three regions:

(i) the low incidence region, where the graph is rather curved. This was presumably due to friction between the aileron and wing - especially at high skew angles, where stagnation pressure on the aileron tip caused reasonably large frictional forces. When running the wind-tunnel tests, it was found that the ailerons remained essentially still, relative to the wing, as the wing incidence was increased from zero lift, until they suddenly jerked to a new position. This stop/start behaviour continued until about four degrees incidence from zero lift, when, due to larger incidence and floating angles, there was little contact area between the wing-tip and the aileron. Thereafter, the aileron behaviour was quite smooth, with very little stop/start jerking.

(ii) the mid-range incidence region where the graph is essentially straight: this being the region where the aileron behaviour was smooth, and the wing aerodynamic behaviour linear.

(iii) the high-incidence stall region, where the usual non-linear aerodynamic effects are prominent. Some high-frequency aileron oscillations were observed near the stall, especially at high skew angles. These oscillations are further discussed in section 6.4.2 of this chapter.

Since skewing the wing reduced the velocity normal to the leading-edge by a factor of cosine of the skew angle, it was expected that the lift-curve slope would change linearly with skew angle. Figure 6.1 below shows this to be essentially true. At high skew angles, fuselage effects became prominent, and some deviation from the ideal straight line is visible.

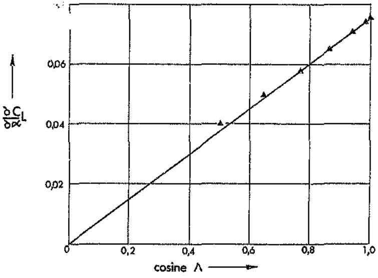

FIGURE 6.1: Effect of Skew on Lift-Curve Slope

There was no apparent effect of aileron differential on the lift/incidence curve, leakage effects presumably being small.

6.1.2 Drag (Figures F.2, F.8, F.19, F.20, F.26, F.32, F.38)

The effect of skew angle on drag coefficient was not found to be marked - being essentially an effect on induced drag at high incidence. The data points obtained from wind-tunnel tests were not joined in the drag coefficient graphs, since there was little to differentiate one curve from another. However, figure 6.2 overleaf, a plot of drag coefficient against lift coefficient squared, shows clearly the changes in induced drag.

Assuming: $C_D = C_{D_O} + \frac{(1 + \delta)}{\pi A_R} C_L^2$ . . . . . . (6.1)

then a plot of C_D versus C_L should be linear, its slope having the value $(1 + \delta)/\pi A_R$. It is clear from figure 6.2 that the slopes of the graphs increase with skew angle, but also that the non-linearity increases with skew angle. Since the aspect ratio of the wing decreased by a factor of $\cos^2\Lambda$, the "spread" of the graphs appears reasonable. No attempt has been made to determine the slopes of the curves, due to their non-linearity at skew angles above 20^O. It is suggested that at large skew angles, the induced drag parameter δ is no longer a constant, but dependent on lift coefficient. This might have been due to cross-flow between the wing and aileron being enhanced by the spanwise component of free-stream velocity. The effect of such a lift-dependent induced drag parameter would be non-linearity of the C_D versus C_L^2 graph.

A second effect of skew angle visible in figure 6.2 is the increase in lift-independent drag C_{D_O}. This was attributed

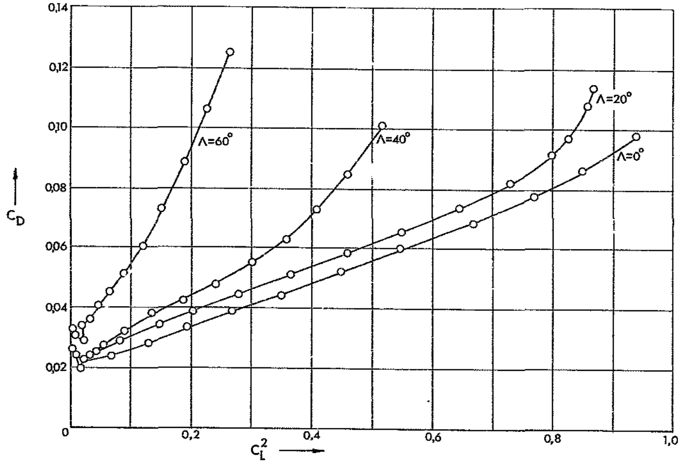

FIGURE 6.2: Effect of Skew on Drag : No Aileron Differential

to pressure drag on the bluff aileron tip increasing as skew angle increased. Some pressure drag could have been acting on the exposed wing-tip as well as the aileron tip (see figure 6.3 below).

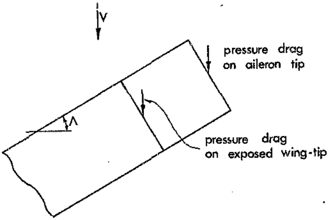

FIGURE 6.3: Increase in Pressure Drag on Wing and Aileron with Skew Angle

Figure 6.4 overleaf is a plot of C_D versus C_L^2 for zero skew angle, and varying aileron differential. There appears to be little change in slope between the no-differential and negative differential graphs, but some discrepancy in slope when a positive differential was applied. This discrepancy appears to be consistent; a similar plot for aileron differential of ten degrees showed the same effect. It is suggested that the effect is due to swirl in the wind-tunnel, increasing the cross-flow effect in one direction, and hindering it in the other.

Figure 6.4 also shows that the lift independent drag, C_{D_0}, increased with increased differential, this being due to increased frontal area of the ailerons at higher differential angles.

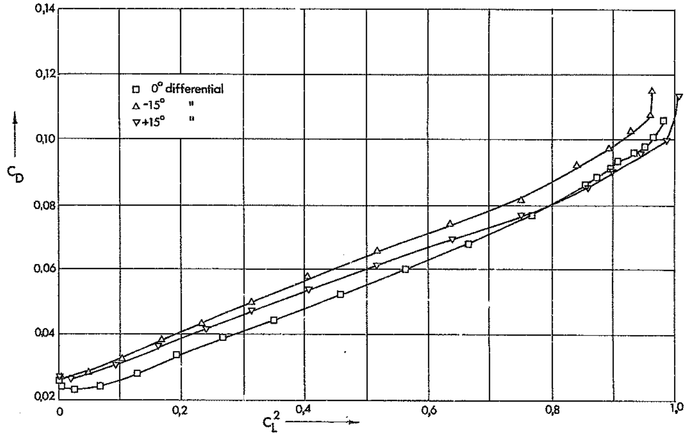

FIGURE 6.4: Effect of Aileron Differential on Drag

6.1.3 Side-Force (Figures F.3, F.9, F.15, F.21, F.27, F.33 and F.39)

If the forces acting in the plane perpendicular to the lift vector, (ie, [illegible] and side-force) are considered to have a resultant a[illegible]al to the leading edge of the wing, (see figure [illegible]ow) then the side-force should increase with skew an[illegible]e, reaching a maximum at 45°.

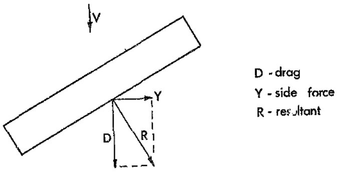

FIGURE 6.5

It may be seen from the side-force/incidence curves that skewing the wing in fact causes a side-force to be developed, which reaches a maximum at skew angles between 40° and 50°. The experimental data of Graham, Jones and Boltz (GJ 73) shows the same effect.

Aileron differential was found to have very little effect on side-force. The side-force coefficients were an order of magnitude smaller than the drag coefficients, which, in turn were a further order of magnitude smaller than the lift coefficients.

6.1.4 Pitching Moment (Figures F.4, F.10, F.16, F.22, F.28, F.39 and F.40)

Of all the experimental results obtained, these were found to have the most scatter. This was attributed to the stop/start behaviour of the ailerons. The general trends observed were reasonably clear however.

The first of these was the change of the slope of the pitching-moment/incidence curves with skew angle. This implies movement of the total model aerodynamic centre from behind the pivot point (about which the moments were taken) to in front of the pivot point, as skew angle increased. However, this is contrary to previously published results (GJ 73). The apparent movement of aerodynamic centre was not very great, however, and may be attributed to the assumptions used in calculating the pitching-moment; especially assuming drag to act at the 40% chord pivot point.

The other trend noticed from the pitching-moment data was the roll/pitch cross coupling. Application of aileron differential caused a pitching-moment to be developed as well as a rolling moment (compare figures F.34 and F.40 with figure F.4). This was merely a function of the asymmetric geometry, as may be seen from figure 6.6 below.

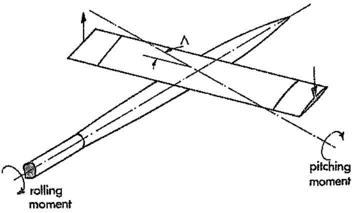

FIGURE 6.6: Pitch/Roll Cross-Coupling

6.1.5 Rolling Moment (Figures F.5, F.11, F.17, F.23, F.29, F.35 and F.41)

It was found that at small skew angles, the rolling moments generated by the floating-tip ailerons were essentially independent of incidence. At higher skew angles two effects were felt : viz

(i) The leading aileron/wing friction prevented the leading aileron from true "floating" at low wing incidences. The trailing aileron, being attached to the leading aileron by the aileron tie rod, was limited to the movement allowed by the torsional flexibility of the tie-rod. Thus, at low wing incidences, there was some incidence-dependence of rolling moment. After the leading aileron had freed itself, the curves were found to be essentially flat.

(ii) At large skew angles, a large proportion of the trailing floating-tip aileron was situated in the wake of the wing, at high incidences. This caused some non-linearity of the rolling moment/incidence graphs.

Figure 6.7 overleaf shows the effects of skew angle on aileron performance. Two distinct effects may be seen - the first being the change in slope of the graphs. As the skew angle increased, so the effectiveness of the ailerons in roll decreased - more and more being contributed to pitching moment. The second effect of skew angle is the rolling moment developed by skewing the wing (ie, the vertical shift of the curves as skew angle increases). This was due to the spanwise shift of centre of pressure from the wing centre-line towards the downstream wing-tip, and was noticed in previous research (CD 46, GJ 73). At skew angles of 50° and 60°, the effect appears to be in the opposite direction. This is in fact due to extrapolation of the

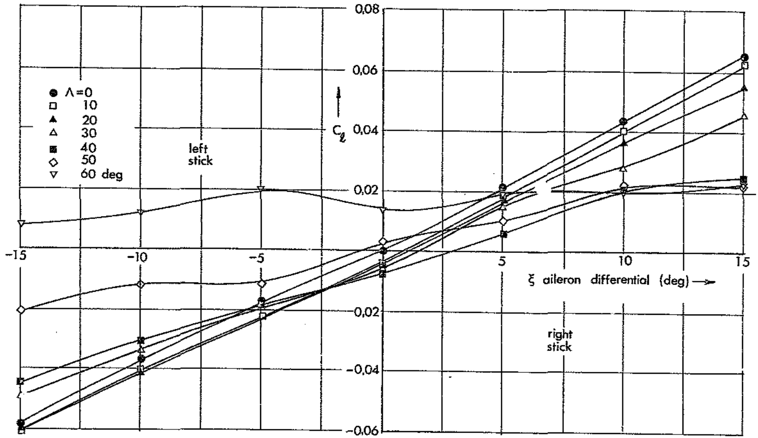

FIGURE 6.7: Effect of Skew on Aileron Performance: $C_L = 0,6$

rolling moment/incidence curves to an incidence corresponding to a lift coefficient of 0,6 (refer to figure F.5 in Appendix F). The non-linearity of the 50^{o} and 60^{o} skew angle curves in figure 6.7 are due to the same extrapolation - however, the trends indicated are useful.

A good measure of aileron effectiveness is the Roll Criterion. It is a measure of the ability of the ailerons to produce a rolling moment by modifying the spanwise wing lift distribution. Weick and Harris (WH 32) found that floating-tip ailerons provided a much better value of Roll Criterion, at all incidences, than conventional ailerons. The performance improvement was particularly marked at high angles of attack near the stall. Figure 6.8 overleaf shows the effect of skew angle on the roll performance of floating-tip ailerons, for an aileron differential of 15^{o} positive. Since, for a rectangular planform monoplane wing:

$$\text{Roll Criterion} = \quad = \frac{C_\ell}{C_L} \qquad \text{(WH 32)}$$

and the rolling moments are essentially independent of incidence, the expected curves were rectangular hyperbolae. Figure 6.8 shows this to be essentially true. The critical Roll Criterion at a value of 0,075, was found by the NACA to represent satisfactory control conditions. Figure 6.8 shows that aileron effectiveness decreases with skew angle, more and more being contributed to pitching moment. In the low incidence cruise regime, aileron effectiveness is seen to be satisfactory.

Figure 6.9 is a similar graph to figure 6.8, for an aileron differential of 15^{o} negative. The dashed line shows the curve for 10^{o} skew, and 15^{o} positive differential, which is above that for 15^{o} negative differential. It would therefore appear that there is some asymmetry in the behaviour of the ailerons. This asymmetry was attributed

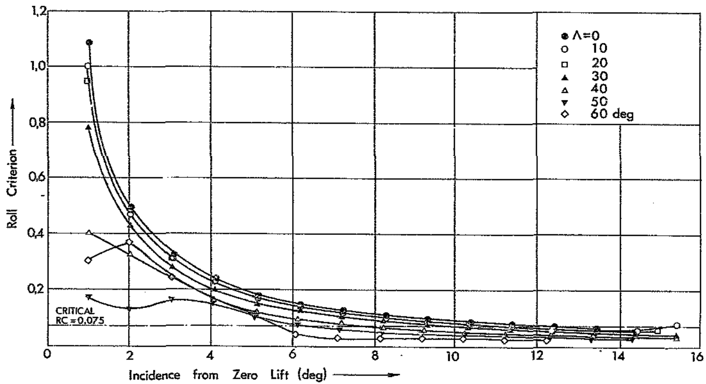

FIGURE 6.8: Effect of Skew on Aileron Effectiveness: 15° Positive Differential

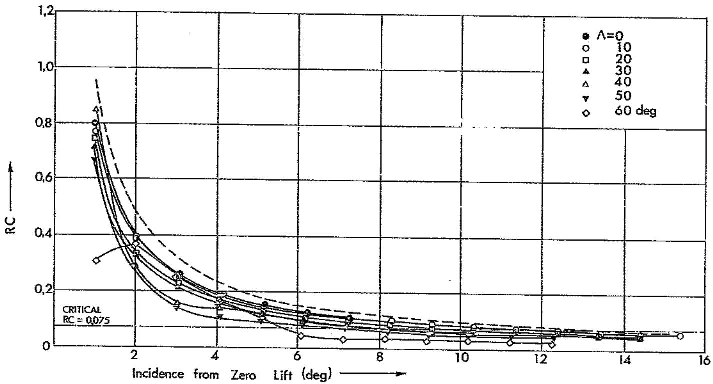

FIGURE 6.9: Effect of Skew on Aileron Effectiveness: 15° Negative Differential

to swirl in the wind-tunnel, increasing the effect of the ailerons in one direction, and opposing their effect in the other. The curve for 60° skew is irregular, this being due to the aileron/wing friction discussed earlier.

Figure 6.10 below compares the performance of floating-tip and conventional ailerons, in the unskewed position, and at a skew angle of 40°. The performance of the floating-tip ailerons is superior in both cases.

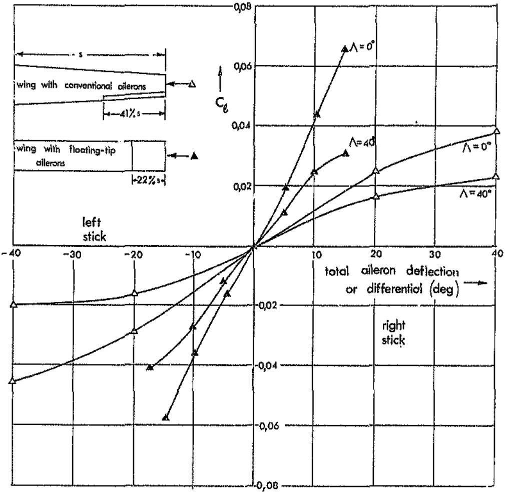

FIGURE 6.10: Comparison of Static Force-Tests of Conventional and Floating-Tip Ailerons: $C_L = 0,6$

6.1.6 Yawing Moment (Figures F.6, F.12, F.18, F.24, F.30, F.36 and F.42)

Skewing the wing was found to create a yawing moment, which increased with increasing skew angle. Figure 6.11 shows this effect at a lift coefficient of 0,6. The effect of aileron differential may also be seen from figure 6.11. Although the data is rather scattered, due to extrapolation as in the rolling moment data, the trend is for favourable yawing moments to be developed, since the slopes of the curves are essentially positive.

6.2 DISCUSSION OF EXPERIMENTAL RESULTS : WIND-TUNNEL MODEL NO. 2

6.2.1 Baseline Lift Distributions

On evaluating the lift distribution across the wings with no incidence differential, it was found that instead of true two-dimensional conditions, there was a linear variation of local lift coefficient, due to swirl in the wind-tunnel. This was corrected for by using the mean value of the readings at pressure-tappings equidistant from the centre-line. Since the readings from some pressure-tappings were disregarded due to leaks or blockages, this "smoothing" process was not used at some positions on the model. Figure 6.12 overleaf shows the lift distributions across the model, for the no-differential tests. The straight lines fitted to the data are arithmetic means of the data points, and represent what will be referred to as the "Baseline Values". The data as corrected appears reasonable, save for those points which could not be "smoothed".

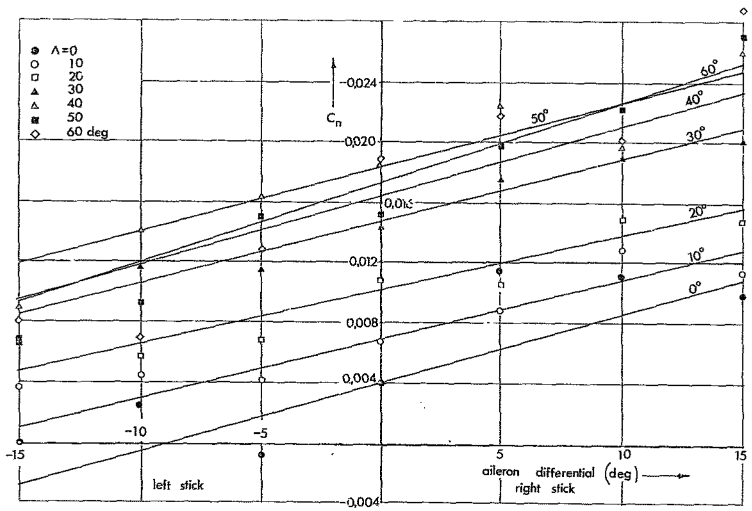

FIGURE 6.11: Effect of Skew on Yawing Moment $C_L = 0.6$

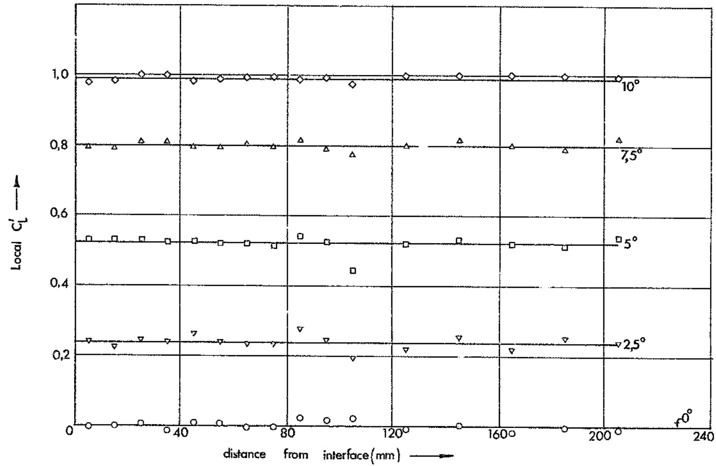

FIGURE 6.12: Baseline Lift Distributions

6.2.2 Lift Curve of the Section

Figure 6.13 overleaf shows a comparison between the lift curve of the section as published in reference Re 61, and the values obtained from the tests described in section 6.2.1. The figure shows good correlation at low incidences - the zero-lift incidences coinciding almost exactly. At mid-range incidences, the experimental values obtained appear rather high. This effect was also noticed, although to a greater extent, when comparing experimental results of Model No. 1 with theoretical predictions (see section 6.3.2). The discrepancy between the values from reference Re 61 and present experimentation is seen to decrease at the high incidence range. This effect was also noticed when comparing experiment and theory. It is suggested that the effect is due to the discrepancy in leading edge radii between the true Clark Y section, and the actual wing section.

6.2.3 Lift Distributions with Incidence Differential

All lift distributions were found to be smooth and continuous, (figures F.43 to F.46), although the effects of the incidence discontinuity were found to propagate further spanwise than was expected.

Before the tests were run, it was presumed that the spanwise propagation of the incidence differential effects would depend only on the magnitude of the incidence differential, and not on the absolute incidence of either wing. Figure 6.14 overleaf shows this presumption to be incorrect, and that there *was* in fact dependence on absolute incidence.

A second trend visible from figure 6.14 is that the spanwise propagation of differential effects is non-linear for the $7\frac{1}{2}^{o}$ reference cases; and almost linear for the 10^{o} reference case.

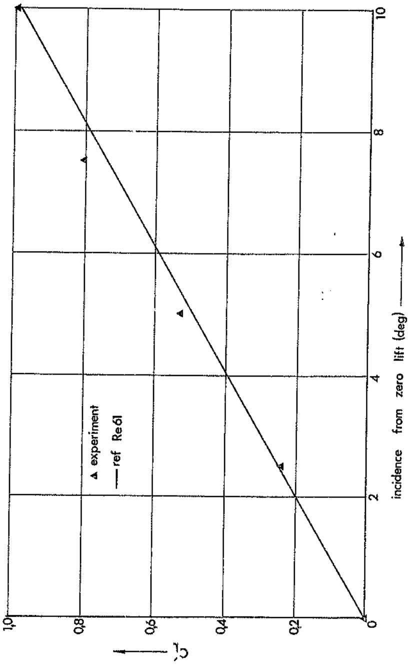

FIGURE 6.13: Comparison of Aerofoil Performance with Reference Re 61

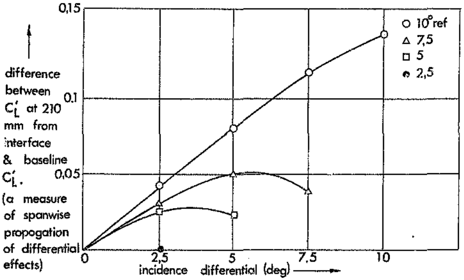

FIGURE 6.14: Effect of Incidence Differential on Spanwise Lift Distribution

The above effects imply rather radical departure from what intuitively should have been linear behaviour. The non-linearity is of the order of five percent, which is above the experimental error of two percent.

6.3 THEORETICAL RESULTS

6.3.1 Lift Distribution

Examination of figure 6.15 overleaf shows that a reasonably smooth lift distribution was predicted; save for the "spikes" at the aileron tips. From equation (3.4), it may be seen that as the aileron tip is approached, θ becomes very small and so $\sin n\theta$ in equation (3.9) also becomes very small. It is suggested that the lift distribution "spikes" are due to manipulation of the matrix equation containing these very small values. The size of these values was increased by moving the first definition point away from the aileron tips, and the "spikes" became less severe. However, the wing definition suffered, and a "wavy" lift distribution resulted. An optimum was reached, and figure 6.15 represents this lift distribution.

6.3.2 The Lift/Incidence Curve

Figure 6.16 on page 6.23 compares the theoretical predictions with experimental results. The dashed line through the experimental results at mid-range incidences, shows correlation of lift-curve slopes to be quite satisfactory: a discrepancy of three per cent was found between experimental and theoretical results. The curvature of the experimental graph might have been due to the smaller leading edge radius used on the aerofoil section, at low Reynolds Numbers, (see figure 5.6).

The reference zero for both curves is the zero-lift condition, which, for the theoretical model, implies zero wing lift alone. Experimentally, zero lift implies zero *nett* lift; the negative fuselage lift was compensated by an equal wing lift. Due to friction, it is possible that

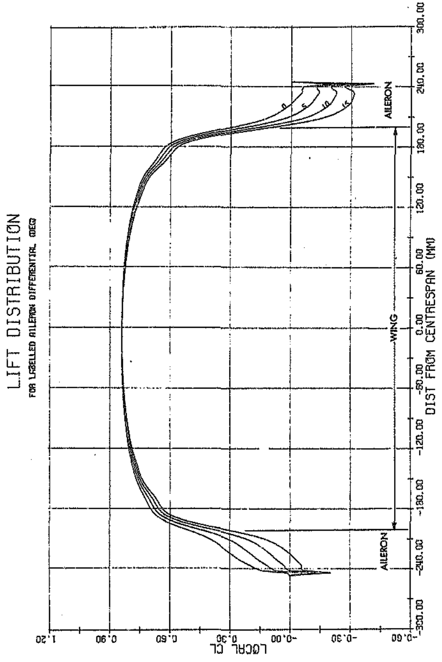
LIFT DISTRIBUTION
FOR LABELLED AILERON DIFFERENTIAL (DEG)
AILERON
WING
AILERON
DIST FROM CENTRESPAN (MM)
LOCAL CL

FIGURE 6.15

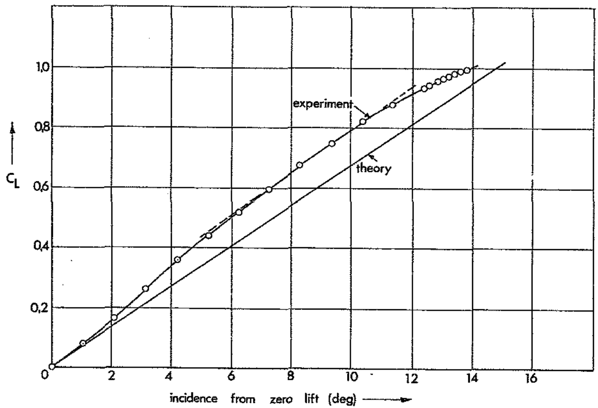

FIGURE 6.16: Comparison of Experimental and Theoretical Lift Performance

the ailerons were not free-floating, and provided some further negative lift. At higher incidences, the fuselage provided some positive lift. These effects perhaps caused the discrepancies in the experimental lift curve.

6.3.3 Induced Drag

The method of optimisation of the definition point system, described in Chapter 3, used correlation between theoretical and experimental induced drag factors. It was found that the induced drag factor was extremely dependent on the definition point system (see figure 3.6).

6.3.4 Rolling Moment

Figure 6.17 overleaf compares theoretical rolling moment predictions with experimental results, for zero skew angle. The results appear very satisfactory at an aileron differential of 5^o; sc ter becoming worse at an aileron differential of 10^o ana 15^o. (The scatter has been discussed in section 6.15 of this chapter.)

6.3.5 Floating Angles

Figure 6.18 (page 26) compares theoretically predicted floating angles with experimental results. At the zero lift angle, it may be seen that the ailerons have a considerable negative floating angle.

This may be due to combination of two causes;

(i) the wing generating lift, which is opposed by the negative fuselage lift, discussed in section 6.3.1.

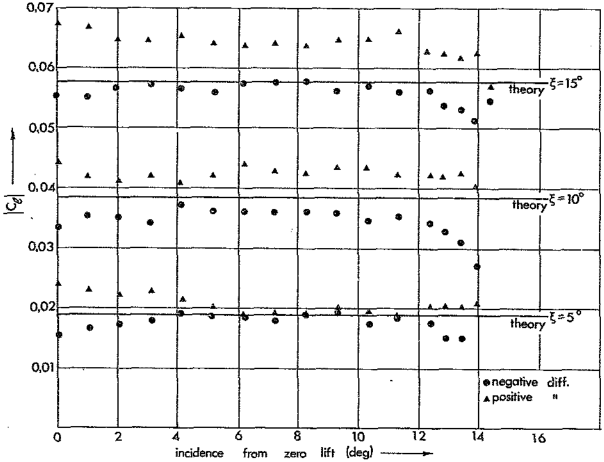

FIGURE 6.17: Comparison of Experiment and Theory for Rolling Moment Prediction

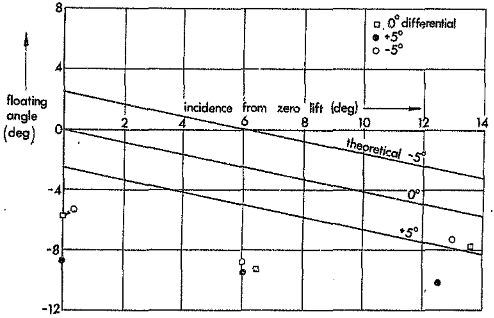

FIGURE 6.18

This wing lift produces an upwash field at the ailerons - hence the negative floating angle. And

(ii) aileron/wing friction.

However, the change in floating angle with wing incidence appears to correlate quite well at low wing incidences. This discrepancy at very high incidences may be due to stall effects.

Since the overall correlation was unsatisfactory, no further results were analysed.

6.4 GENERAL

6.4.1 Criteria for Static Stability of Floating-Tip Ailerons

Assuming that the ailerons are statically balanced about their pivot point (ie, the aileron centre of gravity is on the pivot point), then the following criteria are useful:

(i) The slope of the pitching moment/lift coefficient curve of the *aileron alone* should be negative. This is for gust response of the ailerons; a perturbation from a stable floating-angle results in a stabilising moment being generated. This may be achieved by placing the pivot point of the ailerons ahead of the aerodynamic centre (hence the recommendation of a seventeen per cent chord pivot point by references WH 32 and WH 33).

(ii) The magnitude of the slope of the aileron pitching moment/lift coefficient curve depends on how far ahead of the aerodynamic centre the pivot point is placed. Aeroelastic and dynamic stability considerations might dictate the choice of a slope.

If a cambered aerofoil section is used, then to counteract the zero-lift pitching moment, an out-of-balance moment should be created, so that the curve passes through the origin (see figure 6.19 overleaf).

This means that the floating-tip aileron having a cambered aerofoil section does not pply a downward force on the wing: although some weight penalty might be paid in creating the out-of-balance moment.

Statically balanced floating-tip ailerons having a cambered Clark Y aerofoil section were tested, and it was found that they fluttered excessively. It is presumed that the inter-

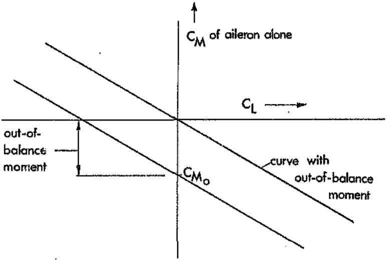

FIGURE 6.19

section between the C_M/C_L curve and the C_L axis was at a large negative lift coefficient; so large that the aileron stalled, and its incidence increased by a weather vane action. The pitching moment was again developed, stall occurred, and the cycle repeated itself.

6.4.2 Aileron Oscillations

Table F.1 in Appendix F lists all the occasions when, at high incidence, high frequency oscillations of the NACA 0012 ailerons occurred. These are not referred to as flutter, since flutter is an aeroelastic effect, and it appears that these aileron oscillations were not due to aeroelastic effects. It is suggested that they were due to the effect of the wake of the wing on the downstream aileron, since the oscillations were only observed at large skew angles and at large incidences just below the stall.

6.4.3 Flow at the Wing/Aileron Interface

A flow visualisation technique was used to examine the flow at the interface of Model No. 2. Neutrally buoyant, helium-filled soap bubbles, of 2 mm diameter, were introduced into the wind-tunnel flow, upstream of the model, and the bubble paths photographed. Figure 6.20 below shows the resulting flow pattern. As may be seen, there is no marked vorticity, although some rotation of the flow may be seen. This was expected from the smooth pressure distribution on Model No. 2.

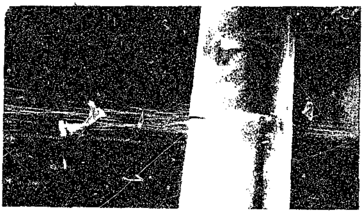

FIGURE 6.20: Visualisation of the Flow about the Wing/Aileron Interface Model

CHAPTER 7

CONCLUSIONS AND SUGGESTIONS FOR FURTHER RESEARCH

It is useful here to repeat the objective in undertaking this research programme:

"investigate the use of floating-tip ailerons on skew wing aircraft, to determine whether an overall improvement in performance is possible".

Bearing this objective in mind, the following conclusions were drawn from the discussion on experimental and theoretical results.

7.1 ROLL PERFORMANCE

Static tests shows the roll performance of floating-tip ailerons to be very good in the low incidence cruise regime, at skew angles up to 60^{o}. In the unskewed position, previous research (Ba 34) showed good performance in the post-stall regime. Skewing the wing up to 20^{o} caused little difficulty in terms of high incidence performance. Above skew angles of 20^{o}, at high incidence, aileron oscillations were caused by wing wake effects on the downstream aileron.

The roll performance of floating-tip ailerons was quite well predicted by simple lifting-line theory.

7.2 CROSS-COUPLING EFFECTS

There were no adverse yawing moments generated by aileron application, trends were for favourable moments to be generated.

The asymmetric geometry of the skew wing aircraft caused pitching moments to be generated by aileron application. These pitching moments would have to be corrected for by a suitable coupled aileron/elevator system in a complete aircraft.

7.3 DRAG EFFECTS

The skewed elliptic wing has been shown to be an optimum in terms of trailing vortex and wave drag, due to the elliptic distributions of lift and thickness (Jo 51, Jo 52). The use of floating-tip ailerons resulted in a very non-elliptic lift distribution, thus increasing the trailing vortex drag from the optimum $\delta = 0$ for an elliptic lift distribution.

A secondary drag effect was the increase in pressure drag with skew angle, due to stagnation pressure effects on the exposed forward-swept wing tip.

It is felt that the improvement in roll performance must be carefully weighed against the detramental effect on lift/drag ratio and hence overall aircraft "efficiency", before it is decided whether floating-tip ailerons result in an improvement in overall aircraft performance.

7.4 SUGGESTIONS FOR FURTHER RESEARCH

The author believes that there are three principal areas in which further research would be of value:

(i) the transonic case - evaluation of the effect of the aileron/wing interface on wave drag in the skewed position.

(ii) the dynamic behaviour of floating-tip ailerons - evaluation of the effectiveness of floating-tip ailerons on a free-flight aircraft model.

(iii) theoretical predictions - use of lifting-surface theory (vortex lattic method) for prediction of skew wing, and floating-tip aileron, performance.

REFERENCES

Ba 74 BAMBER M J. *Aerodynamic Rolling and Yawing Moments produced by Floating Wing-Tip Ailerons, as measured by the Spinning Balance.* NACA Technical Note TN 493, 1934.

CD 46 CAMPBELL J P and DRAKE H M. *Investigation of Stability and Control Characteristics of an Airplane Model with Skewed Wing in the Langley Free-Flight Tunnel.* NACA Technical Note TN 1208, 1946.

Cl 72 CLEGG A *et al. A Report on the Turbulence Level in the Working Section of the Subsonic Wind-Tunnel in the Velocity Range 5-14 m/s, using Hot-Wire Anemometers.* School of Mechanical Engineering, University of the Witwatersrand, Advanced Laboratory, 1972.

Do 66 DOLD, R N S *et al. The Calibration of a Closed-Circuit Subsonic Wind-Tunnel.* School of Mechanical Engineering, University of the Witwatersrand, Advanced Laboratory, 1966.

Ga 75 GARFORTH A M. *Theoretical and Experimental Development of the Constant Volume Method for Determining Laminar Burning Velocity.* PhD Thesis, University of the Witwatersrand, February 1975.

Ge 70 GERALD, C F. *Applied Numerical Analysis.* Addison-Wesley, 1970.

GJ 73 GRAHAM L A, JONES R T and BOLTZ F R. *An Experimental Investigation of Three Oblique-Wing and Body Combinations at Mach Numbers between 0,60 and 1,40.* NASA Technical Memorandum, NASA TM-62,256

HB 70 HOUGHTON E L and BROCK A E. *Aerodynamics for Engineering Students.* Edward Arnold (London), 1970.

Jo 51 JONES R T. *The Minimum Drag of Thin Wings in Frictionless Flow.* J Aero Sci, 18, 12, 1951, p 75.

Jo 52 JONLS R T. *Theoretical Determination of the Minimum Drag of Airfoils at Supersonic Speed.* J Aero Sci, 19, 12, 1952, p 813.

Jo 72a JONES R T. *New Design Goals and a New Shape for the SST.* Astronautics and Aeronautics, 10, 12, 1972, p 66.

Jo 72b JONES R T. *Reduction of Wave Drag by Antisymmetric Arrangement of Wings and Bodies.* AIAA Journal, 10, 2, Feb 1972, pp 171-176.

KH 48 KATZOFF S and HANNAH M E. *Calculation of Tunnel-Induced Upwash Velocities for Swept and Yawed Wings.* NACA Technical Note, TN 1748, 1948.

Ku 73 KULFAN R M *et al. High Transonic Speed Transport Aircraft Study.* NASA Contractor Report, CR-114658, Sept 1973.

Ku 74 KULFAN R M. *Summary Report - High-Transonic Speed Transport Aircraft Study.* NASA Contractor Report, CR-2465, Sept 1974.

MT 68 MILNE-THOMPSON L M. *Theoretical Aerodynamics.* Macmillan and Co, London, 1968.

Po 54i POPE A. *Wind-Tunnel Testing.* Wiley, 1954, p 366.

Po 54ii POPE A. *Wind-Tunnel Testing.* Wiley, 1954, p 273.

Re 61 REIGELS F R. *Aerofoil Sections*. Butterworths, 1961.

Sc 75 SCHRAIVOGEL K I. *Swivel Wing History*. Aviation Week and Space Technology, 10 March, 1975, p 54, Letters to the Editor.

SD 75 SKEWS B W and DAVIS R J. *The Skew Wing*. Wings over Africa, June 1975, pp 24-27.

SG 37 SOUTE H A and GRACEY W. *A Flight Comparison of Conventional Ailerons on a Rectangular Wing and of Conventional and Floating Wing-Tip Ailerons on a Tapered Wing*. NACA Report, TR 630, 1937.

Si 58 SIMON H A. *The Design and Method of Construction of a Closed-Circuit, Low-Speed, Wind-Tunnel*. MSc (Eng) Thesis, University of the Witwatersrand, November 1958.

Sm 61 SMITH J H B. *Lift/Drag Ratios of Optimised Slewed Elliptic Wings at Supersonic Speeds*. Aero Quart, Vol 12, August 1961, pp 201-218.

Sn 73 SNADDON. *A Report on the Attempted Investigation of Turbulence Levels in the Subsonic Wind Tunnel, using Hot-Wire Anemometry*. School of Mechanical Engineering, University of the Witwatersrand, Advanced Laboratory, 1973.

ST 32 SANUKI M and TANI I. *The Wall Interference of a Wind-Tunnel of Elliptic Cross-Section*. Proc. Physical Mathematical Soc. Japan, Vol 14, 1932, p 592.

WH 32 WEICK F E and HARRIS T A. *Wind-Tunnel Research comparing Lateral Control Devices, especially at High Angles of Attack : IV Floating Tip Ailerons on Rectangular Wings.* NACA Report, TR 424, 1932.

WH 33 WEICK F E and HARRIS T A. *Wind-Tunnel Research comparing Lateral Control Devices, particularly at High Angles of Attack : XI Various Floating Wing-Tip Ailerons on both Rectangular and Tapered Wings.* NACA Technical Note, TN 458, 1933.

LIST OF APPENDICES

APPENDIX A

DETAILED DESCRIPTION OF APPARATUS

A.1 THE WIND-TUNNEL

The wind-tunnel is described in detail in references Cl 72, Do 66, Si 58 and Sm 73. A general description is given in this section.

The wind-tunnel is of the closed-circuit type, having a pseudo-elliptic cross-section. Working section dimensions are

minor axis or height	:	609,6 mm
major axis or width	:	914,4 mm
length	:	600,0 mm

The airflow is driven by a fan powered by a 30 kW D.C. motor. Motor control is by a Plastelec thyristor control system. Figure A.1 overleaf shows a schematic view of the wind-tunnel.

The velocity of the airflow in the working section may be varied from approximately 10 m/s to 75 m/s; although at the higher velocities, tunnel heating effects become prominent, and correction has to be made for these.

A.2 VELOCITY MEASUREMENT

The velocity in the wind-tunnel working section was measured using a standard pitot-tube/manometer arrangement. The pitot-tube head protruded approximately 150 mm into the tunnel, keeping well clear of the boundary layer. Dold et al (Do 66) found that the velocity profile in the working sec-

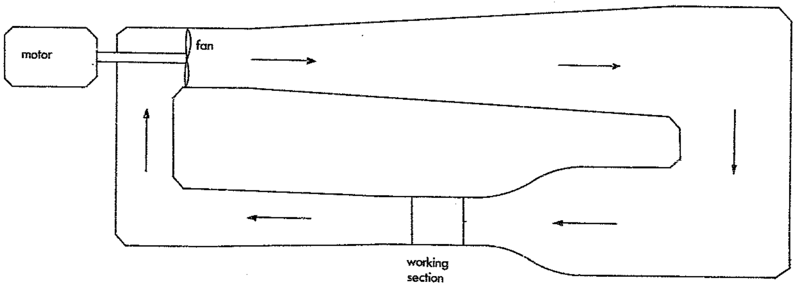

FIGURE A.1: Schematic Plan View of 600 x 900 mm Subsonic Wind-Tunnel tion was essentially flat at the speeds used for testing Model No. 1; the boundary layer being approximately 100 mm thick. The pitot-tube was placed approximately 500 mm upstream of the model, so that its wake would not affect the airflow over the model to any great extent.

The position of the pitot-tube ensured measurement of "free-stream velocity", essentially unaffected by the presence of the model.

Pitot-tube : Airflow Developments
1,30 mm dia stagnation pressure
orifice.

Manometer : Betz-type projection manometer
v. Essen Delft 6750
least count 0,01 inches of water.

A.3 TEMPERATURE MEASUREMENT

The temperature of the airflow was measured using a standard l[illegible]tory mercury thermometer, protruding from the tunnel wall into the flow. This thermometer actually measured stagnation temperature, but since the velocities were relatively low, no correction was made to obtain true static temperature.

Thermometer : standard mercury-in-glass
least count 1,0°C.

A.4 STATIC PRESSURE MEASUREMENT

The wind-tunnel working section is provided with a slot, ensuring that static pressure in the tunnel is the same as ambient atmospheric pressure. The atmospheric pressure tion was essentially flat at the speeds used for testing Model No. 1; the boundary layer being approximately 100 mm thick. The pitot-tube was placed approximately 500 mm upstream of the model, so that its wake would not affect the airflow over the model to any great extent.

The position of the pitot-tube ensured measurement of "free-stream velocity", essentially unaffected by the presence of the model.

Pitot-tube : Airflow Developments
1,30 mm dia stagnation pressure
orifice.

Manometer : Betz-type projection manometer
v. Essen Delft 6750
least count 0,01 inches of water.

A.3 TEMPERATURE MEASUREMENT

The temperature of the airflow was measured using a standard laboratory mercury thermometer, protruding from the tunnel wall into the flow. This thermometer actually measured stagnation temperature, but since the velocities were relatively low, no correction was made to obtain true static temperature.

Thermometer : standard mercury-in-glass
least count 1,0°C.

A.4 STATIC PRESSURE MEASUREMENT

The wind-tunnel working section is provided with a slot, ensuring that static pressure in the tunnel is the same as ambient atmospheric pressure. The atmospheric pressure was measured using a standard Fortin barometer, previously calibrated by the National Physical Research Laboratory.

Barometer : Gallenkamp and Co. Ltd. No. 1110
least count 0,01 mm Hg
accuracy ± 0,1 mm Hg.

A.5 THE WIND-TUNNEL BALANCE

The wind-tunnel balance is an Aerolab Pyramidal Strain Gauge balance, designed to support a model in the wind-tunnel, adjust its angle of attack over a ± 30 degree range, adjust its angle of yaw over a 360 degree range, and separate and measure the six force and moment components which determine the resultant force exerted by the airflow on the model. The angular position of the model in yaw and angle of attack is indicated on Veeder Root counters to the nearest tenth of a degree.

The components are separated mechanically and measured through individual load cells; readout is accomplished through appropriate electrical equipment.

The basic linkage may be termed a pyramidal (or virtual centre) linkage. The central spider which carries the model support is supported on four diagonal struts which, if extended, would meet at a point known as the "balance centre". Since any movement of this central spider must occur as a rotation about the balance centre, moments are measured simply by a vertical or horizontal force, multiplied by its distance to the balance centre. This multiplication is of course effected in the linkage.

The load cells are equipped with strain gauge bridges composed of four active 120 ohm gauges. The bridges are energised by D.C. supplied by separate stabilised power supplies for each component. A wiring diagram for the power and control unit is presented in Figure A.2 overleaf.

Readout is by a Doric Digital Microvoltmeter, having a least count of one microvolt. Sensitivity is limited by electrical noise to $\pm$ 2 microvolts. Values of sensitivity for each of the force and moment components is given in Appendix B.

A.6 MEASUREMENT OF FLOATING-ANGLE OF THE AILERONS

It was obviously impossible to measure the floating angle of the ailerons directly in the wind-tunnel. Various indirect methods were considered, including a travelling microscope. Finally, it was decided to use a photographic method, this having the added advantage of creating a permanent record. The camera used was an Exa IIb, fitted with a Zeiss 2,8/50 lens. A film with a reasonably high ASA rating of 400 was used, enabling reasonable depth of field with one photographic flood light, and a shutter speed of 1/60th sec.

The developed negatives were projected in the projection rig described in Ref Ga 75, giving x and y co-ordinates of the trailing edge of the aileron, trailing edge of the wing, and floating-axis of the aileron.

A.7 MULTI-TUBE MANOMETER

In order to determine the pressure distribution of Model No. 2, use was made of a multi-tube manometer. It consists of a bank of thirty-six tubes, connected to a common reservoir. The bank of tubes may be tilted at angles of 0° to 70° to the vertical. For the purposes of the tests, the bank was tilted at 60° to the vertical, effectively doubling the sen-

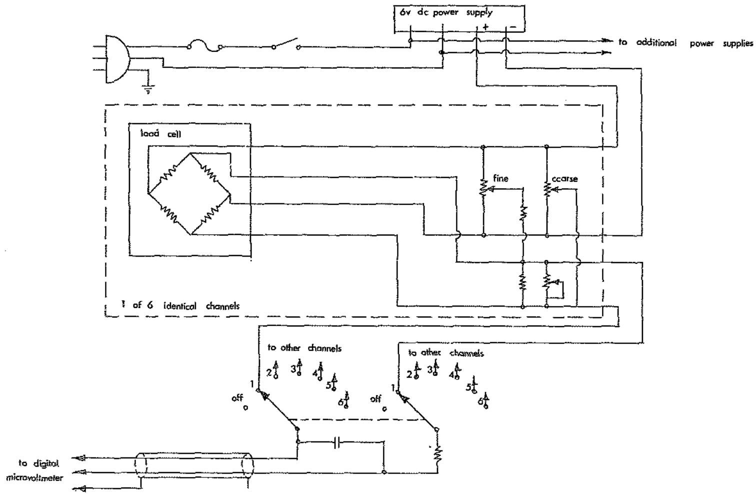

FIGURE A.2: Wiring Diagram for Power and Control Unit for Aerolab Wind-Tunnel Balance sitivity of the tubes.

Manometer least count = 0,05 inches water
(graduations of 0,1 inch, at 60° to the vertical)

A.8 MEASUREMENT OF ANGLE OF ATTACK (INCIDENCE) OF MODEL NO. 2

Since Model No. 2 was not mounted on the wind-tunnel balance, incidence could not be measured directly on the balance's Veeder Root counter. Movements of a reflected laser beam were used to measure, and set-up, Model No. 2 at various incidences. The calibration of this arrangement is given in Appendix B. Figure A.3 below shows a schematic view of the system.

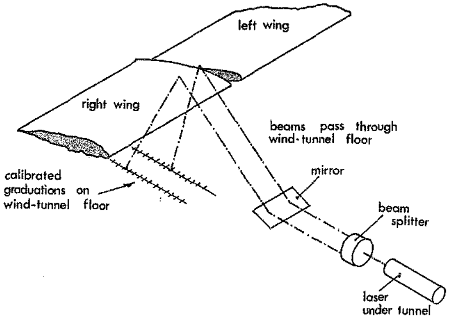

FIGURE A.3: Schematic View of Incidence-Measuring System of Model No. 2

Laser	:	Spectra-Physics Stablite Model 124A Helium-Neon Laser
Power source	:	Spectra-Physics 255 Exiter
Beam splitter	:	from T.S.I. Laser-Doppler System.

APPENDIX B

CALIBRATIONS

B.1 WIND-TUNNEL TEMPERATURE AND PITOT-PRESSURE/TIME CALIBRATION

It was found that when the wind-tunnel was used for extended periods at high speeds, its temperature rose, due to frictional and stagnation effects. The dynamic head of the airflow decreased due to the increase in temperature. It was therefore decided to calibrate the curve of these changes in parameters with time. This meant that it was only necessary to record the values of these parameters at the beginning of each test, and to record the duration of the test, instead of having to record the values at discrete time intervals.

The wind-tunnel was run up to operating speed, and values of temperature and pitot-pressure recorded for time intervals of three minutes. When twel[illegible] minutes had elapsed, further va[illegible] were recorded at ten minute intervals, until the temp[illegible]d pitot-pressure of the wind-tunnel had stabilis[illegible] test was repeated on the following day, when the ambi[illegible] temperature was five degrees Celcius lower, and it was found that the change in wind-tunnel stable temperature and pitot-pressure was negligible.

Due to the exponential nature of these parameter changes, exponential curves were fitted to the data points. The curves are shown overleaf in figures B.1 and B.2.

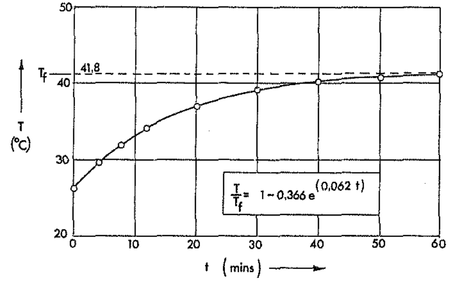

FIGURE B.1: Curve fit to Calibration Data: Wind-Tunnel Temperature vs Time

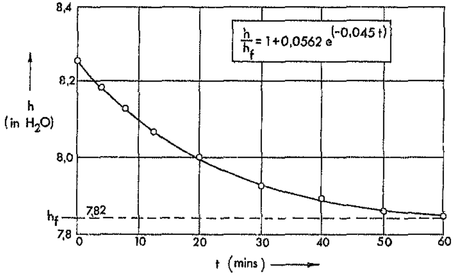

FIGURE B.2: Curve fit to Calibration Data: Wind-Tunnel Pitot-Head vs Time

B.2 WIND-TUNNEL BALANCE CALIBRATION

Before any tests were carried out in the wind-tunnel, it was decided to replace the load cells on the lift, side-force and drag components on the wind-tunnel balance, with more sensitive cells. After this replacement, the balance was aligned as recommended in the operating manual. The position of the resolving centre was determined by the use of fittings supplied with the balance. These consisted of four pointed rods, which were clamped to the spider struts, and met at the resolving centre. The alignment was checked by mounting a vertical cylindrical aluminium bar on the balance and running the wind-tunnel through its complete speed range. The balance provided an output of drag component and pitching-moment; but lift, side-force, rolling and yawing moments were essentially zero. The alignment was further checked during calibration.

Supplied with the balance was a calibration "tee", a "t" shaped bar having grooves at one-inch intervals. This was mounted on the balance using the fittings supplied. Stout cord was attached to the "tee", and passed over a 250 mm diameter pulley to a large scale pan. The apparatus is shown overleaf in figure B.3.

Standard masses were placed in the scale pan, and the pulley was moved until only lift and pitching-moment registered on the balance output voltmeter. The cord was checked with an accurate spirit level, and found to be vertical. This ensured that the three forces were orthogonal and aligned with the airflow direction in the tunnel. Moment cross-coupling was not checked for, since measurement of moments depended on the orthogonality of the three forces only.

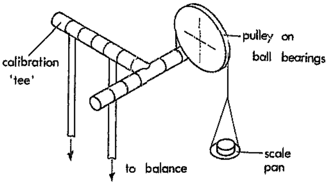

FIGURE B.3: The Balance Calibration Apparatus

Readings of the three forces and the three moments were then recorded, for varying masses in the scale pan, at varying positions on the "tee". The true moments were calculated (since moments were not applied *at* the resolving centre), and figures B.4 to B.9 represent the results. Data points are not shown for the unloading condition, since there was no observable hysterisis on any of the components.

Table B.1 contains all the relevant data for the wind-tunnel balance.

TABLE B.1: THE 600 x 900 SUBSONIC WIND-TUNNEL BALANCE

Load Cell Sensitivities:

Lift	282,04 $\mu V.lbf^{-1}$	63,39 $\mu V.N^{-1}$
Drag	302,56 $\mu V.lbf^{-1}$	68,01 $\mu V.N^{-1}$
Side-force	389,68 $\mu V.lbf^{-1}$	87,59 $\mu V.N^{-1}$
Pitching Moment	25,35 $\mu V.(lbf\ in)^{-1}$	224,33 $\mu V.(Nm)^{-1}$
Rolling Moment	31,51 $\mu V.(lbf\ in)^{-1}$	278,85 $\mu V.(Nm)^{-1}$
Yawing Moment	44,72 $\mu V.(lbf\ in)^{-1}$	395,75 $\mu V.(Nm)^{-1}$

Position of Resolving Centre = 385,64 mm from mounting flange.

Positive direction of components as registered on voltmeter:

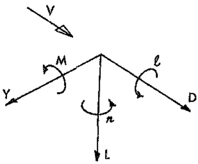

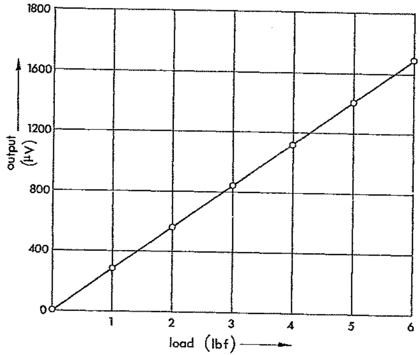

FIGURE B.4: Lift Cell Calibration

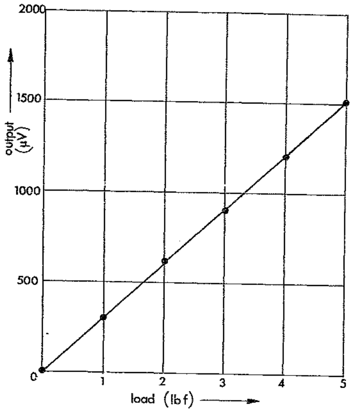

FIGURE B.5: Drag Cell Calibration

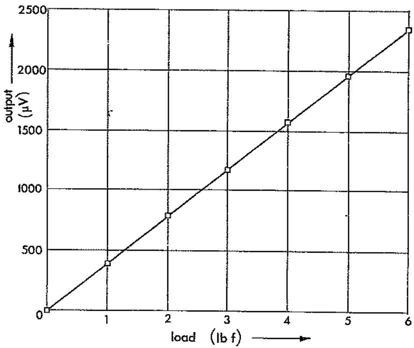

FIGURE B.6: Side-Force Cell Calibration

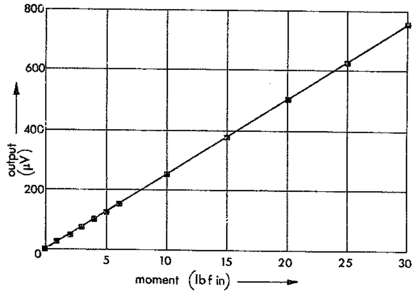

FIGURE B.7: Pitching Moment Cell Calibration

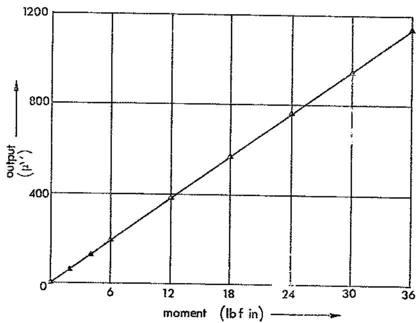

FIGURE B.8: Rolling Moment Cell Calibration

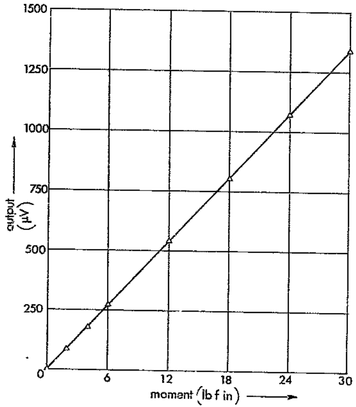

FIGURE B.9: Yawing Moment Cell Calibration

B.3 CALIBRATION OF MODEL NO. 1

When Model No. 1 was first tested in the wind-tunnel, it was found that there were some side-force, yawing and rolling moment components present due to machining imperfections. These forces and moments had to be corrected for when evaluating wind-tunnel data. Figures B.10 to B.12 below and overleaf show the data points obtained from the first wind-tunnel test, and the fitted curves.

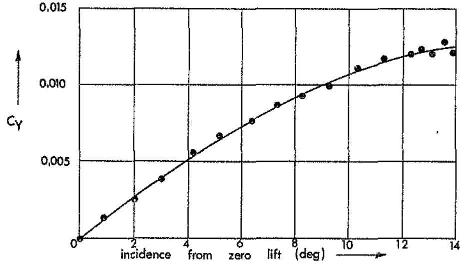

FIGURE B.10: Side-Force Calibration

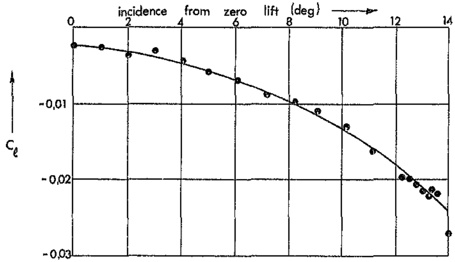

FIGURE B.11: Rolling Moment Calibration

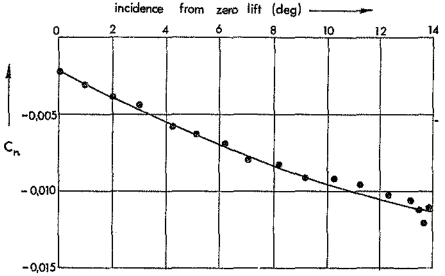

FIGURE B.12: Yawing Moment Calibration

B.4 CALIBRATION OF THE INCIDENCE MEASURING SYSTEM OF MODEL NO. 2

Model No. 2 was first assembled in the wind-tunnel. The bottom flat faces of the wings were set parallel to the wind-tunnel floor by the use of a vernier height gauge. This position was at eight degrees incidence from zero (six degrees from zero lift line to the chord line, and two degrees further to the bottom surface).

The laser was set up as in Appendix A, and the position of the reflected beams marked on the wind-tunnel floor. By lowering the trailing edges by a measured amount, the incidence of the wings were calibrated from zero lift (trailing edges eight degrees up fr reference), to ten degrees incidence (trailing edge down by two degrees), in steps of 2,5 degrees. At each incidence, the position of the reflected laser beams were marked on the wind-tunnel floor.

APPENDIX C

METHOD OF CALCULATION OF RESULTS

This appendix serves to explain the methods by which the results were calculated from raw experimental data. The computer programme referred to is listed in Appendix D.

C.1 MODEL NO. 1

The results for Model No. 1 are presented in the form of non-dimensional coefficients. Parameters common to all coefficients are density, velocity and wing area. Density was calculated using the ideal gas law, correcting temperature for heating effects. Velocity was calculated assuming 100 per cent conversion of dynamic head in the wind-tunnel to manometric height. Allowance was made for the change in pitot-pressure with time.

Forces and moments were converted to S.I. units using the calibration factors from Appendix B. The moments were corrected for displacement from the balance resolving centre, by assuming that the drag, side-force and lift vectors acted at the 40 per cent chord pivot point of the model (see figure C.1 overleaf).

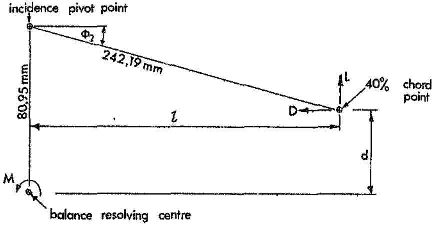

FIGURE C.1: Corrections for Displacement from Balance Resolving Centre

from figure C.1:

$l = 242{,}19 \cos \phi_2$

$d = 80{,}95 + 242{,}19 \sin \phi_2$

the corrected moments are:

$$M_c = M - L.l - D.d$$
$$\ell_c = \ell - Y.d \qquad \ldots\ldots\ldots\ldots \quad (C.1)$$
$$n_c = n - Y.l$$

The coefficients were then calculated, and incidence and drag coefficient were corrected for boundary-induced interference (as described in Chapter Four). The results were calculated using the computer programme DAVEXP, whose logic follows that described here.

C.2 MODEL NO. 2

Reference Re 61 gives pressure coefficient curves for varying lift coefficients, for the Clark Y aerofoil. Since the wind-tunnel tests on Model No. 2 were in the low-speed range, the velocity remained constant during each test. It was therefore possible to plot lift coefficient against suction pressure, from the curves of pressure coefficient in reference Re 61, for the test velocity and the 30 per cent chord position of the pressure tappings. Figure C.2 below is such a plot.

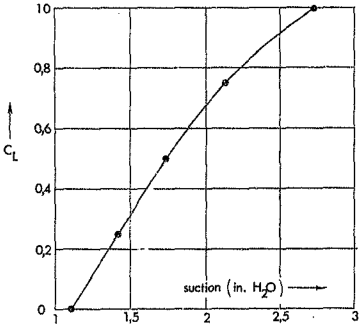

FIGURE C.2: Variation of Suction with Lift Coefficient for the 30% Upper Surface Chord Position of the Clark Y Aerofoil (taken from data presented in reference Re 61)

Suction readings were thus readily converted to local lift coefficients.

APPENDIX D

COMPUTER PROGRAMMES

D.1 DAVELIP

This programme evaluated the boundary-induced interference factor for the elliptic cross-section wind-tunnel of the University of the Witwatersrand. Essentially, there are four stages to the programme:

(i) convert x-y co-ordinates to elliptical co-ordinates.

(ii) sum series of odd terms for the interference on the wind-tunnel axis (see equation 4.6).

(iii) sum series of even terms for the interference off the wind-tunnel axis.

(iv) output.

Each series was judged to have converged when a term was smaller than 0,00001.

```
C
C      ------------------------------------------------------------------
C      PROGRAM TO CONVERT X-Y COORDINATES TO ELLIPTICAL;
C      THEN SUM SERIES GIVEN BY SANUKI & TANI FOR INTERFERENCE FACTORS
C      ON WITS WIND-TUNNEL.
C      ------------------------------------------------------------------
C      PARAMETERS USED;;
C      S=CORRECTED SEMI-SPAN, AR,BR=SEMI-MAJOR &MINOR AXES OF TUNNEL
C      A,B = SEMI-MAJOR & MINOR AXES OF ELLIPSE THRO' TRAILING VORTEX
C      AK = RATIO OF SPAN TO SEMI-MAJOR AXIS. H = HEIGHT OF WING ABOVE
C      TUNNEL MAJOR AXIS. C = CO-ORD OF FOCUS OF ELLIPSES.
C      DB=H/BR
C      ------------------------------------------------------------------
C
       INTEGER NAM(400)
       BR=25.4*12.
       AR=BR*1.5
       C=SQRT(AR**2-BR**2)
       READ(5,100)AK
       DO 900 LZ=1,5
       READ(5,104)NAM
       S=AK*AR
       WRITE(6,199)AK
       DB=0.001
       DO 700 KA=1,200
       H=DB*BR
C
C      ------------------------------------------------------------------
C      CONVERSION TO ELLIPTICAL COORDS
C      ------------------------------------------------------------------
       FACT1=S**2+H**2+C**2
       FACT2=FACT1**2-(4.*C**2*S**2)
       IF(FACT2)10,20,20
 20    ASQ=(FACT1+SQRT(FACT2))/2.
       A=SQRT(ASQ)
       B=SQRT(ASQ-C**2)
       XIO=(ALOG((AR+BR)/(AR-BR)))/2.
       XIDSH=(ALOG((A+B)/(A-B)))/2.
```

```
            ETADSH=ARCOS((S)/(C*COSH(XIDSH)))
            GO TO 7
     10     WRITE(6,111)
            STOP
      7     CONTINUE
            TCL=0.00001
            AKAP=0.
            AKAP1=0.
            AKAP2=0.
C
C     ------------------------------------------------------------
C     INTERFERENCE ON AXIS
C     ------------------------------------------------------------
            DO 500 I=1,100
            II=(2*I)-1
            AN=FLOAT(II)
            TERM1=(EXP(-AN*XIO))/(AN*COSH(AN*XIO))
            TERM2=(COSH(AN*XIDS'')**2
            TERM3=(COS(AN*ETADS
            SUM1=TERM1*TERM2*TER
            IF(SUM1-TCL)1,1,2
      2     AKAP1=AKAP1+SUM1
    500     CONTINUE
            IF(SUM1-TOL)1,1,5
C
C     ------------------------------------------------------------
C     INTERFERENCE OFF AXIS
C     ------------------------------------------------------------
      1     DO 600 J=1,100
            BN=FLOAT(2*J)
            TERM4=(EXP(-BN*XIO))/(BN*(SINH(BN*XIO)))
            TERM5=(SINH(BN*XIDSH))**2
            TERM6=(SIN(BN*ETADSH))**2
            SUM2=TERM4*TERM5*TERM6
            IF(SUM2-TOL)3,3,4
      4     AKAP2=AKAP2+SUM2
    600     CONTINUE
            IF(SUM2-TCL)3,3,5
```

```
    3     AKAP=AKAP1+AKAP2
          DELTA=(AKAP*BR)/(4.*AR*AK**2)
    C     ------------------------------------------------------------
    C     OUTPUT
    C     ------------------------------------------------------------
          WRITE(7,201)DB,DELTA
          DB=DB+0.001
  700     CONTINUE
          WRITE(7,104)NAM
          AK=AK+0.1
  900     CONTINUE
          STOP
    5     WRITE(6,200)
          STOP
  100     FORMAT(F5.2)
  104     FORMAT(80A1)
  111     FORMAT(20X,'ALL ROOTS IMAGINARY')
  199     FORMAT('K=',F3.1)
  200     FORMAT(1H1,/5X,'TOLERANCE NOT REACHED')
  201     FORMAT(2F13.5)
          END
```

D.2 DAVEXP

This programme, used to calculate wind-tunnel results from raw data, has been described in Appendix C. The programme is listed overleaf for reference.

```
FORTRAN IV G LEVEL  21              DAVEXP              DATE = 75321          09/59/15                PAGE 0001
                C
                C
                C        -------------------------------------------------------------------
                C        THIS PROGRAM CORRECTS WIND-TUNNEL DATA FOR BOUNDARY-INDUCED
                C        INTERFERENCE, AND FOR ORIENTATION OF MODEL.
                C
                C        PARAMETERS SUPPLIED ARE ATMOS PRESS(MM HG),INITIAL TEMP,(DEG C)
                C        INITIAL PITOT-STATIC PRESS(IN H2O),NO OF DATA POINTS, AND DURATION
                C         OF TEST
                C        DATA PARAMETERS SUPPLIED ARE BALANCE OUTPUT IN MILLIVOLTS,
                C        AND INCIDENCE FROM ZERO-LIFT, IN DEGREES.
                C        -------------------------------------------------------------------
                C        -------------------------------------------------------------------
                C
 0001                    INTEGER NAM(160),NT(7)
 0002                    REAL ALFA(7,35),D(7,35),SF(7,35),PM(7,35),YM(7,35),RM(7,35),LDIST,
                        $CL(7,35),CD(7,35),CSF(7,35),CPM(7,35),CRM(7,35),CYM(7,35),L(7,35)
                C
                C        -------------------------------------------------------------------
                C        INITIALISE VALUES
                C        -------------------------------------------------------------------
 0003                    REAL DF(6,3,4),DW(3,4),CLDS(4),W(3)
 0004                    R=287.26
 0005                    SSFAN=0.246
 0006                    TAREA=0.442
 0007                    BR=0.0254*12.
 0008                    A=0.0254*24.
 0009                    B=0.0254*36.
 0010                    SAREA=A*B
 0011                    P=P*9.81*13.4*1000.
 0012                    RHOW=1000.
 0013                    C=0.056
 0014                    AREA=C*0.492
 0015                    DS=AREA/4.
 0016                    DS=DS/(2.*(B**2))
 0017                    PHI1=-ARSIN(34.5/410.)
                C
                C        -------------------------------------------------------------------
```

```
              C      INPUT
              C      ---------------------------------------------------------------
0018                 READ(5,93)(((DF(I,J,K),K=1,4),J=1,3),I=1,6)
0019                 DO 1000 M=1,7
0020                 READ(5,90)P,T1,TIME,VH1,NT(M),NTEST
0021                 READ(5,92)SKEW,AIL
0022                 WRITE(6,103)NTEST
0023                 WRITE(6,100)SKEW,AIL
0024                 NM=NT(M)
0025                 DO 30 K=1,NM
0026                 READ(5,91)ALFA(M,K),L(M,K),D(M,K),PM(M,K),SF(M,K),YM(M,K),RM(M,K)
0027                 ALFA(M,K)=ALFA(M,K)*3.14159/180.
0028                 L(M,K)=-L(M,K)
0029                 SF(M,K)=-SF(M,K)
0030                 PM(M,K)=-PM(M,K)
0031                 YM(M,K)=-YM(M,K)
0032                 RM(M,K)=-RM(M,K)
              C
              C      ---------------------------------------------------------------
              C      CHANGE FORCES AND MOMENTS TO S.I. UNITS
              C      ---------------------------------------------------------------
0033                 L(M,K)=(L(M,K)*9.81)/(282.04*2.205)
0034                 D(M,K)=(D(M,K)*9.81)/(302.56*2.205)
0035                 SF(M,K)=(SF(M,K)*9.81)/(389.68*2.205)
0036                 PM(M,K)=(PM(M,K)*9.81*0.0254)/(25.35*2.205)
0037                 RM(M,K)=(RM(M,K)*9.81*0.0254)/(31.51*2.205)
0038                 YM(M,K)=(YM(M,K)*9.81*0.0254)/(44.715*2.205)
              C
              C      ---------------------------------------------------------------
              C      CORRECTIONS TO DISPLACEMENT FROM RESOLVING CENTRE
              C      ---------------------------------------------------------------
0039                 PHI2=PHI1+ALFA(M,K)
0040                 H=0.24219*SIN(PHI2)
0041                 LDIST=0.24219*COS(PHI2)
0042                 DDIST=0.08095+0.24219*SIN(PHI2)
0043                 PM(M,K)=PM(M,K)-L(M,K)*LDIST-D(M,K)*DDIST
0044                 SDIST=DDIST
0045                 RM(M,K)=RM(M,K)-SDIST*SF(M,K)
```

```
0046              YM(M,K)=YM(M,K)-SF(M,K)*LDIST
            C
            C     ----------------------------------------------------------------
            C     CORRECT FOR TEMPERATURE-TIME
            C     ----------------------------------------------------------------
0047              TM=TIME*FLOAT(K)/FLOAT(NT(M))
0048              TF=41.8
0049              TM1=(-41.8/2.6)*ALOG(((T1/TF)-1.)/(-0.366))
0050              T=1.-0.366*EXP((-2.6/41.8)*(TM-TM1))
0051              T=T*TF
0052              T=T+273.
0053              RHOA=P/(R*T)
            C
            C     ----------------------------------------------------------------
            C     CORRECT FOR PITOT-PRESSURE-TIME
            C     ----------------------------------------------------------------
0054              HF=7.82
0055              TH1=(1./(-0.045))*ALOG(((VH1/HF)-1.)/0.05627)
0056              VH=1.+0.05627*EXP((-0.045)*(TM-TH1))
0057              VH=VH*7.82
0058              V=SQRT((2.*RHOW*9.81*25.4*0.001)/(RHOA))
0059              V=V*SQRT(VH)
0060              Q=(RHOA*(V**2.))/2.
0061              RF=Q*AREA
            C
            C     ----------------------------------------------------------------
            C      CHANGE TO COEFFICIENTS
            C     ----------------------------------------------------------------
0062              CL(M,K)=L(M,K)/RF
0063              CD(M,K)=D(M,K)/RF
0064              CSF(M,K)=SF(M,K)/RF
0065              CPM(M,K)=PM(M,K)/(RF*C)
0066              CRM(M,K)=RM(M,K)/(RF*SSPAN)
0067              CYM(M,K)=YM(M,K)/(RF*SSPAN)
0068              CSF(M,K)=CSF(M,K)+0.0002093-0.001482*ALFA(M,K)+0.00004164*((ALFA(M
                 $,K))**2)
0069              CRM(M,K)=CRM(M,K)+0.00228-0.00001397*ALFA(M,K)+0.0001146*((ALFA(M,
                 $K))**2)
```

```
0070           CYM(M,K)=CYM(M,K)+0.002276+0.0007998*ALFA(M,K)-0.000009938*((ALFA(
              $M,K))**2)
          C
          C    --------    ------------------------------------------------------
          C    CORREC'       BOUNDARY-INDUCED INTERFERENCE
          C    ------      ------------------------------------------------------
0071           IF(CLL.           23,9
0072       23  DELTA=0.
0073           GO TO 25
0074        9  IF(SKEW)20,10,20
          C
          C     ----------------------------------------------------------------
          C     CORRECTION TO UN-SKEWED CASE , USING CURVE FIT TO SANUKI AND TANI
          C    DATA
          C     ----------------------------------------------------------------
0075       10  HB=H/BR
0076           DELTA=0.104736-0.0001771906*HB+0.2258559*(HB)**2
0077           GO TO 25
          C
          C    -----------------------------------------------------------------
          C    CORRECTION TO SKEWED CASE, USING INTERPOLATED RECTANGULAR
          C    WIND-TUNNEL DATA
          C    -----------------------------------------------------------------
0078       20  FACT1=SQRT(1.-(0.75)**2)
0079           FACT2=SQRT(1.-(0.25)**2)
0080           CLO=2.*CL(M,K)/(FACT1+FACT2)
0081           CL1=CLO*FACT1
0082           CL2=CLO*FACT2
0083           CL3=CL2
0084           CL4=CL1
0085           CLDS(1)=CL1*DS
0086           CLDS(2)=CL2*DS
0087           CLDS(3)=CL3*DS
0088           CLDS(4)=CL4*DS
0089           IS=IFIX(SKEW/10.)
0090           DO 505 IA=1,3
0091           DO 506 IM=1,4
0092           DW(IA,IM)=CLDS(IM)*DF(IS,IA,IM)
```

```
0093      506  CONTINUE
C094           W(IA)=0.0
0095      505  CONTINUE
0096           DO 510 IB=1,3
0097           DO 511 IN=1,4
0098           W(IB)=W(IB)+DW(IB,IN)
0099      511  CONTINUE
0100      510  CONTINUE
0101           WMEAN=(W(1)+W(2)+W(3))/3.
0102           SDELT=(SAREA*WMEAN)/(AREA*CL(M,K))
0103           HB=H/BR
0104           DELT=0.104736-0.0001771906*HB+0.2258559*(HB)**2
0105           RRATO=SDELT/0.2402
0106           DELTA=DELT*RRATO
0107     25    CD(M,K)=CD(M,K)+DELTA*(AREA/TAREA)*(CL(M,K)**2)
0108           ALFA(M,K)=ALFA(M,K)+DELTA*AREA*CL(M,K)/TAREA
0109           ALFA(M,K)=ALFA(M,K)*180./3.14159
         C
         C     ------------------------------------------------------------
         C     OUTPUT
         C     ------------------------------------------------------------
0110           WRITE(6,101)ALFA(M,K),CL(M,K),CD(M,K),CSF(M,K),CPM(M,K),CYM(M,K),C
              $RM(M,K)
0111      30   CONTINUE
0112      1000 CONTINUE
0113           DO 2000 IZ=1,7
0114           READ(5,104)NAM
0115           NZ=NT(IZ)
0116           DO 50 JK=1,NZ
0117           WRITE(7,105)ALFA(IZ,JK),CL(IZ,JK)
0118      50   CONTINUE
0119           WRITE(7,104)NAM
0120      2000 CONTINUE
0121           DO 2001 IX=1,2
0122           READ(5,104)NAM
0123           NX=NT(IX)
0124           DO 51 JI=1,NX
0125           WRITE(7,105)ALFA(IX,JI),CD(IX,JI)
```

```
51    CONTINUE
      WRITE(7,104)NAM
2001  CONTINUE
      DO 2002 IY=1,7
      READ(5,104)NAM
      NY=NT(IY)
      DO 52 JL=1,NY
      WRITE(7,105)ALFA(IY,JL),CSF(IY,JL)
52    CONTINUE
      WRITE(7,104)NAM
2002  CONTINUE
      DO 2003 IV=1,7
      READ(5,104)NAM
      NV=NT(IV)
      DO 53 JM=1,NV
      WRITE(7,105)ALFA(IV,JM),CPM(IV,JM)
53    CONTINUE
      WRITE(7,104)NAM
2003  CONTINUE
      DO 2004 IU=1,7
      READ(5,104)NAM
      NU=NT(IU)
      DO 54 JN=1,NU
      WRITE(7,105)ALFA(IU,JN),CYM(IU,JN)
54    CONTINUE
      WRITE(7,104)NAM
2004  CONTINUE
      DO 2005 IT=1,7
      READ(5,104)NAM
      NTT=NT(IT)
      DO 55 JJ=1,NTT
      WRITE(7,105)ALFA(IT,JJ),CRM(IT,JJ)
55    CONTINUE
      WRITE(7,104)NAM
2005  CONTINUE
      STOP
C
C     -----------------------------------------------------------------
```

```
FORTRAN IV G LEVEL  21               DAVEXP            DATE = 75321          09/59/15           PAGE 0007

                   C      FORMAT STATEMENTS
                   C      ------------------------------------------------------------
 0162               90    FORMAT(F6.2,F5.2,F4.1,F5.3,I2,I3)
 0163               91     FORMAT(F5.1,6F7.1)
 0164               92    FORMAT(F4.1,F5.1)
 0165               93    FORMAT(12F5.3)
 0166              100    FORMAT(/5X,'CORRECTED WIND-TUNNEL DATA',//5X,'SKEW ANGLE=',F4.1,'
                         $DEG   ;   AILERON DIFFERENTIAL= ',F5.1,' DEG',//5X,'ALFA',10X,'CL'
                         $,11X,'CD',10X,'CSF',10X,'CPM',8X,'CYM',9X,'CRM')
 0167              101    FORMAT(3X,F5.2,4X,6F12.4)
 0168              103    FORMAT(1H1,20X,'TEST NO ',I3)
 0169              104    FORMAT(80A1)
 0170              105    FORMAT(2F12.4)
 0171                     END
```

D.3 DAVSPAN

The floating angles of the ailerons, and the wing performance were predicted, using solutions to the Monoplane Equation, by this programme. The floating angles of the ailerons were determined by solving

$$\int_{\text{aileron}} (\text{lift across symmetrical aerofoil section}) = 0 \quad . \quad . \quad (D.1)$$

using the method of false position (Ge 70). Generally, the solution to

$$y = f(x) = 0 \quad . \; . \; . \; . \; . \; . \; . \; . \; . \; . \; . \; . \; . \quad (D.2)$$

is sought.

Two "first guesses" at solutions are made; (x_1, y_1) and (x_2, y_2) such that

$y_2 > 0 \quad y_1 < 0$ and $x_2 > x_1$ (see figure D.1 below)

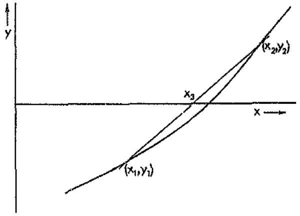

FIGURE D.1

The point where the straight line between (x_1, y_1) and (x_2, y_2) crosses the x-axis is used as the x-value of the next approximation to the solution. For the floating angle case, y is the integrated lift across the aileron, and x is the floating angle.

The programme logic is represented in the flow chart below.

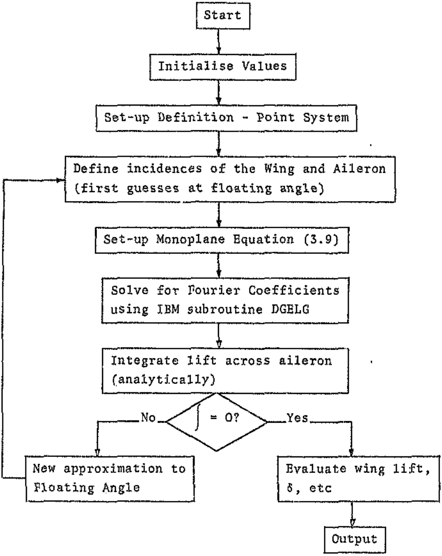

In order to reduce round-off errors, the programme was written for double length, eight character words (double precision).

It was found that the first intercept on the x-axis proved to be the solution to (D.2), within the specified tolerance of 0,001: i.e. the lift across the aileron was a linear function of aileron incidence.

```
                 C
                 C     ------------------------------------------------------------
                 C     THIS PROGRAM DETERMINES THE FLOATING ANGLE OF FLOATING-TIP
                 C     AILERONS, USING SUCCESSIVE SOLUTIONS TO THE MONOPLANE EQUATION
                 C     AND THE METHOD OF FALSE POSITION
                 C     ------------------------------------------------------------
0001                   IMPLICIT REAL*8 (A-H,O-Z)
0002                   REAL*8 A(37,37),R(37),Y(37)
0003                   REAL*8 LIFT
                 C     ------------------------------------------------------------
                 C     INITIALISE VALUES
                 C     ------------------------------------------------------------
0004                   READ(5,100)SLOP,AO,CHORD,SSPAN
0005                   READ(5,101)DIFF,AWING
0006                   PI=3.*DARCOS(0.5D0)
0007                   DEGRAD=PI/180.
0008                   SLOP=SLOP/DEGRAD
0009                   ASR=2.*SSPAN/CHORD
0010                   AWING=AWING*DEGRAD
0011                   AMUW=(CHORD*SLOP)/(8.*SSPAN)
0012                   AMUA=(CHORD*0.083)/(8.*SSPAN*DEGRAD)
                 C     ------------------------------------------------------------
                 C     DEFINITION OF SPANWISE DISTRIBUTION OF POINTS
                 C     ------------------------------------------------------------
                 C     NA=NO OF POINTS ON AILERON
0013                   NA=7
                 C     NW=NO OF POINTS ON WING
0014                   NW=23
0015                   NP=NW+2*NA
0016                   FACT=10.5
0017                   DO 76 IAIL=1,5
0018                   Y(1)=-243.
0019                   SPACE=((2.*SSPAN)-90.-2.*FACT)/DFLOAT(NW-1)
0020                   AILSP=(45.-(SSPAN+Y(1))-FACT)/(DFLOAT(NA-1))
0021                   DO 62 IK=2,NA
0022                   Y(IK)=Y(IK-1)+AILSP
0023              62   CONTINUE
0024                   DO 60 IJ=1,NA
```

```
0025            IK=IJ-1
0026            Y(NP-IK)=-Y(IJ)
0027       60   CONTINUE
          C     N1 IS MAX POINT ON WING
0028            N1=NW+NA
          C     N1W IS 1ST POINT ON WING
0029            N1W=NA+1
0030            NM=(NP+1)/2
0031            DO 72 IW=N1W,N1
0032            LW=IW-NM
0033            Y(IW)=DFLOAT(LW)*SPACE
0034       72   CONTINUE
          C     ----------------------------------------------------------
          C     DEFINITION OF INCIDENCES OF WING AND AILERON
          C     ----------------------------------------------------------
0035            AAIL1=-8.*DEGRAD
0036            AAIL2=DEGRAD
0037            LL=0
0038      444   LL=LL+1
0039            IF(LL.EQ.1)GO TO 30
0040            IF(LL.EQ.2)GO TO 31
0041            IF(LL.EQ.100)GO TO 69
0042            AAIL=AAILF
0043            GO TO 33
0044       30   AAIL=AAIL1
0045            GO TO 33
0046       31   AAIL=AAIL2
0047       33   CONTINUE
0048            DO 10 K=1,NP
0049            THETA=DARCOS(-Y(K)/SSPAN)
0050            IF(DABS(Y(K))-201.)50,50,51
0051       51   IF(Y(K))55,55,54
0052       55   ALFA=AAIL
0053            AMU=AMUA
0054            GO TO 52
0055       54   ALFA=AAIL
0056            AMU=AMUA
0057            GO TO 52
```

```
   50 ALFA=AWING
      AMU=AMUW
C     ------------------------------------------------------------
C     SET UP MONOPLANE EQUATION
C     ------------------------------------------------------------
   52 DO 20 M=1,NP
      A(K,M)=DSIN(DFLOAT(M)*THETA)*(DSIN(THETA)+DFLOAT(M)*AMU)
      R(K)=AMU*DSIN(THETA)*(ALFA)
   20 CONTINUE
   10 CONTINUE
C     ------------------------------------------------------------
C     GAUSSIAN ELIMINATION OF MATRIX - TO FIND FOURRIER COEFFS
C     ------------------------------------------------------------
      N=1
      EPS=0.1D-10
      CALL DGELG(R,A,NP,N,EPS,IER)
      WRITE(6,150)IER
C     ------------------------------------------------------------
C     INTEGRATE ALONG AILERON SPAN
C     ------------------------------------------------------------
      CALL AEL(R,CLA,NP)
      IF(DABS(CLA).LT.0.0001)GO TO 70
      IF(LL.EQ.1)GO TO 34
      IF(LL.EQ.2)GO TO 35
      GO TO 68
   34 CLA1=CLA
      GO TO 444
   35 CLA2=CLA
      GO TO 67
   68 IF(CLA2*CLA)65,70,66
   65 AAIL1=AAILF
      GO TO 67
   66 AAIL2=AAILF
C     AAILF IS NEW APPROXIMATION
   67 AAILF=(CLA1*AAIL2-CLA2*AAIL1)/(CLA1-CLA2)
      GO TO 444
   69 WRITE(6,106)
   70 AILI=AAIL/DEGRAD
```

```
FORTRAN IV G LEVEL  21                    DAVSPAN              DATE = 75322          11/28/27                PAGE 0004

 0086               AW=AWING/DEGRAD
 0087               DELTA=0.0
 0088               DO 80 I=3,NP,2
 0089               DELTA=DELTA+DFLOAT(I)*(R(I)**2)
 0090          80   CONTINUE
 0091               DELTA=DELTA/(R(1)**2)
 0092               CLW=PI*ASR*R(1)
 0093               WRITE(6,107)AW,AILI,LL,CLW,DELTA,FACT
 0094               FACT=FACT-0.5
 0095          76   CONTINUE
 0096               STOP
              C     ------------------------------------------------------------
              C     FORMAT STATEMENTS
              C     ------------------------------------------------------------
 0097         100   FORMAT(F7.5,F6.3,F5.2,F6.2)
 0098         101   FORMAT(2F5.2)
 0099         106   FORMAT(//5X,'100 STEPS')
 0100         107   FORMAT(/2F15.3,8X,I2,2F15.3,F6.1)
 0101         150   FORMAT(I2)
 0102         206   FORMAT(2X,F4.1,3F20.4)
 0103         207   FORMAT(2X,'ALPHA',16X,'CL',16X,'CRM',16X,'CYM')
 0104         208   FORMAT(1H1,20X,'AILERON DIFFERENTIAL=',F5.2,' DEG')
 0105         300   FORMAT(1H1,2X,'WING INCIDENCE   FLOATING ANGLE   ITERATIONS   CLW
                   $        DELTA')
 0106               END
```

```
0001              SUBROLTINE AEL(R,Y,NP)
           C      ------------------------------------------------------------------
           C      SUBROLTINE TO INTEGRATE ACROSS AILERON
           C      ------------------------------------------------------------------
0002              IMPLICIT REAL*8 (A-H,O-Z)
0003              REAL*8 R(37)
0004              SSPAN=246.
0005              CHORD=56.
0006              PI=3.0*DARCOS(0.5D0)
0007              THETA=DARCOS(-201.D0/SSPAN)
0008              TERM1=PI*R(1)/2.
0009              TERM1=TERM1-R(1)*(THETA/2.-(DSIN(2.0D0*THETA))/4.)
0010              T2=0.0
0011              DO 10 N=2,NP
0012              TERM2=(DSIN(DFLOAT(N-1)*THETA))/(2.*DFLOAT(N-1))
0013              TERM3=(DSIN(DFLOAT(N+1)*THETA))/(2.*DFLOAT(N+1))
0014              T2=T2+R(N)*(TERM2-TERM3)
0015        10    CONTINUE
0016              Y=TERM1-T2
0017              Y=(Y*8.*(SSPAN**2))/CHORD
0018              RETURN
0019              END
```

APPENDIX E

ERROR ANALYSIS

The accuracy of the observations is limited by the accuracy of the measuring instruments used. This appendix lists the probable errors in the various parameters, and an estimation of the final accuracy of the non-dimensional coefficients is given.

As an example, consider the lift coefficient error. The lift coefficient is given by:

$$C_L = \frac{L}{\frac{1}{2}\rho\ V^2\ S} \qquad \text{(E.1)}$$

In partial differential form, the error dC_L due to errors in other parameters may be written as:

$$dC_L = \left|\frac{\partial C_L}{\partial L}\right| . dL + \left|\frac{\partial C_L}{\partial \rho}\right| . d\rho + \left|\frac{\partial C_L}{\partial V^2}\right| . dV^2$$

$$+ \left|\frac{\partial C_L}{\partial S}\right| dS \qquad \text{(E.2)}$$

Now the error in density $d\rho$ depends on the error in static pressure and temperature measurement.

Using the Ideal Gas Law:

$$\rho = \frac{p}{RT} \qquad \text{(E.3)}$$

$$d\rho = \left|\frac{\partial \rho}{\partial p}\right| . dp + \left|\frac{\partial \rho}{\partial T}\right| . dT \qquad \text{(E.4)}$$

(assuming no error in R).

Since velocity was measured using a pitot-tube/manometer system:

$$\tfrac{1}{2}\rho\ V^2 = \rho_w\ gh$$

or

$$V^2 = \frac{2\rho_w}{\rho}\ gh \qquad \ldots\ldots\ldots\ldots\ldots \text{(E.5)}$$

hence

$$dV^2 = \left|\frac{\partial V^2}{\partial \rho}\right| .d\rho + \left|\frac{\partial V^2}{\partial h}\right| dh \qquad \ldots\ldots\ldots\ldots \text{(E.6)}$$

(assuming no error in ρ_w and g)

hence (E.2) becomes:

$$\begin{aligned} dC_L = & \left|\frac{\partial C_L}{\partial L}\right| .dL + \left|\frac{\partial C_L}{\partial \rho}\right| \{\left|\frac{\partial \rho}{\partial p}\right| .dp + \left|\frac{\partial \rho}{\partial T}\right| .dT\} \\ & + \left|\frac{\partial C_L}{\partial V^2}\right| \{\left|\frac{\partial V^2}{\partial \rho}\right. .d\rho + \left|\frac{\partial V^2}{\partial h}\right| dh\} \\ & + \left|\frac{\partial C_L}{\partial S}\right| .dS \qquad \ldots\ldots\ldots\ldots \text{(E.7)} \end{aligned}$$

Table E.1 overleaf lists the values of the errors and Table E.2 lists the values of the differentials in equation (E.7), at the highest values of the respective parameters.

TABLE E.1

Parameter	Reading Error	Instrument Error	Total
L	0,05 N	0,08 N	0,13 N
D	0,015 N	0,035 N	0,05 N
Y	0,035 N	0,055 N	0,09 N
M	0,013 Nm	0,068 Nm	0,081 Nm
ℓ	0,011 Nm	0,05 Nm	0,061 Nm
n	0,008 Nm	0,03 Nm	0,038 Nm
T	0,1 K	0,1 K	0,2 K
p	1,33 Pa	13,3 Pa	14,6 Pa
ρ	from p and T		$1,04\times10^{-4}$ kg m^{-3}
h	5×10^{-5} m H_2O	2×10^{-3} m H_2O	2,05 mm H_2O
S	$1,6\times10^{-8}$ m^2	-	$1,6\times10^{-8}$ m^2

TABLE E.2

$\frac{\partial C_L}{\partial L} = 0,021$ per N	$\frac{\partial \rho}{\partial T} = 3,32\times10^{-4}$ Pa K^{-1}
$\frac{\partial C_L}{\partial \rho} = -0,975$ per kg m^{-3}	$\frac{\partial V^2}{\partial \rho} = 0,43$ kg ms^{-2}
$\frac{\partial C_L}{\partial V^2} = -0,0003$ per m^2 s^{-2}	$\frac{\partial V^2}{\partial h} = 2,05\times10^4$ ms^{-2}
$\frac{\partial C_L}{\partial S} = -33,32$ per m^2	$\frac{\partial \rho}{\partial p} = 1,16\times10^{-5}$ kg m^{-3} Pa^{-1}

Substituting these values into equation (E.7) yields

$$dC_L = \underset{L}{2,73\times10^{-3}} + \underset{\rho}{2,3\times10^{-4}} + \underset{V^2}{1,26\times10^{-2}} + \underset{S}{5,33\times10^{-2}} = 1,56\times10^{-2}$$

this is the error at $C_L = 1$.

Percentage error = 1,56%.

As may be seen, this error is primarily due to the error in velocity squared, which is common to all non-dimensional coefficients. The other errors are at least an order of magnitude smaller. It may therefore be said that all coefficients have a maximum error of 2%.

APPENDIX F

EXPERIMENTAL RESULTS

This appendix contains all the calculated experimental results for the wind-tunnel models. The raw data is not presented here, but is on file in the School of Mechanical Engineering for reference.

F.1 EXPERIMENTAL RESULTS : WIND-TUNNEL MODEL NO. 1

These results are presented in seven sets of : lift, drag, side-force, pitching moment, rolling moment and yawing moment coefficients versus incidence from zero lift, at varying skew angles; each set for constant aileron differential.

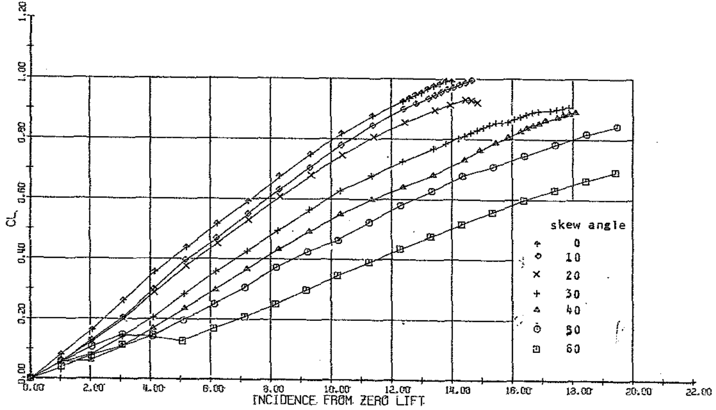

FIGURE F.1 Effect of Skew on Lift Coefficient; Aileron Differential = 0 deg.

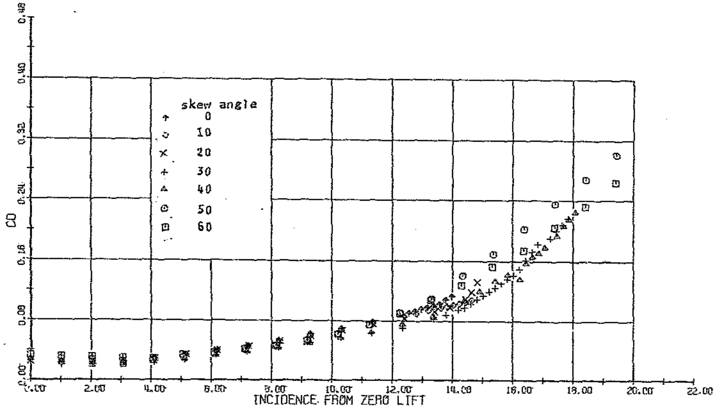

FIGURE F.2 Effect of Skew on Drag Coefficient; Aileron Differential = 0 deg.

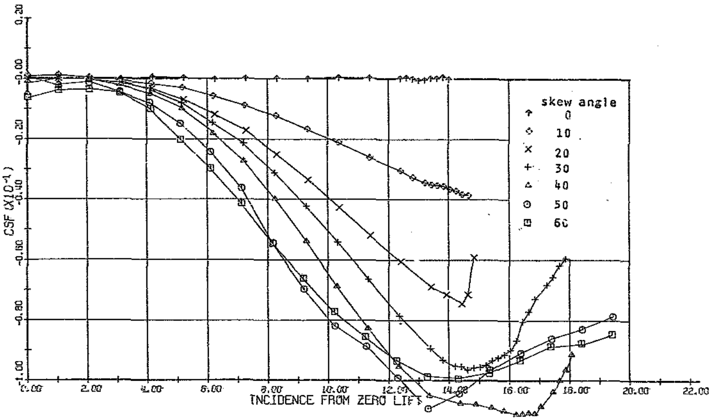

FIGURE F.3 Effect of Skew on Side-Force Coefficient; Aileron Differential = 0 deg

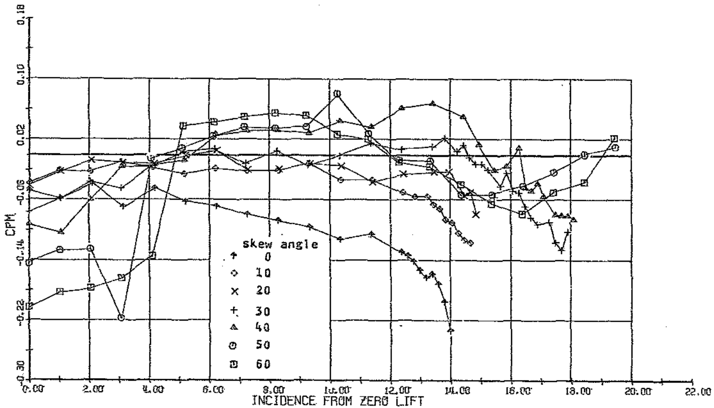

FIGURE F.4 Effect of Skew on Pitching-Moment Coefficient; Aileron Differential = 0 deg

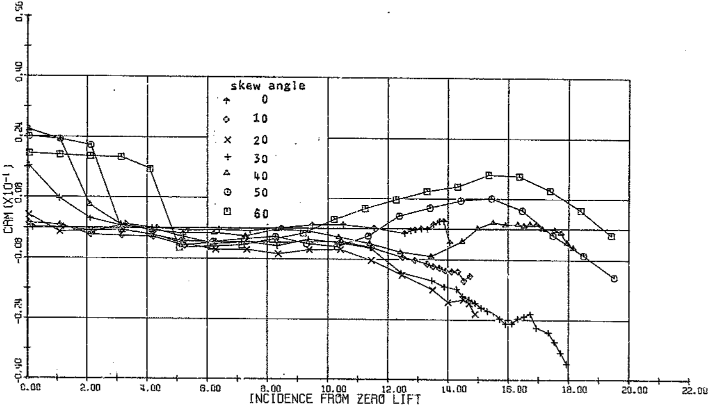

FIGURE F.5 Effect of Skew on Rolling-Moment Coefficient; Aileron Differential = 0 deg

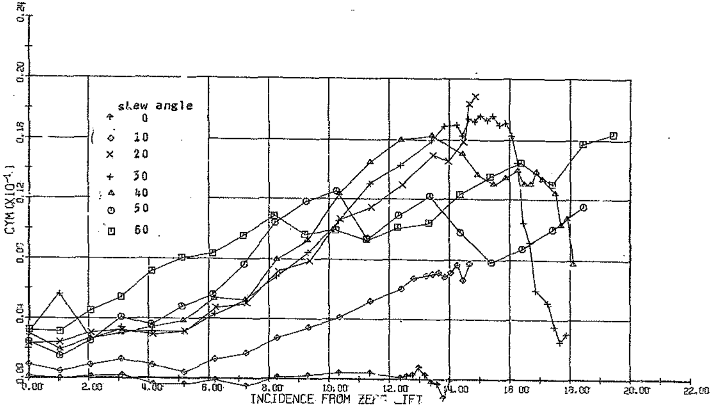

FIGURE F.6 Effect of Skew on Yawing Moment Coefficient; Aileron Differential = 0 deg

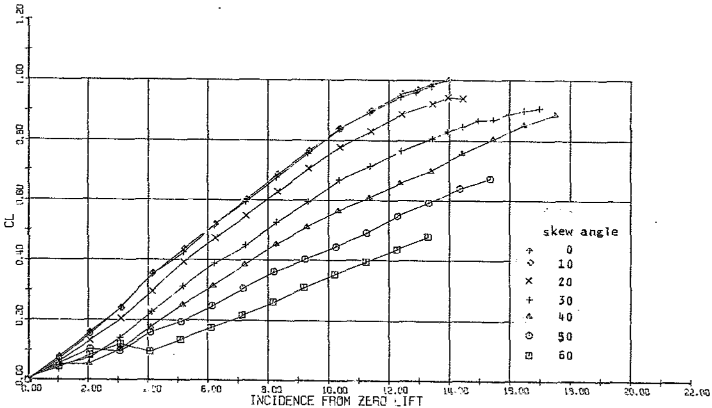

FIGURE F.7 Effect of Skew on Lift Coefficient; Aileron Differential = 5 deg

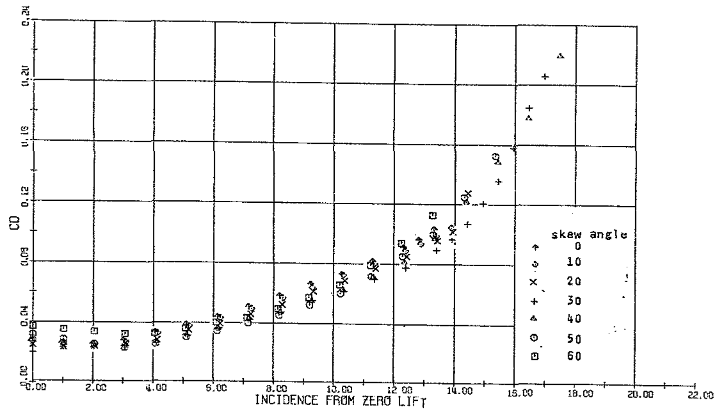

FIGURE F.8 Effect of Skew on Drag Coefficient; Aileron Differential = 5 deg

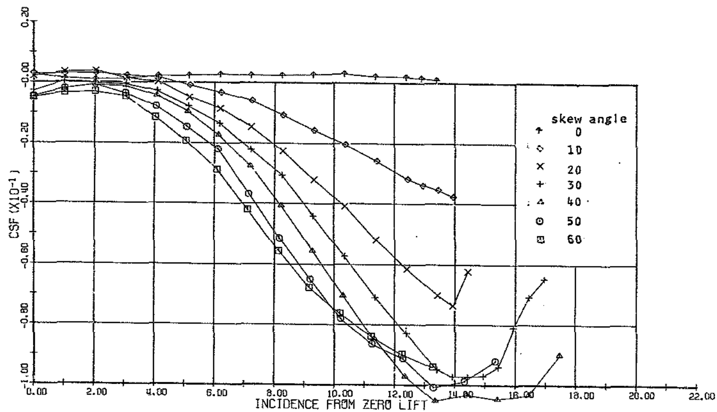

FIGURE F.9 Effect of Skew on Side-Force Coefficient, Aileron Differential = 5 deg

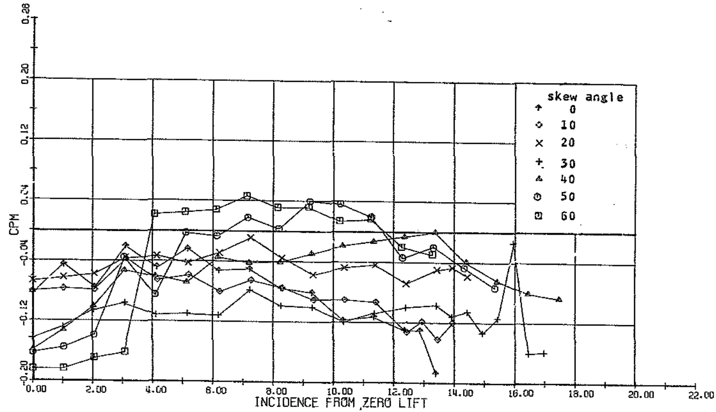

FIGURE F.10 Effect of Skew on Pitching Moment Coefficient; Aileron Differential = 5 deg

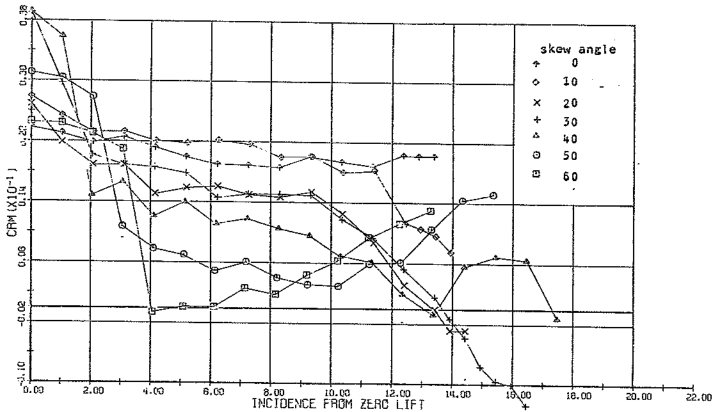

FIGURE F.11 Effect of Skew on Rolling Moment; Aileron Differential = 5 deg

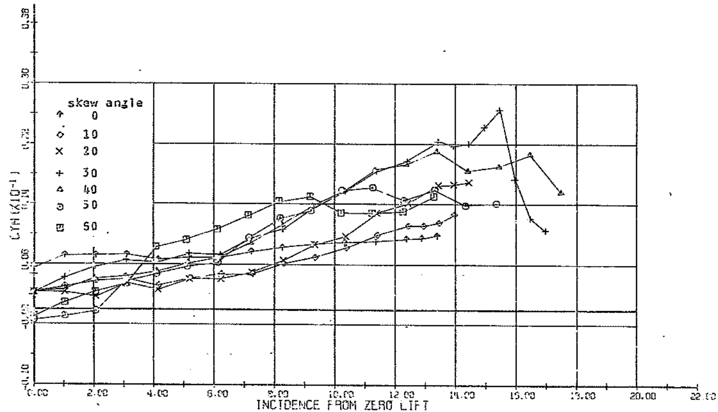

FIGURE F.12 Effect of Skew on Yawing Moment Coefficient; Aileron Differential = 5 deg

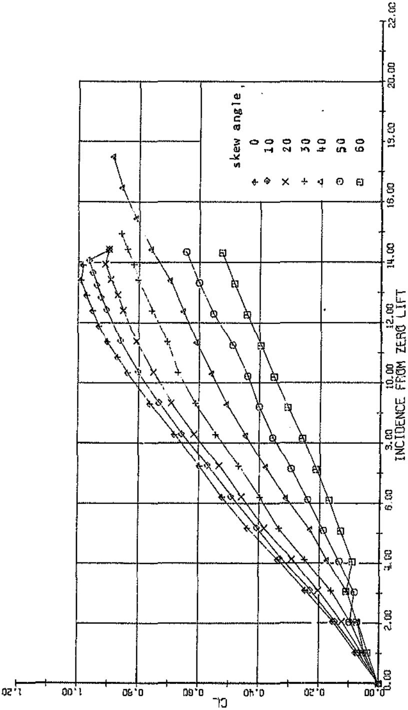

FIGURE F.13 Effect of Skew on Lift Coefficient; Aileron Differential = -5 deg

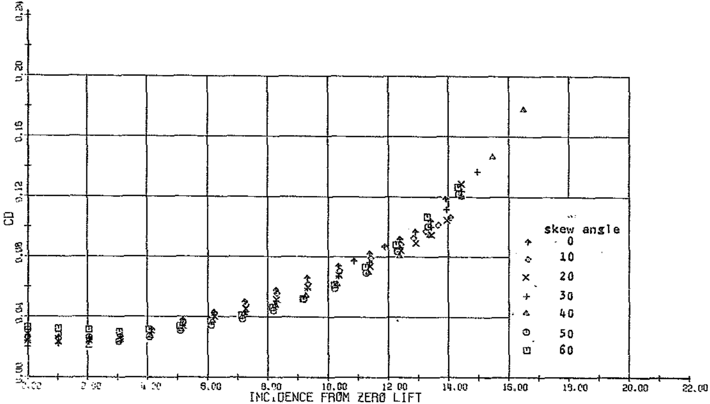

FIGURE F.14 Effect of Skew on Drag Coefficient; Aileron Differential = -5 deg

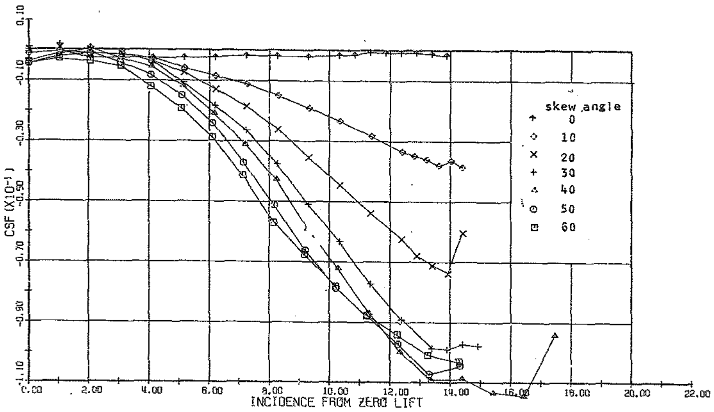

FIGURE F.15 Effect of Skew on Side-Force Coefficient; Aileron Differential = -5 deg

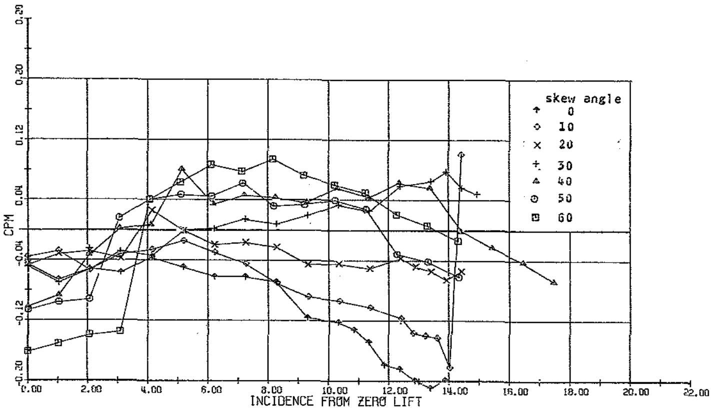

FIGURE F.16 Effect of Skew on Pitching Moment Coefficient; Aileron Differential = -5 deg

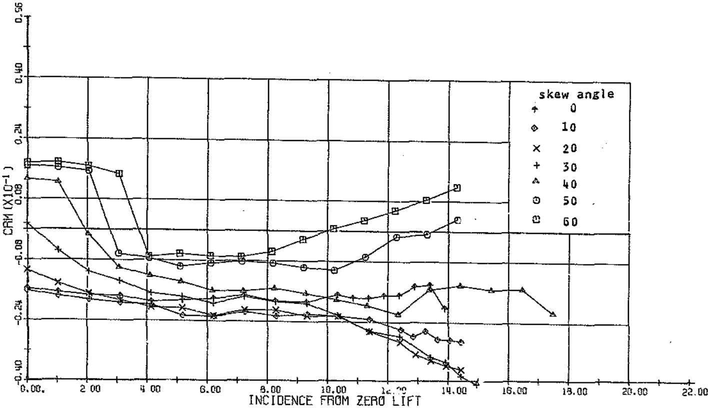

FIGURE F.17 Effect of Skew on Rolling Moment Coefficient; Aileron Differential = -5 deg

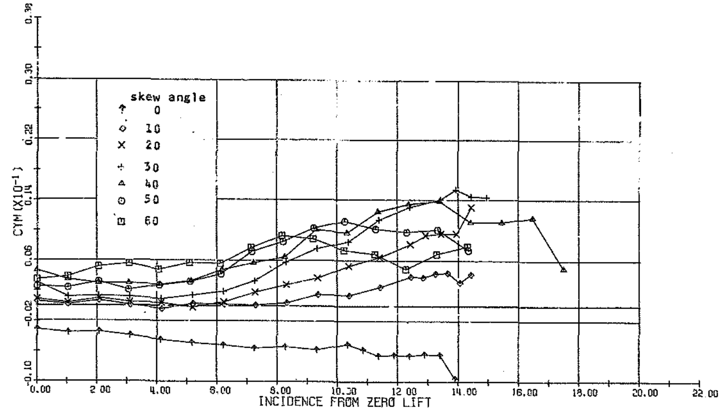

FIGURE F.18 Effect of Skew on Yawing Moment Coefficient; Aileron Differential = -5 deg

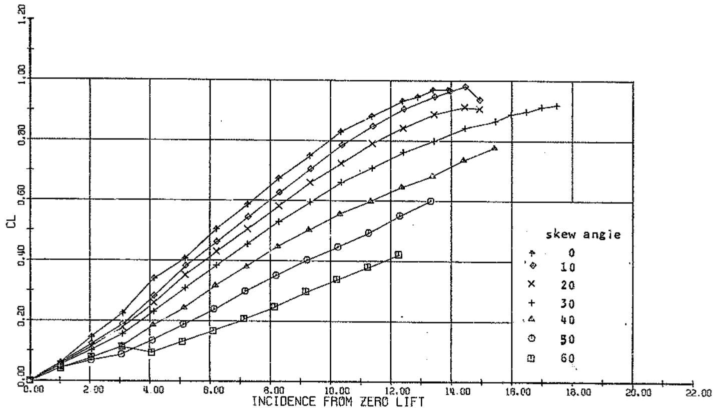

FIGURE F.19 Effect of Skew on Lift Coefficient; Aileron Differential = 10 deg

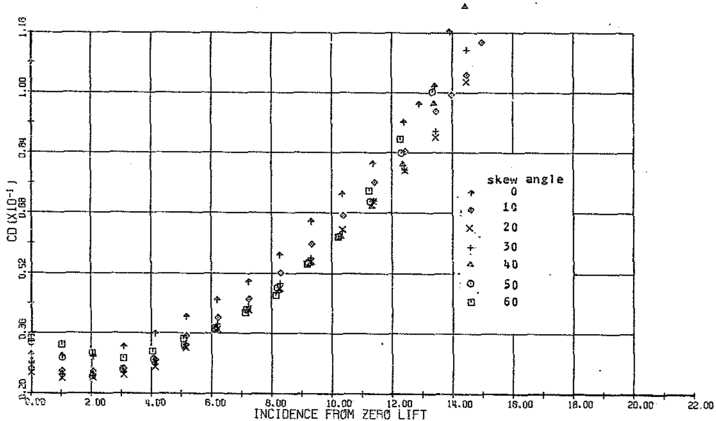

FIGURE F.20 Effect of Skew on Drag Coefficient; Aileron Differential = 10 deg

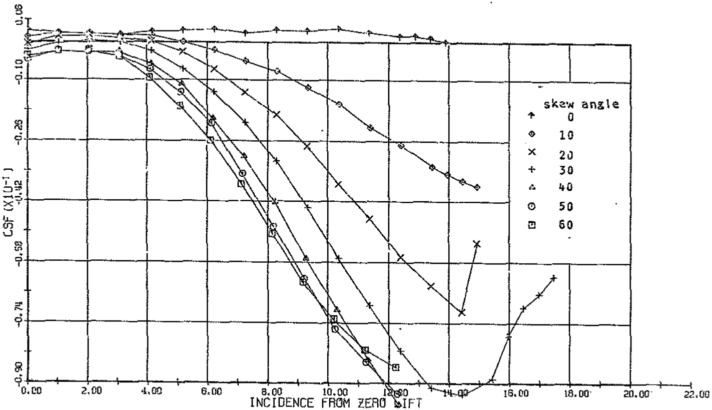

FIGURE F.21 Effect of Skew on Side-Force Coefficient; Aileron Differential = 10 deg

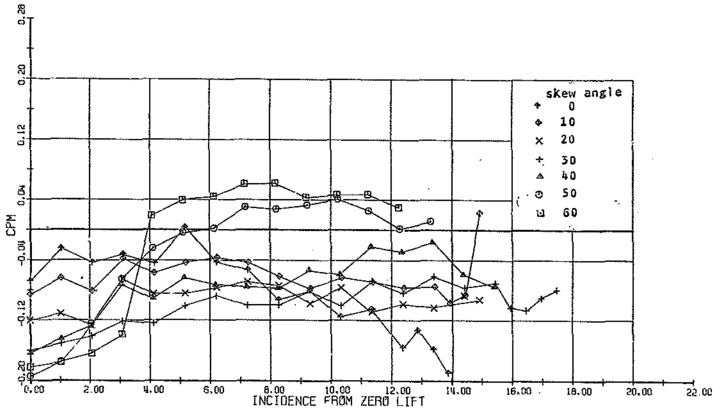

FIGURE F.22 Effect of Skew on Pitching Moment Coefficient; Aileron Differential = 10 deg

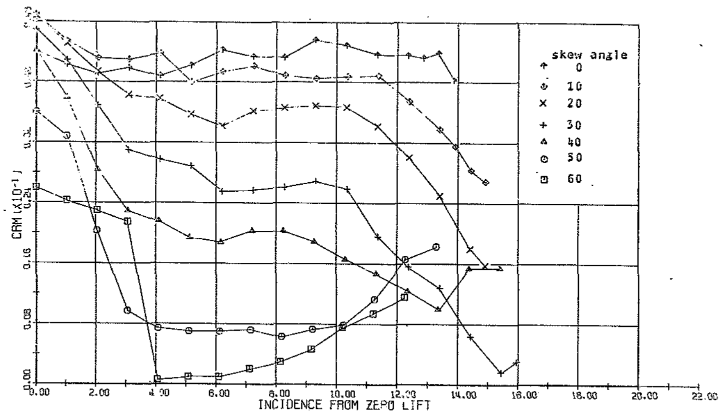

FIGURE F.23 Effect of Skew on Rolling Moment Coefficient; Aileron Differential = 10 deg

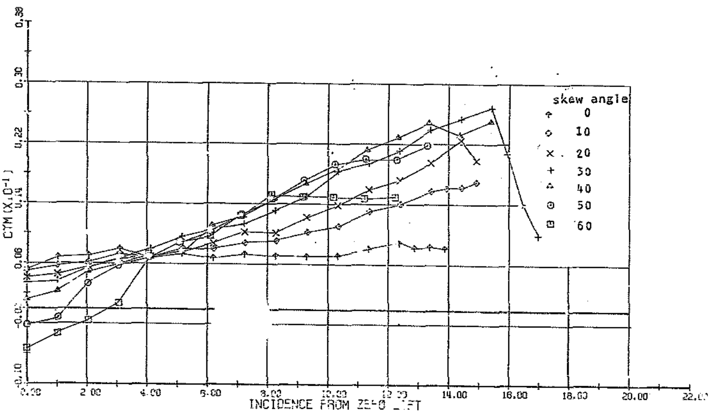

FIGURE F.24 Effect of Skew on Yawing Moment Coefficient; Aileron Differential = 10 deg

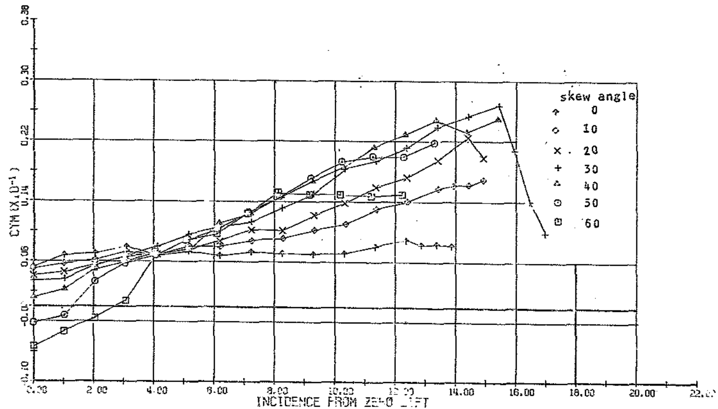

FIGURE F.24 Effect of Skew on Yawing Moment Coefficient; Aileron Differential = 10 deg

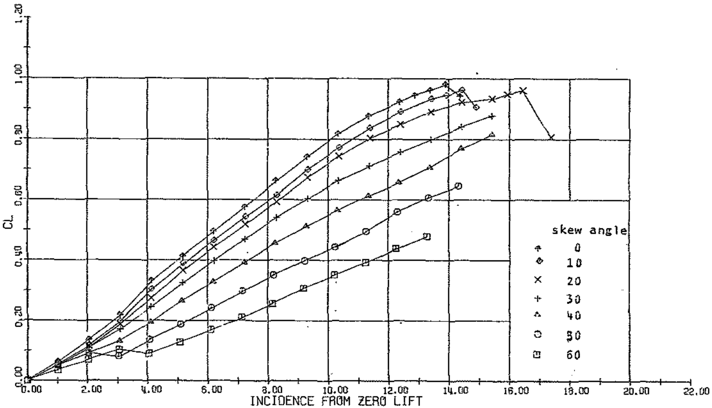

FIGURE F.25 Effect of Skew on Lift Coefficient; Aileron Differential = -10 deg

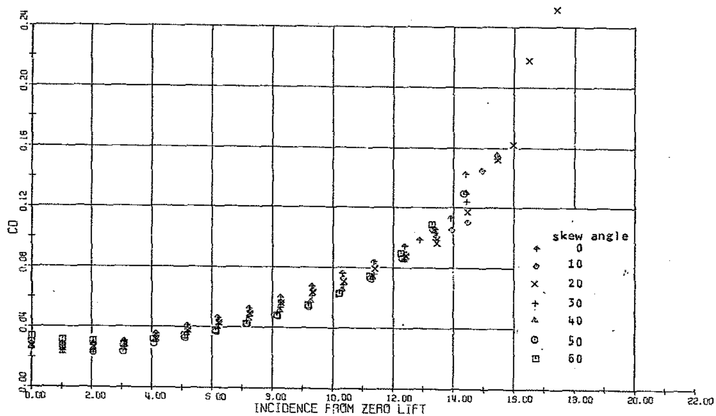

FIGURE F.26 Effect of Skew on Drag Coefficient; Aileron Differential = -10 deg

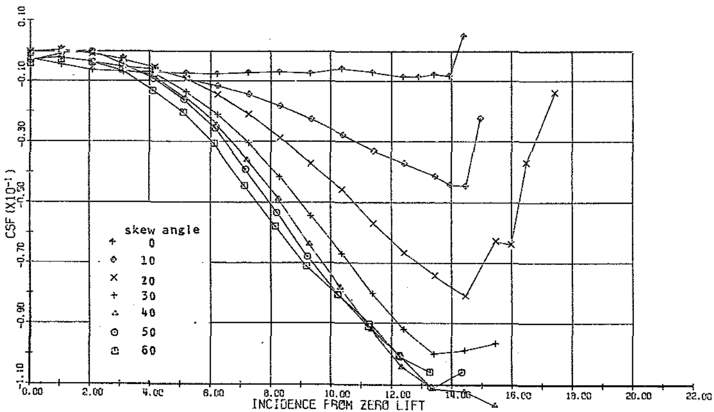

FIGURE F.27 Effect of Skew on Side-Force Coefficient; Aileron Differential = -10 deg

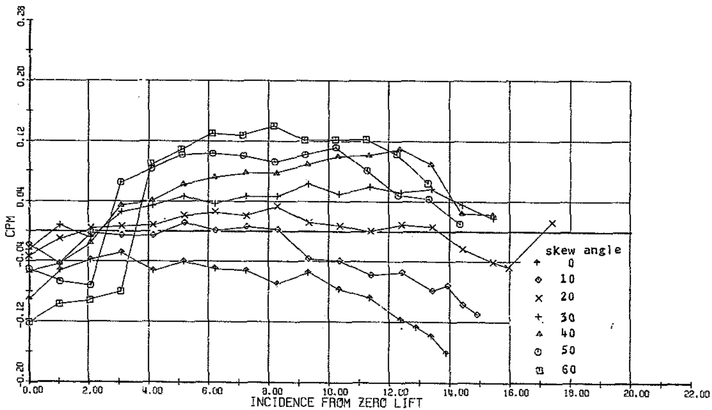

FIGURE F.28 Effect of Skew on Pitching Moment Coefficient; Aileron Differential = -10 deg

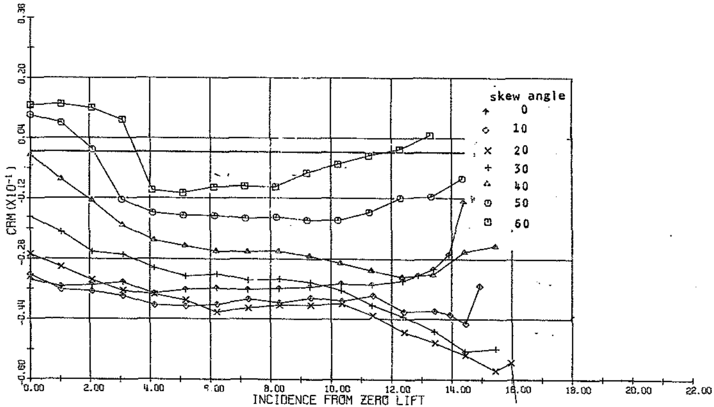

FIGURE F.29 Effect of Skew on Rolling Moment Coefficient; Aileron Differential = -10 deg

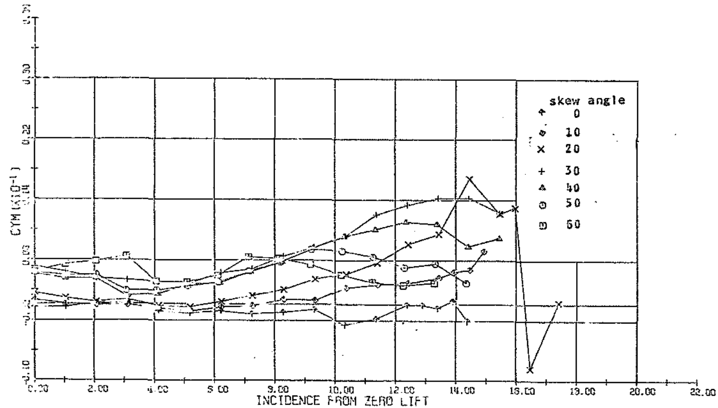

FIGURE F.30 Effect of Skew on Yawing Moment Coefficient; Aileron Differential = -10 deg

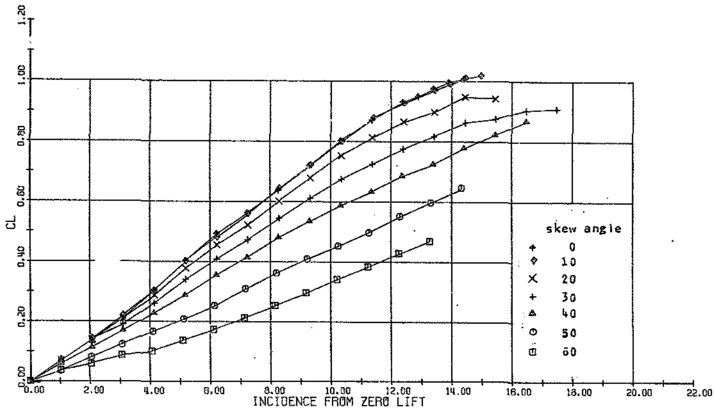

FIGURE F.31 Effect of Skew on Lift Coefficient; Aileron Differential = 15 deg

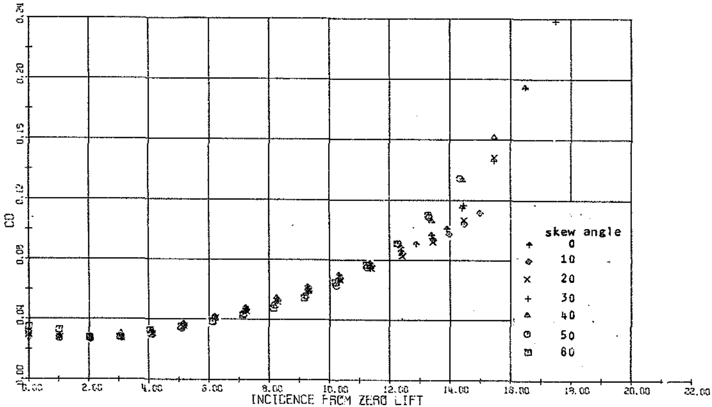

FIGURE F.32 Effect of Skew on Drag Coefficient; Aileron Differential = 15 deg

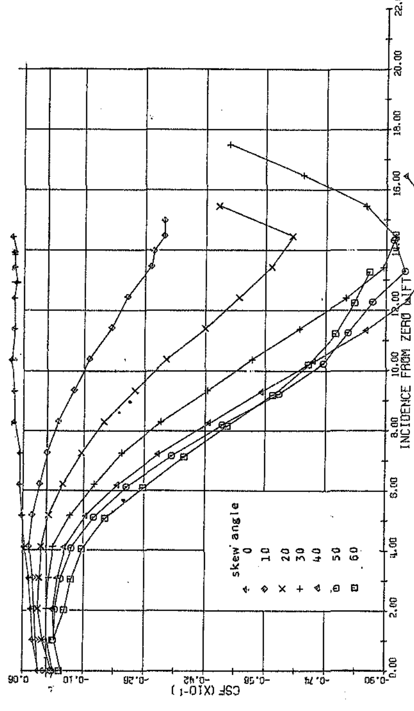

FIGURE F.33 Effect of Skew on Side-Force Coefficient; Aileron Differential = 15 deg

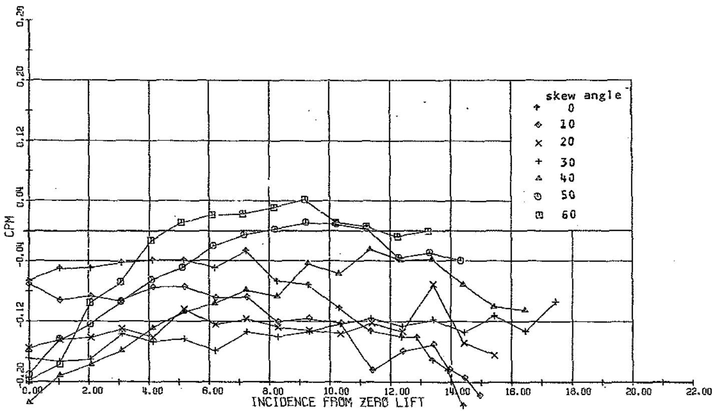

FIGURE F.34 Effect of Skew on Pitching Moment Coefficient; Aileron Differential = 15 deg

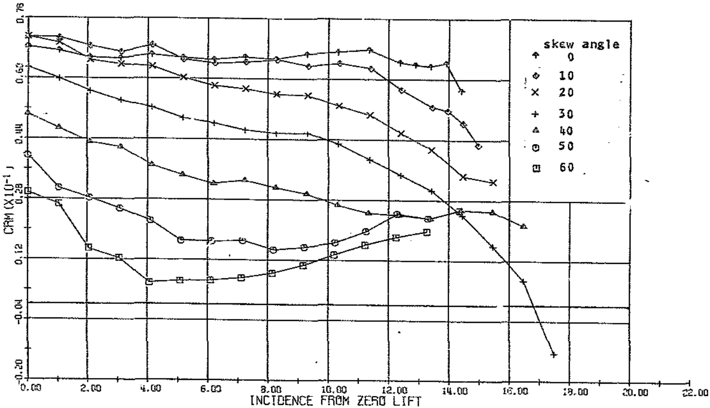

FIGURE F.35 Effect of Skew on Rolling Moment Coefficient; Aileron Differential = 15 deg

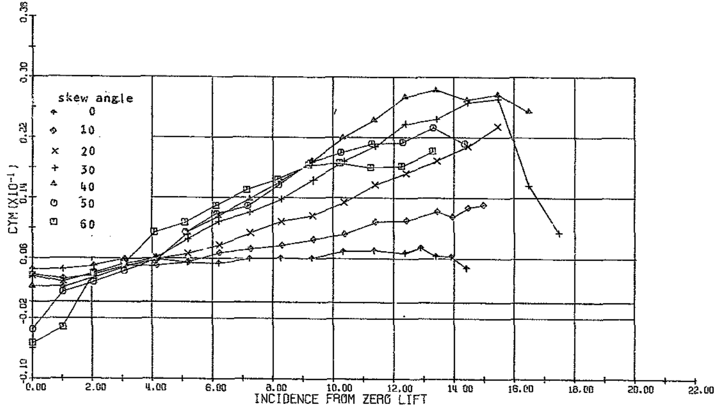

FIGURE F.36 Effect of Skew on Yawing Moment Coefficient; Aileron Differential = 15 deg

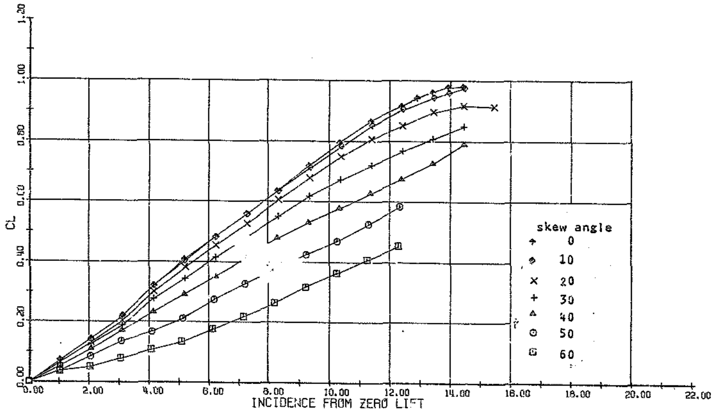

FIGURE F.37 Effect of Skew on Lift Coefficient; Aileron Differential = -15 deg

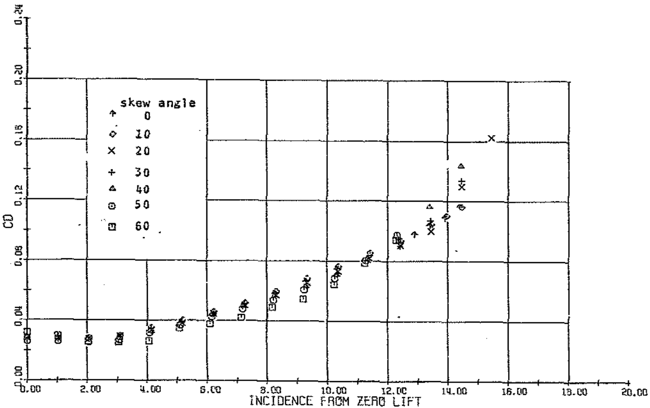

FIGURE F.38 Effect of Skew on Drag Coefficient; Aileron Differential = -15 deg

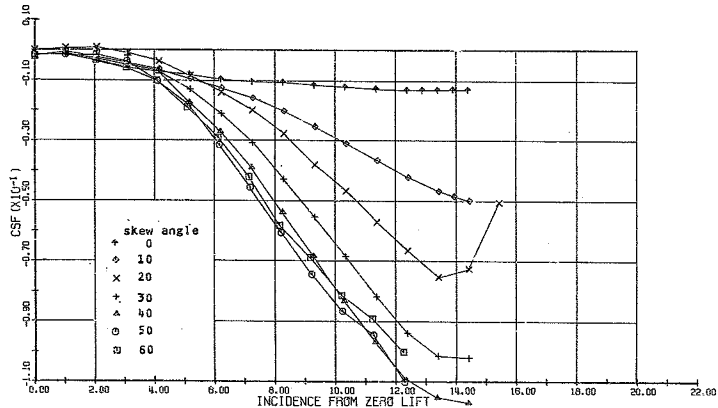

FIGURE F.39 Effect of Skew on Side-Force Coefficient; Aileron Differential = -15 deg

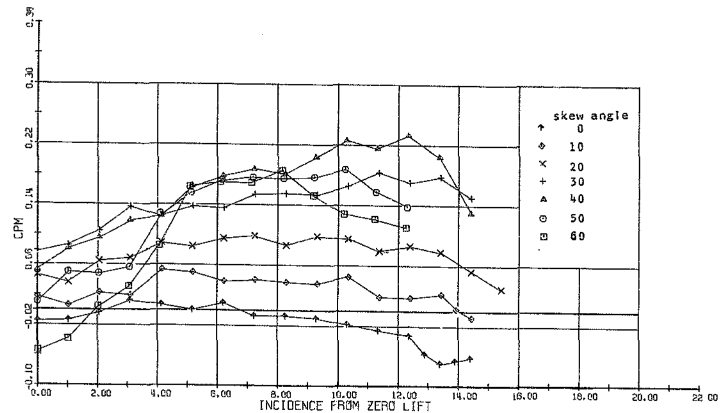

<u>FIGURE F.40</u> <u>Effect of Skew on Pitching Moment Coefficient</u>; Aileron Differential= -15 deg

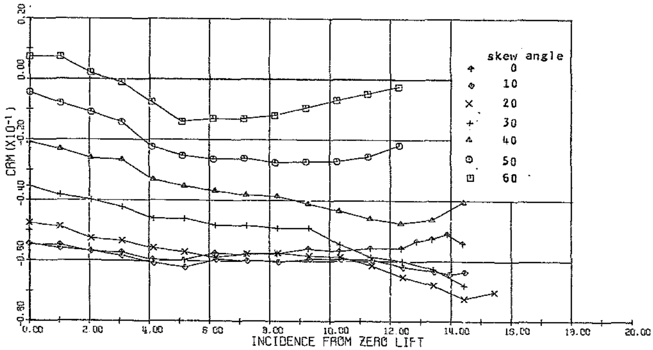

FIGURE F.41 Effect of Skew on Rolling Moment Coefficient; Aileron Differential = -15 deg

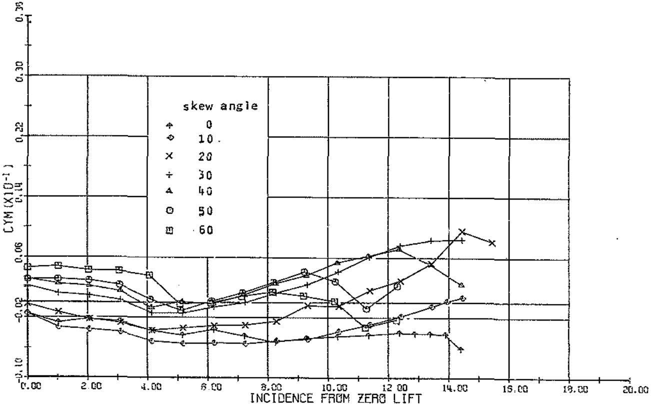

FIGURE F.42 Effect of Skew on Yawing Moment Coefficient; Aileron Differential = -15 deg

F.2 EXPERIMENTAL RESULTS : WIND-TUNNEL MODEL NO. 2

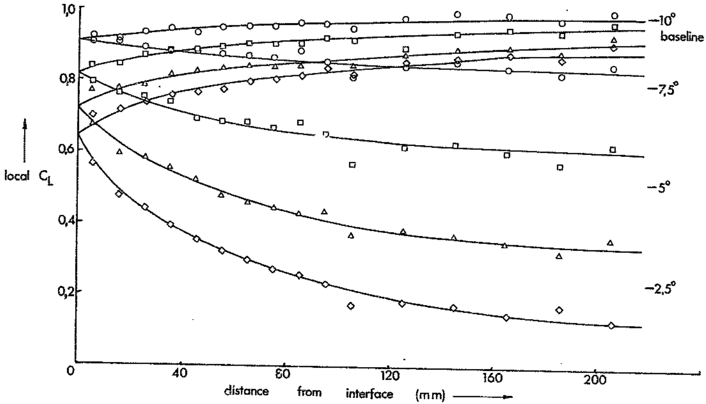

FIGURE F.43: Lift Distribution; Reference Wing at 10 deg Incidence from Zero Lift

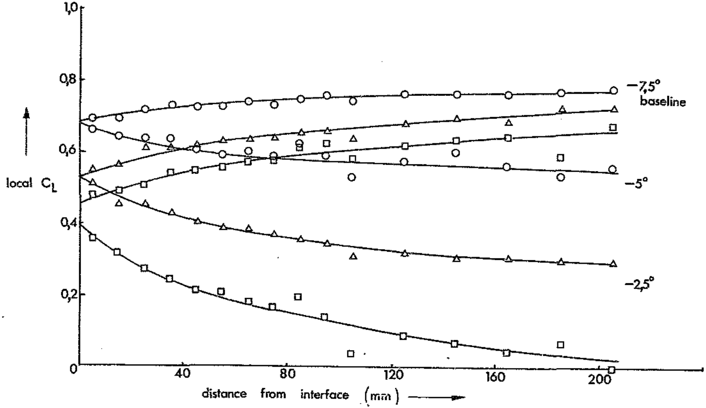

FIGURE F.44: Lift Distribution; Reference Wing at 7,5 deg Incidence from Zero Lift

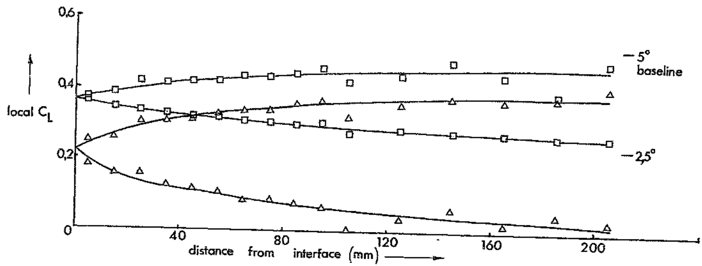

FIGURE F.45: Lift Distribution; Reference Wing at 5 deg Incidence from Zero Lift

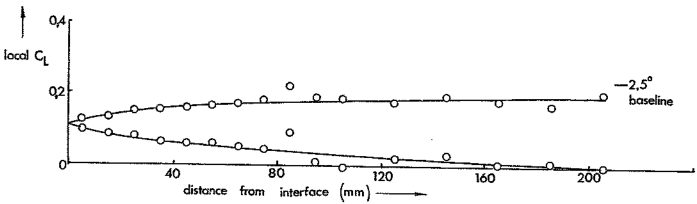

FIGURE F.46: Lift Distribution; Reference Wing at 2,5 deg from Zero Lift

TABLE F.1 NACA 0012 Aileron Oscillations

Skew Angle (deg)

Aileron Differential (deg)	0	10	20	30	40	50	60
0					*	**	**
5				*	*	**	**
10				*	**	**	**
15				*	**	**	**
-5				*	*	**	**
-10			*	**	**	**	**
-15			*	**	**	**	**

* mild aileron oscillations at high incidence
** severe " " " " "

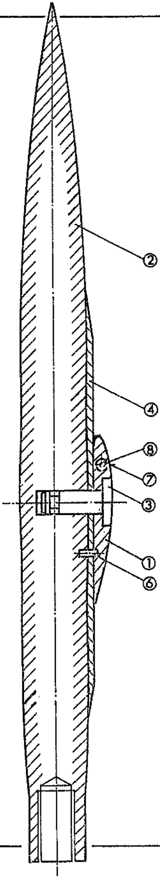

PART NO	DESCRIPTION	NO OFF	MATERIAL
1	WING	1	B51S
2	S-H BODY	1	ALUMINIUM
3	MOUNTING PIN	1	MILD STEEL
4	SADDLE	1	ALUMINIUM
5	AILERON	2	AL./BALSA
6	LOCATING PIN	1	SILVER STEEL
7	BUSH	5	'TEFLON'
8	TIE-ROD	1	SILVER STEEL

SECTIONAL VIEW

FULL SIZE

MODEL NO 1

GENERAL ASSEMBLY

DRWG NO SW1-1/74

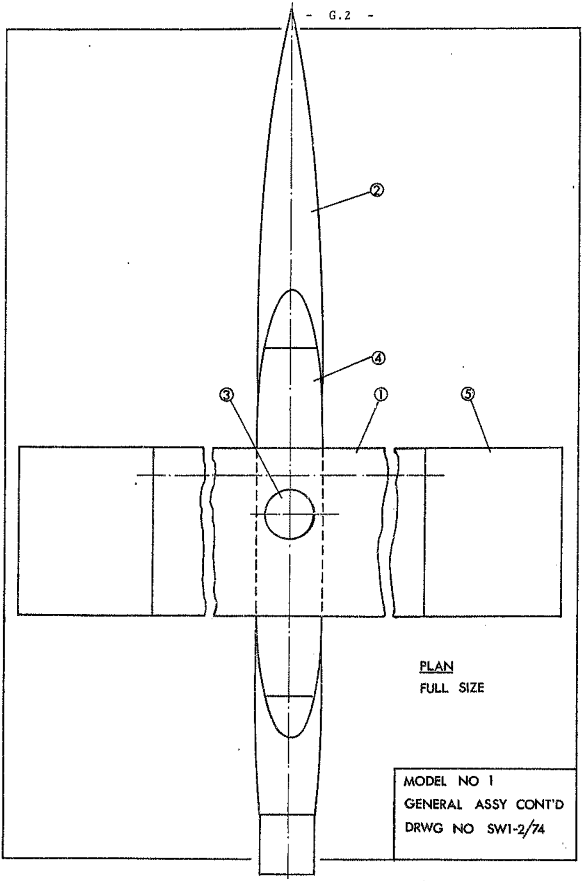

MODEL NO 1
GENERAL ASSY CONT'D
DRWG NO SW1-2/74

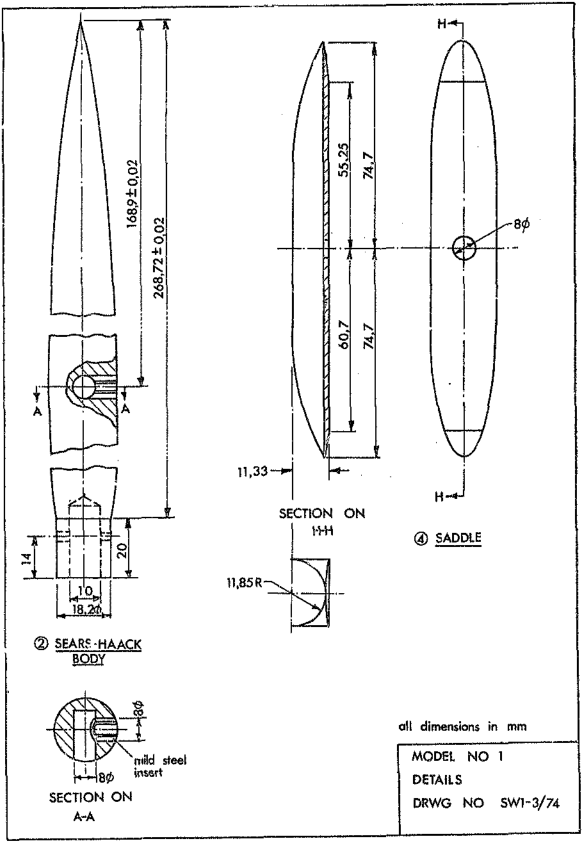
168,9±0,02
268,72±0,02
A
A
14
20
10
18,2ϕ
② SEARS-HAACK BODY
8ϕ
8ϕ
mild steel insert
SECTION ON A-A
55,25
74,7
60,7
74,7
11,33
SECTION ON H-H
11,85R
H
H
8ϕ
④ SADDLE
all dimensions in mm
MODEL NO 1
DETAILS
DRWG NO SW1-3/74

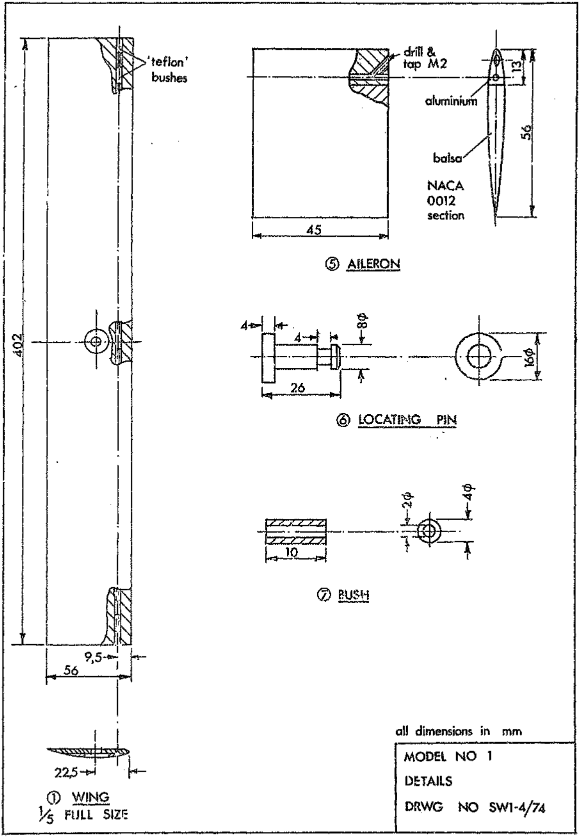
'teflon' bushes
402
9,5
56
22,5
① WING
1/5 FULL SIZE
drill & tap M2
13
aluminium
56
balsa
NACA 0012 section
45
⑤ AILERON
4
4
8φ
16φ
26
⑥ LOCATING PIN
2φ
4φ
10
⑦ BUSH
all dimensions in mm
MODEL NO 1
DETAILS
DRWG NO SW1-4/74

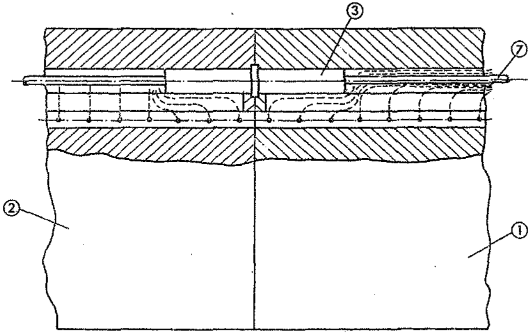

INTERFACE DETAIL
FULL SIZE
-----indicates nylon tubing

PART NO	DESCRIPTION	NO OFF	MATERIAL
1	RIGHT WING	1	B51S ALLOY
2	LEFT "	1	" "
3	CENTRE PIN	1	M.S.
4	SEALING PLATE	2	ALUMINIUM
5	WING BUSH	2	"
6	LOCATING BUSH	2	M.S.
7	TENSION ROD	2	SILVER STEEL
8	ROD SUPPORT	2	BRASS

MODEL NO 2
GENERAL ASSEMBLY
DRWG NO SW2-1/75

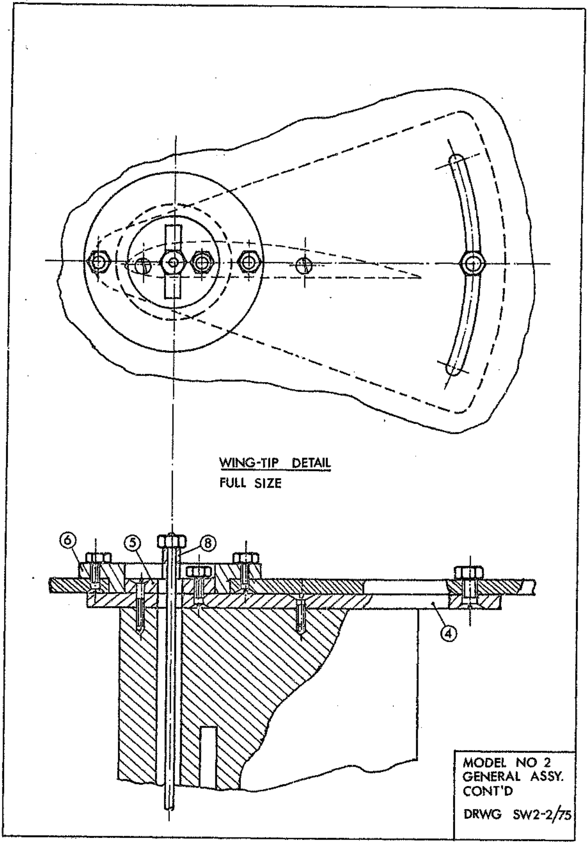
WING-TIP DETAIL
FULL SIZE
6
5
8
4
MODEL NO 2
GENERAL ASSY.
CONT'D
DRWG SW2-2/75

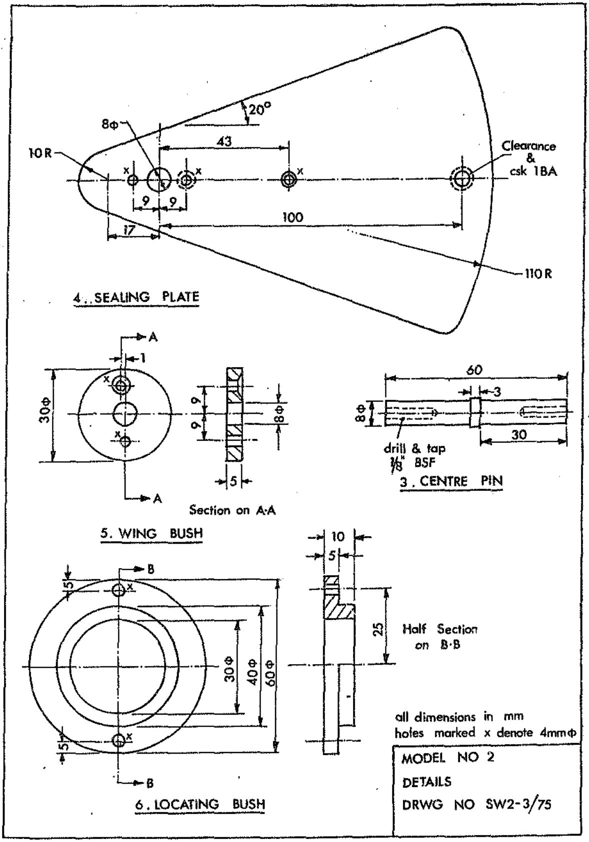
20°
8Φ
43
10 R
Clearance & csk 1BA
9
9
100
17
110 R
4. SEALING PLATE
A
1
30Φ
9
9
8Φ
5
A
Section on A-A
5. WING BUSH
60
3
8Φ
30
drill & tap 1/8" BSF
3. CENTRE PIN
10
5
B
5
30Φ
40Φ
60Φ
25
Half Section on B-B
5
B
6. LOCATING BUSH
all dimensions in mm
holes marked x denote 4mmΦ
MODEL NO 2
DETAILS
DRWG NO SW2-3/75

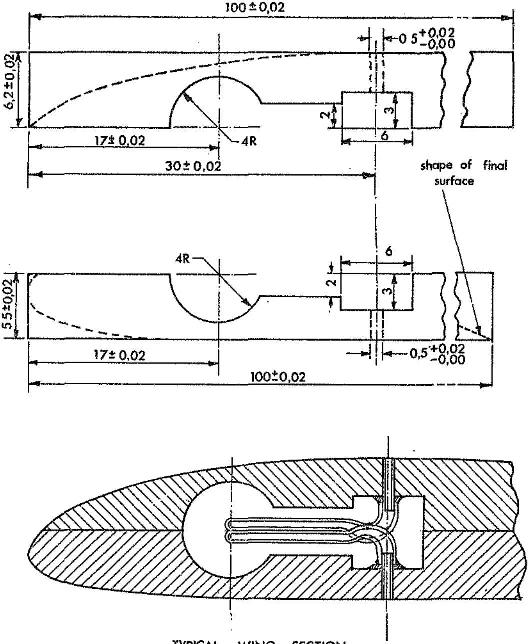

TYPICAL WING SECTION

4 × FULL SIZE

all dimensions in mm

MODEL NO 2

WING DETAILS

DRWG NO SW2-4/75

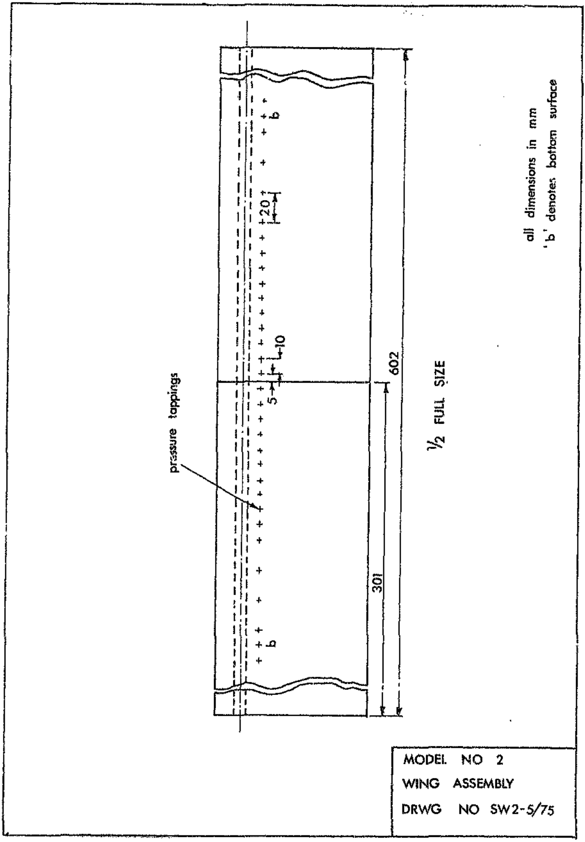

all dimensions in mm
'b' denotes bottom surface
pressure tappings
20
10
5
b
b
602
301
½ FULL SIZE
MODEL NO 2
WING ASSEMBLY
DRWG NO SW2-5/75